Ultra-Slow and Superluminal Light Propagation in Solids at Room Temperature

by

Matthew S. Bigelow

Submitted in Partial Fulfillment

of the

Requirements for the Degree

Doctor of Philosophy

Supervised by

Professor Robert W. Boyd

The Institute of Optics
The College
School of Engineering and Applied Sciences

University of Rochester
Rochester, New York

2004

Curriculum Vitae

Matthew Bigelow was born in Colorado Springs, Colorado on July 26, 1975. He attended Pillsbury Baptist Bible College in Owatonna, Minnesota for 1994-1995 academic year and then transferred to Colorado State University in Fort Collins, Colorado in the Fall of 1995. There he graduated *Summa Cum Laude* with a Bachelor of Science in both mathematics and physics in 1998. As an undergraduate, he was awarded the Hewlett Packard Employee Scholarship (1995), the First-Year Physics Student Scholarship (1996), the Undergraduate Research Scholarship (1997), and the Weber Scholarship (1998) which goes to the top student in the Department of Physics. In addition, during his senior year he was honored as a Achievement Rewards for College Scientists (ARCS) Scholar which is awarded to the top student in the College of Natural Sciences at Colorado State University. He came to the University of Rochester in August of 1998 as a Ph.D. graduate student at the Institute of Optics. He joined the Nonlinear Optics group under the direction of Professor Robert W. Boyd in June of 1999. His graduate studies include ultra-slow and superluminal light propagation in room-temperature solids, stimulated Brillouin scattering, 2-D spatial soliton stability, and the production of polarization-entangled photons in bulk materials using a third-order nonlinearity. From the Fall of 1999 to the Spring of 2004, he received the Frank J. Horton Graduate Research Fellowship through the Laboratory for Laser Energetics.

Acknowledgements

I would like to thank the Laboratory for Laser Energetics for its generous support through the Frank J. Horton Graduate Research Fellowship.

I would also like to acknowledge the help of my fellow students John Heebner, Ryan Bennink, Sean Bentley, Vincent Wong, Giovanni Piredda, Aaron Schweinsberg, Colin O'Sullivan-Hale, Petros Zerom, Ksenia Dolgaleva, Yu Gu, and George Gehring. I'm also grateful for the help of Yoshi Okawachi and the assistance of the other members of Alex Gaeta's group during my trips to Ithaca to work on the SBS slow light experiment. In addition, I would like to give a special thanks to Nick Lepeshkin for his assistance on many of these experiments. Also, I thank Dan Gauthier for the helpful discussions we had on information velocity.

I also appreciate the help of Joan Christian, Gayle Thompson, and Noelene Votens. They always seemed to find time to help and never seemed to get flustered even though I know I inconvenienced them many times.

I especially would like to thank my advisor, Dr. Robert Boyd, for his help, support, and encouragement. His hard work for all of us is greatly appreciated.

Finally, I would like to thank my wife Allison for putting up with both me and Rochester all these years. I could not have done it without you.

Publications

Alex Gaeta, Yoshi Okawachi, Matthew S. Bigelow, Aaron Schweinsberg, Robert W. Boyd, and Dan J. Gauthier, *Precise group velocity control in an SBS amplifier*, (To be submitted).

Aaron Schweinsberg, Matthew S. Bigelow, Nick N. Lepeshkin, and Robert W. Boyd, *Observation of slow and fast light in erbium-doped optical fiber*, (To be submitted).

Matthew S. Bigelow, Nick N. Lepeshkin, and Robert W. Boyd, *Information velocity in materials with large normal or anomalous dispersion*, (Submitted to Phys. Rev. A).

Robert W. Boyd, Matthew S. Bigelow and Nick N. Lepeshkin, *Superluminal and ultra-slow light propagation in room-temperature solids*, Laser Spectroscopy, Proceedings of the XVI International Conference, pp. 362-364 (2004).

Matthew S. Bigelow, Petros Zerom, and Robert W. Boyd, *Breakup of ring beams carrying orbital angular momentum in sodium vapor*, Phys. Rev. Lett. **92**, 083902 (2004).

Matthew S. Bigelow, Nick N. Lepeshkin, and Robert W. Boyd, *Superluminal and slow light propagation in a room temperature solid*, Science **301**, 200 (2003).

Matthew S. Bigelow, Nick N. Lepeshkin, and Robert W. Boyd, *Observation of ultra-slow light propagation in a ruby crystal at room temperature*, Phys. Rev. Lett. **90** 113903 (2003).

Matthew S. Bigelow, Q-Yan Park, Robert W. Boyd, *Stabilization of the propagation of spatial solitons*, Phys. Rev. E **66**, 04631 (2002).

Conference Papers

Matthew S. Bigelow, Nick N. Lepeshkin, Robert W. Boyd, *Information velocity in ultra-slow and fast light media*, **IMP1**, IQEC 2004, San Francisco, CA.

Matthew S. Bigelow, Sean J. Bentley, Alberto M. Marino, Robert W. Boyd, Carlos R. Stroud, Jr., *Polarization properties of photons generated by two-beam excited conical emission*, **ThA6**, OSA Annual Meeting 2003, Tucson, AZ.

Matthew S. Bigelow, Nick N. Lepeshkin, Robert W. Boyd, *Observation of superluminal pulse propagation in alexandrite*, **QTuG33**, QELS 2003, Baltimore, MD.

Matthew S. Bigelow, Nick N. Lepeshkin, Robert W. Boyd, *Observation of slow light in ruby*, **MX3**, OSA Annual Meeting 2002, Orlando, FL.

Nick N. Lepeshkin, Matthew S. Bigelow, Robert W. Boyd, Abraham G. Kofman, Gershon Kurizki, *Brillouin scattering in media with sound dispersion*, **WU2**, OSA Annual Meeting 2002, Orlando, FL.

Matthew S. Bigelow, Svetlana G. Lukishova, Robert W. Boyd, Mark D. Skeldon, *Transient stimulated Brillouin scattering dynamics in polarization maintaining optical fiber*, **CTuZ3**, CLEO 2001, Baltimore, MD.

Invited Talks

Matthew S. Bigelow, *Ultra-Slow and Superluminal Light Propagation in Room-Temperature Solids*, First International Conference on Modern Trends in Physics Research (MTPR-04), Cairo, Egypt, April 6, 2004.

Matthew S. Bigelow, *Ultra-Slow and Superluminal Light Propagation in Room-Temperature Solids*, S & T Seminar, Laboratory for Laser Energetics, Rochester, NY, February 20, 2004.

Abstract

Slow and superluminal group velocities can be observed in any material that has large normal or anomalous dispersion. While this fact has been known for more than a century, recent experiments have shown that the dispersion can be very large without dramatically deforming a pulse. As a result, the significance and nature of pulse velocity is being re-evaluated. In this thesis, I review some of the current techniques used for generating ultra-slow, superluminal, and even stopped light. While ultra-slow and superluminal group velocities have been observed in complicated systems, from an applications point of view it is highly desirable to be able to do this in a solid that can operate at room temperature. I describe how coherent population oscillations can produce ultra-slow and superluminal light under these conditions. In addition, I explore the information (or signal) velocity of a pulse in a material with large dispersion. Next, I am able to demonstrate precise control of the pulse velocity in an erbium-doped fiber amplifier. I extend this work to study slow light in an SBS fiber amplifier. This system has much larger bandwidth and can produce much longer fractional delays, and therefore has great potential to control the group velocity for applications in all-optical delay lines. Finally, I investigate numerically and experimentally the stability of ring-shaped beams with orbital angular momentum in a material with a saturable nonlinearity.

Contents

List of Figures

Chapter 1

Introduction

"And God saw the light, that it was good ..." — Genesis 1:4

For over 100 years, the problem of how a wave travels through a dispersive material is one that has been studied in great detail [1–3]. Recent interest in this problem has been sparked by the discovery of systems that have high dispersion, yet allow a pulse to propagate relatively undistorted. In addition, these new systems have relatively low loss so the pulse dynamics are easy to observe. However, until now, all of the systems that have been developed to generate slow or fast light are fairly complicated and difficult to implement. Specifically, these experiments are done in ultra-cold or hot atomic vapors or in solids at liquid helium temperatures. They also require precisely tuned and highly stable laser systems. For real-world applications, such complicated systems are a liability. In this thesis, I explore better ways to produce slow and fast

light—methods that work in a room-temperature solid-state material.

1.1 Velocities of Light

Before any discussion can begin on the techniques used to change the speed of light, it is important to define the characteristic velocities of light. In this section, I will introduce five important velocities of an electro-magnetic wave in a material: the phase velocity, the group velocity, the centro-velocity, the energy-transport velocity, and the signal or information velocity. This is certainly not a complete list. In fact, there are at least eight characteristic velocities of light propagation [4, 5]. However, usually only a few of these are distinct in any given system.

1.1.1 Phase and Group Velocity

It is believed that Lord Rayleigh was the first to note the difference between the phase and group velocity [1]. The phase velocity of a monochromatic wave in a dispersive medium is defined as the velocity of points of constant phase. If the complex electric field is given as

$$
\begin{aligned}
E(z,t) &= E_0 e^{i(kz-\omega t)} \\
&= E_0 e^{ik(z-\frac{\omega}{k}t)},
\end{aligned}
\tag{1.1}
$$
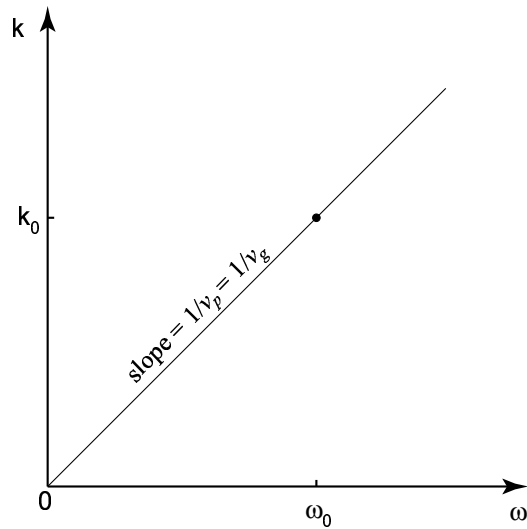
Figure 1.1: The dispersion diagram for electro-magnetic waves travelling in a vacuum.

the points of constant phase will travel at a velocity

$$v_p = \frac{\omega}{k},$$ (1.2)

where k is the wavenumber and ω is the angular frequency. This thought is frequently expressed in terms of a refractive index n_0, where $v_p = c/n_0$. If the field is not monochromatic, another velocity associated with wave propagation becomes relevant. This velocity, the group velocity, is defined as

$$v_g = \frac{d\omega}{dk}.$$ (1.3)

In a vacuum, the group velocity is equal to the phase velocity (Fig. 1.1) since all frequency components travel at the same speed (c). However, in general the group

velocity will be different from the phase velocity. If the electromagnetic field interacts with the material at *any* frequency the material becomes dispersive at *all* frequencies, and the group velocity no longer exactly equals the phase velocity. In fact, near an optical resonance, the group velocity can be negative (Fig. 1.2). While usually
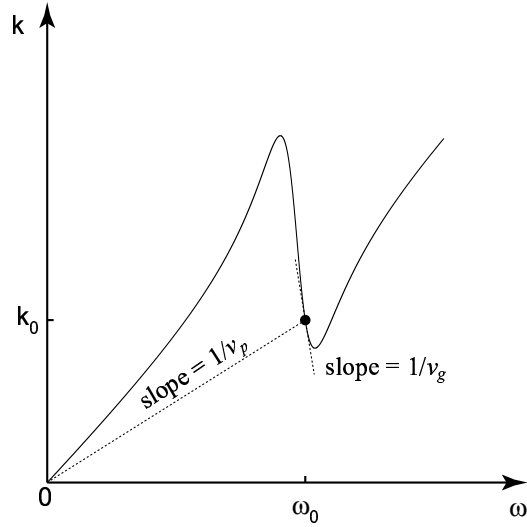
Figure 1.2: A dispersion curve containing a material resonance indicating the values for the phase and group velocity at a given frequency. The phase velocity is given by $v_p = \omega_0 / k_0$. The group velocity is the inverse of the slope of the dispersion curve at the frequency ω_0.

identified with the velocity of a pulse, the group velocity can be thought of as the speed of the propagating temporal interference pattern produced by multiple spectral components. For a pulse with a central frequency ω_0, the group index is given as

$$
\begin{aligned}
n_g(\omega_0) = \frac{c}{v_g} &= c\frac{dk}{d\omega} \\
&= c\frac{d\left(\omega n(\omega_0)/c\right)}{d\omega} \\
&= n(\omega_0) + \omega_0\frac{dn(\omega_0)}{d\omega}.
\end{aligned} \tag{1.4}
$$

1.1.2 Centro-velocity

The centro-velocity, as first introduced by Smith [4], is the velocity of the temporal center-of-mass of the pulse intensity. Formally it is defined as

$$v_c = \left| \nabla \left(\frac{\int_{-\infty}^{\infty} t E^2(\mathbf{r}, t) dt}{\int_{-\infty}^{\infty} E^2(\mathbf{r}, t) dt} \right) \right|^{-1} \tag{1.5}$$

where E($\mathbf{r}$,t) is the electric field over all space. In most cases, this velocity is equal to the group velocity except when a pulse experiences some asymmetric pulse distortion. The centro-velocity is actually very useful in that it is always defined, unlike the group velocity, for pulses that are badly distorted or broken up into multiple pulses. It also has the advantage that it can be easily measured.

1.1.3 Energy-Transport Velocity

The velocity at which electro-magnetic energy is transmitted through a material is complicated by the fact that some of the energy is stored in the material and the rest is contained in the electromagnetic field. Formally, it can be defined as the ratio of the Poynting vector to the stored energy density of the wave, or

$$v_e = \mathbf{S}/W. \tag{1.6}$$

However, it has been shown by Loudon that this velocity is equal to the group velocity in a non-absorbing dielectric, but is different in the presence of absorption [6].

Specifically, he was able to write the closed form expression

$$v_e = \frac{c}{n_{\mathrm{r}} + 2\omega n_{\mathrm{i}}/\Gamma},$$

(1.7)

where Γ is the oscillator damping coefficient of a Lorentz material and n_{r} and n_{i} are the real and imaginary parts of the refractive index (see Appendix B). Loudon also noted that this velocity is bounded by c. Not surprisingly then, other authors claim that the energy velocity is equal to the signal velocity in many cases [2, 7, 8].

1.1.4 Information Velocity

The concept of signal or information velocity becomes particularly important in a material with anomalous dispersion. This concept was first introduced by Sommerfeld and Brillouin because of concerns that superluminal pulse propagation in a material with anomalous dispersion could contradict the predictions of special relativity [2]. They noted that a distinction had to be made between the group velocity and the information velocity. However, unlike the other velocities, the information velocity is difficult to define because of the difficulty in defining "information." Attempting to answer this question, Brillouin defined a signal as "... a short isolated succession of wavelets, with the system at rest before the signal arrived and also after it has passed." From this definition, Brillouin calculated the field of a square pulse through a material with a single Lorentz resonance. This calculation led to the prediction of Brillouin (high frequency) and Sommmerfeld (low frequency) forerunners or precursors. Both

Brillouin and Sommerfeld assumed that it was not possible to detect precursors, and they found that the signal velocity is equal to the group velocity in regions of normal dispersion. In regions of anomalous dispersion where the group velocity exceeds c, they found that the signal velocity is still bounded by c, but has a maximum at the resonant frequency of the Lorentz atom. However, the assumption that it is impossible to detect precursors has since been shown to be incorrect [9, 10]. Conversely, Smith found that the signal velocity actually has a minimum at the resonance frequency [4]. More recently, Oughstun and Sherman gave a very rigorous discussion of electromagnetic wave propagation in a dispersive material [7]. They agreed with Smith that the signal velocity is minimum at the resonance frequency, but they found, contrary to the view of Sommerfeld and Brillouin, that the signal velocity can be well defined.

Nevertheless, Sommerfeld makes a very good point when he states [2]:

> It can be proven that the signal velocity is exactly equal to c if we assume the observer to be equipped with a detector of infinite sensitivity, and this is true for normal or anomalous dispersion, for isotropic or anisotropic medium, that may or may not contain conduction electrons.

Therefore, if it is possible to note the exact moment when the electric field becomes non-zero, we have effectively detected the signal, and the signal velocity must be equal to c.

Still others have argued that information velocity is equal to the group velocity even when the group velocity is superluminal [11]. However, Stenner *et al.* have

presented compelling evidence that the information velocity is less than or equal to c in a material where the group velocity is negative [12]. They sent two different types of pulses into a system with large anomalous dispersion—a '1'-pulse that would suddenly jump to a higher value at the peak, and '0'-pulse that would rapidly drop to zero at the peak. They found that despite sending these pulses through a material with negative group velocity, it was not possible to distinguish between a '1' or '0' early. The information contained in the type of pulse sent into the material could not be discerned before you could distinguish the pulses in vacuum. We will consider these claims more closely in a later chapter.

1.2 Kramers-Kronig Relations

While some of the systems developed to produce large group velocities are rather exotic, they need not be. Rather, all that is necessary is to have a system where the refractive index changes rapidly as a function of frequency. This is usually done in a material which is at or near a resonance with the applied optical field. To see why this is so, we consider the Kramers-Kronig relations (see derivation in Appendix A)

$$n_{\rm r}(\omega) \;=\; 1 + \frac{c}{\pi} P \int_0^\infty \frac{\alpha(s)}{s^2 - \omega^2} ds, \tag{1.8a}$$

$$\alpha(\omega) \;=\; -\frac{4\omega^2}{\pi c} P \int_0^\infty \frac{n_{\rm r}(s) - 1}{s^2 - \omega^2} ds. \tag{1.8b}$$
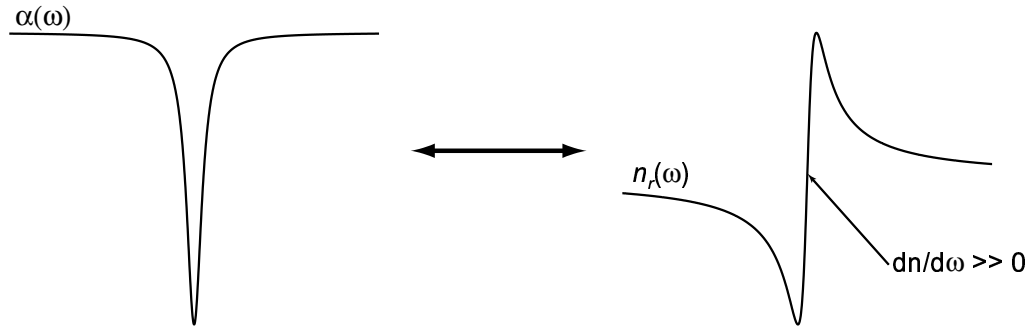
Figure 1.3: The absorption and refractive index are related through the Kramers-Kronig Relations. A narrow spectral hole will produce strong normal dispersion.

which relate the real part of the refractive index to the absorption within the material. From a simple analysis of these equations, one can show that a narrow dip in an absorption spectrum will produce strong normal dispersion ($dn/d\omega \gg 0$), whereas a peak or gain will produce anomalous dispersion ($dn/d\omega \ll 0$). I illustrate the former case in Fig. 1.3. Since the group index of a pulse is given in Eq. (1.4) as $n_g = n_0 + \omega \frac{dn}{d\omega}$, if the dispersion is large, the group index can also be large (either positive or negative).

Therefore, the key to producing a slow (or fast) light material is to find some physical process which has a strong, but narrow spectral feature. Such a feature, by the Kramers-Kronig relations, will produce the large dispersion necessary for slow or fast light.

1.3 Ultra-Slow and Stopped Light

It has long been known that a rapid change in the refractive index near a material resonance leads to a large value of the group index [2,3,13]. However, in these situations strong absorption accompanies the low group velocity making the experimental observation of these effects difficult although not altogether impossible. In the first experimental observation of slow and fast light propagation in a resonant system [14], laser pulses propagated without appreciable shape distortion, but experienced very strong resonant absorption ($\sim 10^5$ cm^{-1}).

To reduce absorption, most of the recent work on slow light propagation has made use of the technique of electromagnetically induced transparency (EIT) to render the material medium highly transparent (Fig. 1.4) while still retaining the strong dispersion required for the creation of slow light [15–17]. These spectral features can be so narrow that pulses are considered to be "ultra-slow." Using this technique, Kasapi *et al.* [18] observed a group velocity of $v_g = c/165$ in a 10-cm-long Pb vapor cell.

Interest in this field really exploded when Hau *et al.* [19] observed a group velocity of 17 m/s in a Bose-Einstein condensate (BEC). However, it has since been shown that ultra-slow group velocities are possible in more traditional states of matter. Kash *et al.* [20] also used an EIT technique to measure a group velocity of 90 m/s in a hot rubidium vapor. Using similar techniques, Budker *et al.* [21] have inferred group velocities as low as 8 m/s.
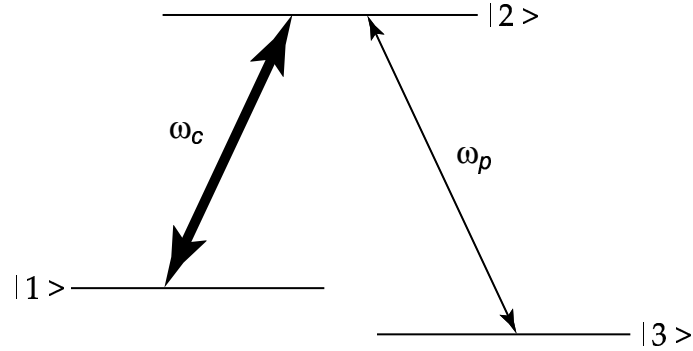
Figure 1.4: To produce EIT, a strong control beam (ω_p) is applied between levels $|1\rangle$ and $|2\rangle$. This effectively splits level $|2\rangle$ so that a probe beam sees reduced absorption over a very narrow spectral range.

In the first demonstration of ultra-slow light in a solid, Turukhin *et al.* [22] have observed a velocity of 45 m/s in a praseodymium doped Y_2SiO_5 crystal. They again used EIT techniques, but in order to maintain ground state coherence, the sample had to be cooled to a cryogenic temperature of 5 K.

It has also been demonstrated that it is possible to stop or store a pulse of light and then 'release' it at a significantly later time [23–25]. Such devices could have applications in optical memories and optical computing. A dynamically controlled photonic band gas is one particularly promising technique developed by Bajscy *et al.* [25]. The key feature of this technique consists of two counter-propagating lasers that are tuned to the control field frequency in an EIT system to form periodic regions where a probe field will see reduced absorption. With only one control field present, the pulse enters the material. The second field is then applied which 'traps' the probe inside the photonic lattice. It can then be released again by turning off one of the control fields. The intriguing part of this technique is that the photonic component

of the pulse never disappears; it is truly a case of stopped light.

1.4   Fast Light

There has also been considerable experimental work in the production of fast light [26, 27]. Akulshin *et al.* have observed a group velocity of $-c/23{,}000$ using electromagnetically induced absorption [28]. More recently, Kim *et al.* [29] used the same technique and observed a group velocity of $-c/14{,}400$. Another technique is gain-assisted superluminal light propagation which was first proposed by Steinberg and Chiao [30]. In this technique, a probe pulse is tuned between the gain lines produced by two pump beams. The probe sees less gain between these lines, and correspondingly large anomalous dispersion. Later Wang *et al.* demonstrated a group velocity of $-c/310$ using this method [31]. Stenner *et al.* [12] (who we mentioned in the context of information velocity) used a slightly modified version of the gain-assisted superluminal light propagation technique to produce pulse advancements that were nearly 11% the width of the pulse ($v_g = -c/19.6$).

Another form of fast light is superluminal barrier tunnelling. The possibility that a particle may be able to tunnel through a barrier in a time independent of barrier width has been a point of controversy for many years [32–35]. Recently, Steinberg *et al.* [36] measured the tunnelling time of a single photon through a 1-D photonic band gap material and found that the photon appears on the far side of the barrier $\sim$1.5 fs earlier than had it been travelling in vacuum. In addition, Spielman *et al.* [37] found

that pulse propagation time through a photonic band gap material is independent of the length of the material. These apparent violations of causality were resolved by Winful [38,39] who showed that for relatively long pulses, the field of the transmitted pulse through a barrier can adiabatically follow the incident pulse with almost no delay. However, if the pulse is too narrow, the output field can not follow the input field and no superluminal pulse advancement can be seen.

1.5 Stability of 2-D Spatial Solitons

I also did extensive theoretical and experimental work on 2-D spatial solitons. Optical spatial solitons (self-trapped light filaments) [40] hold great promise for many applications in modern optical technology such as photonics and optical computing [41,42]. Recently, there has also been considerable interest in the formation of higher-order spatial solitons [43], that is, solitons possessing complex transverse structure leading to radial and/or azimuthal nodes of the field distribution. Beams that have a ring-shaped intensity pattern and carry orbital angular momentum are of particular interest because of their increased information content and their greater power handling capabilities [44]. Such beams have an $e^{im\phi}$ field dependence and carry $m\hbar$ of orbital angular momentum per photon [45,46]. The entanglement of photons with orbital angular momentum has generated considerable interest [47–49]. Orbital angular momentum provides an infinite number of quantum states that may be entangled, and thereby may find applications in the field of quantum information such as quantum

cryptography.

However, it is well established that self-trapped beams (that is, (2+1) dimensional waves) are unstable in a homogeneous Kerr medium [50]. Ring-shaped solitons are more resistant to whole-beam collapse, but these beams have been shown to have strong azimuthal instabilities in both a saturable Kerr medium and in a material with a competing quadratic $\left(\chi^{(2)}\right)$ and cubic $\left(\chi^{(3)}\right)$ nonlinearity [51, 52]. Specifically, these solitons are most likely to break up into $2m$ filaments that drift away tangentially from the original ring [51].

Several techniques have been proposed and implemented for increasing the stability of spatial solitons, including the use of saturable nonlinear materials [53], geometries with restricted dimensionality [54], non-paraxial beams [55], and multicomponent (vector) solitons [56–60]. The components of a vector soliton can be orthogonal polarizations [61, 62], fundamental and second harmonic components [63], or any two mutually incoherent beams [64]. The stability of spatial vector solitons has also been the subject of active investigation over the past several years [65, 66]. However, the existence and stability of ring-shaped vector solitons remains an open question.

It has been shown that it is possible to stabilize scalar ring solitons in a competing cubic-quintic $\left(\chi^{(3)} - \chi^{(5)}\right)$ medium if there is enough power in the beam [67–71]. It was found by Towers *et al.* that the stability regions of an $m = 1, 2$ soliton take up 9% and 8% of their corresponding existence regions [68]. It has also been shown that it is possible to stabilize high-power $m = 1, 2$ solitons in a material with a quadratic

nonlinearity [72, 73]. However, in all nonlinear models, it is believed that any 2-D

soliton with orbital angular momentum $m \geq 3$ or any 3-D soliton with $m \geq 2$ is not

stable [74, 75].

This problem has been extensively studied analytically and numerically in the

literature. However, very little has been done experimentally to study this instability.

Rings with $m \leq 2$ have been studied in photorefractive [76] and quadratic materials

[77], and atomic vapors [78, 79]. However, we know of no experimental studies of

beams with large $(m > 2)$ orbital angular momentum numbers. Of particular interest,

Minardi *et al.* have shown that it may be possible to use the individual solitons

generated in the break-up of vortex beams to perform optical algebraic operations [80].

It is thus of considerable importance to determine how stable ring beams are in

propagating through a nonlinear optical material.

Chapter 2

Coherent Population Oscillations

"Truly the light is sweet ..." — *Ecclesiastes 11:7*

All of the techniques for producing both fast and slow light discussed in the last chapter require complicated experimental set-ups and/or low temperatures. However, it is important in developing applications that these large group indices can be produced in a room-temperature solid. It is this feature which makes it attractive to use the "holes" or "anti-holes" that are formed in homogenously broadened absorption lines as a result of coherent population oscillations.

Spectral holes due to coherent population oscillations were first predicted in 1967 by Schwartz and Tan [81] from the solution of the density matrix equations of motion and has been described in greater detail by subsequent authors [82–84]. In 1983, Hillman *et al.* [85] observed such a spectral hole in ruby. In their experiment, they

used an argon-ion laser operating at 514.5 nm to pump population from the ground

state to the broad $^4F_2$ absorption band. Population decays from this level within a few

picoseconds to the metastable $2\overline{A}$ and $\overline{E}$ levels and eventually returns to the ground

level with a decay time T_1' of a few milliseconds. A second probe beam (or amplitude

modulation side-bands) will beat with the pump and cause the electron population

to oscillate between the ground and metastable level. Because the decay time is so

long, this oscillation will only occur if the beat frequency (δ) between the pump and

probe beams is small so that $\delta T_1 \sim 1$. When this condition is fulfilled, the pump

wave can efficiently scatter off the temporally modulated ground state population

into the probe wave, resulting in reduced absorption of the probe wave. The spectral

hole created is centered at the laser frequency and has a width of approximately

the inverse of the population relaxation time. Hillman *et al.* [85] used modulation

spectroscopy to observe this feature and measured its width to be 37 Hz (HWHM).
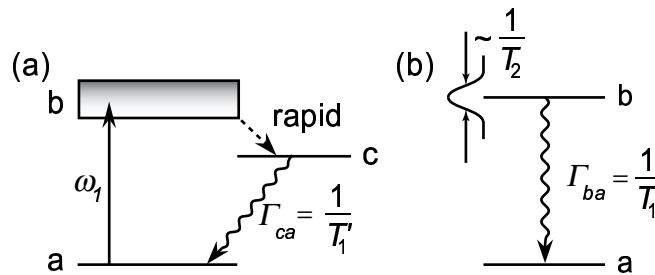
Figure 2.1: (a) A simplified version of the energy levels in ruby. Because of the
rapid decay into level c, we can model this system as the two-level atom shown in
(b).

To analyze the situation in ruby mathematically, I refer to the ground state as

level a, the $^4F_2$ absorption band as level b, and the levels $2\overline{A}$ and $\overline{E}$ as level c, as

illustrated in Fig. 2.1(a). Because of the rapid decay of level b, it is possible to reduce this system to a two-level system shown in Fig. 2.1(b). The density matrix equations of motion for this system are given by [86]

$$\dot{\rho}_{ba} = -\left(i\omega_{ba} + \frac{1}{T_2}\right)\rho_{ba} + \frac{i}{\hbar}V_{ba}w, \tag{2.1a}$$

$$\dot{w} = -\frac{w - w^{(eq)}}{T_1} - \frac{2i}{\hbar}\left(V_{ba}\rho_{ab} - V_{ab}\rho_{ba}\right), \tag{2.1b}$$

where w is the population inversion, $T_1 = T_1'/2$ is the ground state recovery time, T_1' is the lifetime of level c, T_2 is the dipole moment dephasing time, and $w^{(eq)}$ is the population inversion of the material in thermal equilibrium. The distinction between T_1 and T_1' has been discussed by Sargent [82]. The interaction Hamiltonian in the rotating-wave approximation is given by $V_{ba} = -\mu_{ba}\left(E_1 e^{-i\omega_1 t} + E_3 e^{-i\omega_3 t}\right)$, where E_1 and E_3 are the pump and probe field amplitudes, respectively, μ_{ba} is the dipole matrix element, and $\omega_3 = \omega_1 + \delta$. We seek a solution to the density matrix equation that is correct to all orders in the amplitude of the strong pump field and is correct to lowest order in the amplitude of the probe field. In this order of approximation I represent the population inversion as

$$w(t) = w^{(0)} + w^{(-\delta)}e^{i\delta t} + w^{(\delta)}e^{-i\delta t}, \tag{2.2}$$

where $w^{(0)}$ and $w^{(\pm\delta)}$ are given in Ref. [83] as

$$w^{(0)} = \frac{\left[1 + (\omega_1 - \omega_{ba})^2 T_2^2\right] w^{(eq)}}{1 + (\omega_1 - \omega_{ba})^2 T_2^2 + \Omega^2 T_1 T_2}, \tag{2.3a}$$

$$w^{(\pm\delta)} = \frac{\gamma}{2T_1} \frac{1 \mp i\delta/\beta}{\delta^2 + \beta^2}, \tag{2.3b}$$

where we have defined

$$\gamma = \frac{4T_2|\mu_{ab}|^2}{\hbar^2 \left[1 + (\omega_1 - \omega_{ba})^2 T_2^2\right]} (2E_1 E_3), \tag{2.4}$$

$$\beta = \frac{1}{T_1} + \frac{4T_2|\mu_{ab}|^2}{\hbar^2} (E_1^2) = \frac{1}{T_1} \left(1 + \Omega^2 T_1 T_2\right), \tag{2.5}$$

and the Rabi frequency

$$\Omega \equiv \frac{2|\mu_{ab}||E_1|}{\hbar} \tag{2.6}$$

to simplify notation. The response at the probe frequency can be represented as [83]

$$\rho_{ba}(\omega_1 + \delta) = \frac{\mu_{ba}}{\hbar} \frac{E_3 w^{(0)} + E_1 w^{(\delta)}}{\omega_1 - \omega_{ba} + i/T_2}. \tag{2.7}$$

Note that the first term corresponds to the interaction of the probe wave with the static part of the population difference (i.e. saturable absorption), whereas the second term represents the scattering of the pump wave off the temporally modulated ground state population. This contribution leads to decreased absorption at the probe frequency, that is, to a spectral hole in the probe absorption profile. To demonstrate

this effect, I simplify Eq. (2.7) by assuming that $\omega_1 = \omega_{ab}$, that T_2^{-1} is large compared

to the Rabi frequency and to the beat frequency $\delta \equiv \omega_3 - \omega_1$, and that $w^{(eq)} = -1$,

to find

$$\rho_{ba}(\omega_1 + \delta) = \frac{i\mu_{ba}E_3T_2}{\hbar} \left(\frac{1}{1 + \Omega^2 T_1 T_2} - \Omega^2 \frac{T_2}{T_1} \frac{1 + i\delta/\beta}{\delta^2 + \beta^2} \right). \tag{2.8}$$

We can see from the above expressions that β is the linewidth of the spectral hole.

Therefore, the amplitudes of the population oscillations are appreciable only for $\delta \leq$

$1/T_1$.

We can determine the linear susceptibility through use of Eq. (2.8) by means

of the relation $\chi(\delta) = N\mu_{ba}\rho_{ba}(\omega_3)/E_3$ and, consequently, find expressions for the

absorption and the refractive index experienced by the probe field as

$$\alpha(\delta) = \frac{\alpha_0}{1 + I_0} \left[1 - \frac{I_0(1 + I_0)}{(T_1\delta)^2 + (1 + I_0)^2} \right], \tag{2.9a}$$

$$n(\delta) = 1 + \frac{\alpha_0 c}{2\omega_1} \frac{I_0}{1 + I_0} \left[\frac{T_1\delta}{(T_1\delta)^2 + (1 + I_0)^2} \right], \tag{2.9b}$$

where $I_0 = I_1/I_{sat} \equiv \Omega^2 T_1 T_2$ is the normalized pump intensity and α_0 is the unsatu-

rated absorption coefficient.

We can plot Eqs. (2.9a) and (2.9b) under general conditions to find how it changes

with pump power. In Fig. 2.2 we can see both the power-broadened spectral hole

caused by coherent population oscillations and the decrease in total absorption from

saturable absorption. These spectral holes correspond to rapid changes in the refrac-

tive index as a function of frequency (Fig. 2.3). We can infer from Fig. 2.3 that the
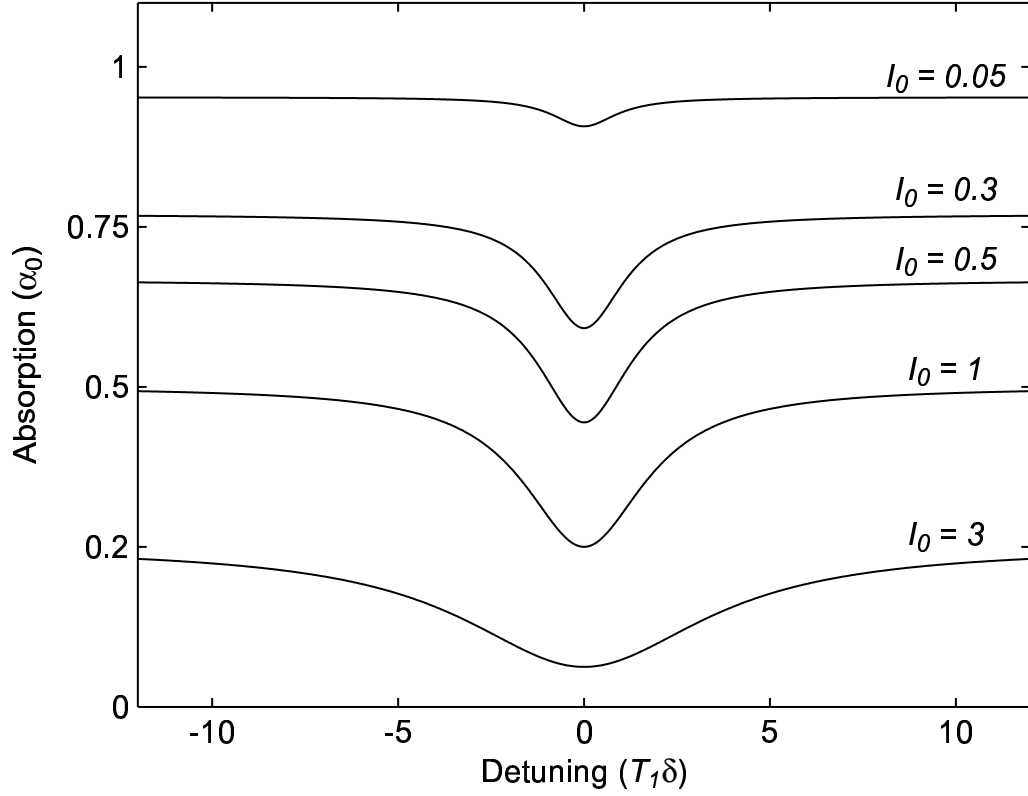
Figure 2.2: The absorption (in units of α_0) seen by the probe beam caused by coherent population oscillations found by plotting Eq. (2.9a).

dispersion is optimal when the pump intensity is equal to the saturation intensity ($I_0 = 1$). However, further analysis is necessary to verify this.

To find the group index we can rewrite Eq. (1.4) to get

$$n_g = n(\delta) + \omega_1 \frac{dn}{d\delta}. \tag{2.10}$$

This equation describes the propagation of spectrally narrow-band pulses centered at the pump frequency ω_1. For broad-band pulses, higher-order dispersion effects need to be taken into account [8]. Some of our experimental results were obtained through
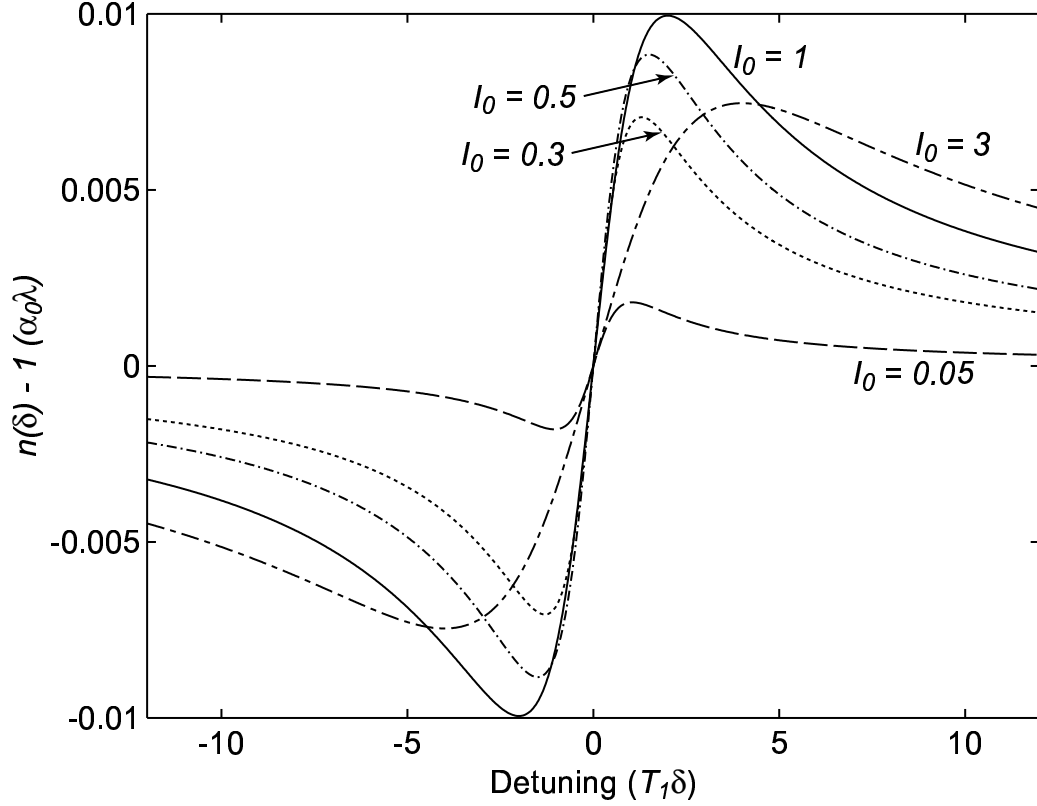
Figure 2.3: The refractive index change (in units of $\alpha_0\lambda$) seen by the probe beam caused by coherent population oscillations found by plotting Eq. (2.9b).

use of modulation techniques such that the optical field contained only a carrier wave (to act as the pump that creates the hole) and two sidebands (to act as probes). Since this field contains discrete frequencies rather than a continuum of frequencies, a generalized form of Eq. (2.10) describing the propagation of the modulation pattern through the material is given by $n_g^{\mathrm{mod}} = n_1 + \omega_1 \left[n(\delta) - n(-\delta)\right]/2\delta$, where n_1 is the refractive index experienced by the pump. Combining this with Eq. (2.9b), I obtain

$$n_g^{\mathrm{mod}} = n_1 + \frac{\alpha_0 c T_1}{2} \frac{I_0}{1 + I_0} \left[\frac{1}{\left(1 + I_0\right)^2 + \left(T_1\delta\right)^2}\right]. \tag{2.11}$$

For off-resonance modulations ($\delta \gg 1/T_1$), the modulation index reduces to $n_g^{\mathrm{mod}} \approx n_1$. Close to resonance, the expected fractional delay of the modulation as the beam propagates a distance L is

$$\varphi^{\mathrm{mod}} \simeq \frac{\alpha_0 L T_1}{4\pi} \frac{I_0}{1 + I_0} \left[\frac{\delta}{(1 + I_0)^2 + (T_1 \delta)^2} \right]. \tag{2.12}$$

If we take the derivative of Eq. (2.12) with respect to δ and set it equal to zero, we find that the modulation frequency which has the largest fractional delay is $\delta_{\mathrm{max}} = \beta = (1 + I_0)/T_1$. Putting this result back into Eq. (2.12), we find that for a given pump intensity, the maximum possible fractional delay is

$$\varphi^{\mathrm{mod}} = \frac{\alpha_0 L}{8\pi} \frac{I_0}{(1 + I_0)^2}. \tag{2.13}$$

Again we can find for what values of I_0 this expression is maximum. As anticipated from Fig. 2.3, we find that φ^{mod} is largest when $I_0 = 1$. Therefore, the largest possible fractional delay due to coherent population oscillations is

$$\varphi_{\mathrm{max}}^{\mathrm{mod}} = \frac{\alpha_0 L}{32\pi}. \tag{2.14}$$

However, I_0 depends on propagation distance because of pump absorption. As a result, the optimal input intensity is somewhat above the saturation intensity. In addition, the modulation frequency where the largest effect occurs (δ_{max}) also changes

with propagation distance.

Similarly, we can define a relative modulation attenuation $[A(\delta)]$ as the difference between the attenuation of the modulation intensity and the attenuation of the pump intensity [82, 85] or

$$A(\delta) \equiv \ln\left[\frac{I_0(L)}{I_0(0)}\right] - \ln\left[\frac{I_{\mathrm{mod}}(L)}{I_{\mathrm{mod}}(0)}\right]. \tag{2.15}$$

To find $A(\delta)$, we know from Eq. (2.9a) that the modulation intensity satisfies the equation

$$\frac{dI_{\mathrm{mod}}(z)}{dz} = -\frac{\alpha_0}{1+I_0}\left[1 - \frac{I_0(1+I_0)}{(1+I_0)^2 + (T_1\delta)^2}\right]I_{\mathrm{mod}}(z). \tag{2.16}$$

Likewise, the pump intensity satisfies the equation

$$\frac{dI_0}{dz} = -\frac{\alpha_0}{1+I_0}I_0. \tag{2.17}$$

Combining Eq. (2.17) with Eq. (2.16) we get

$$\frac{dI_{\mathrm{mod}}}{I_{\mathrm{mod}}} = \frac{dI_0}{I_0} - \frac{(1+I_0)dI_0}{(1+I_0)^2 + (T_1\delta)^2} \tag{2.18}$$

which can be exactly integrated to give

$$\ln\left[\frac{I_{\mathrm{mod}}(L)}{I_{\mathrm{mod}}(0)}\right] = \ln\left[\frac{I_0(L)}{I_0(0)}\right] - \frac{1}{2}\ln\left[\frac{(1+I_0(L))^2 + (T_1\delta)^2}{(1+I_0(0))^2 + (T_1\delta)^2}\right]. \tag{2.19}$$

Therefore, the relative modulation attenuation is

$$A(\delta) = \frac{1}{2} \ln \left[\frac{(1 + I_0(L))^2 + (T_1\delta)^2}{(1 + I_0(0))^2 + (T_1\delta)^2} \right]. \tag{2.20}$$

We use Eqs. (2.11) and (2.20) in the next few chapters to model the results of our experiments with ruby and alexandrite.

Up to this point, we have been treating the issue of coherent population oscillations purely in the frequency domain. However, it is useful to consider the time domain in order to understand the delay that a pulse may experience. Consider a strong pulse that is incident on a saturable absorber. The leading edge of the pulse will experience absorption and saturate the material. Consequently, the back of the pulse will see reduced absorption with the net result being that the re-shaped pulse is shifted backwards in time. Therefore, slow light due to coherent population oscillations may be equivalent to the Basov effect [87].

Chapter 3

Slow Light in Ruby

"Where is the way where light dwelleth?" —Job 38:19

We can utilize the results of the previous chapter to explicitly consider the effects of coherent population oscillations in ruby. In essence, we have repeated the work of Hillman *et al.* [85], but have extended their work to include the time domain. The work described in this chapter has been published in Physical Review Letters [88].

Our experimental setup is shown in Fig. 3.1. I used a single-line argon-ion laser operating at 514.5 nm as the laser source. The beam passed first through a variable attenuator and then an electro-optic modulator. The modulator was driven by a function generator which allowed us to either place a 6% sinusoidal amplitude modulation on the beam or produce long ($\sim$ ms) pulses with almost no background intensity. For all pulse lengths, these pulses had a peak power of 0.28 W with a background that was

less than 4% of that of the peak. A glass slide sent 5% of the beam to one detector for reference. The beam was then focused with a 40-cm-focal length lens to a beam waist of 84 μm near the front surface of a 7.25-cm-long ruby rod. Because the center of the beam experienced less absorption than the edges due to saturation, the beam did not expand significantly in traversing the ruby. Ruby is a uniaxial crystal, and I rotated the rod to maximize the interaction. The beam exiting the ruby was incident on a detector, and the detected signal was stored along with that of the input beam on a digital oscilloscope. The resulting traces were compared on a computer to calculate the relative delay and amplitude of the two signals.
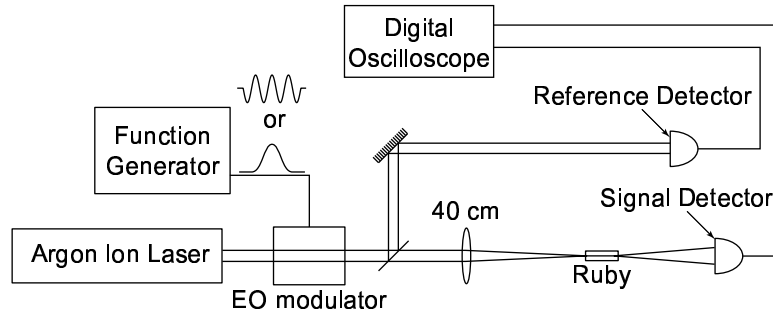
Figure 3.1: The experimental setup used to observe slow light in ruby.

To model the total group delay and modulation attenuation observed in our experiments, I first numerically calculated the value of I_0 throughout the length of the crystal. As discussed in the last chapter, the pump beam intensity depends on the propagation distance through the ruby as

$$\frac{dI_0(z)}{dz} = -\frac{\alpha_0}{1 + I_0}I_0.$$

(3.1)

Using the accepted value of 1.5 kW/cm^2 [89] for the saturation intensity of ruby at

514.5 nm, I integrated Eq. (3.1) numerically to find $I_0(z)$. Combining this function

with our theoretical model for the dispersion [Eqs. (2.11) and (2.20)], I could fit the

total delay and the relative modulation attenuation measured in our experiment. I

assumed α_0 and T_1 to be free parameters and found the values of $\alpha_0 = 1.17$ cm^{-1} and

$T_1 = 4.45$ ms. These values are in the range found by Cronemeyer [90] and others.

The total transmission in our experiments was on the order of 0.1%.
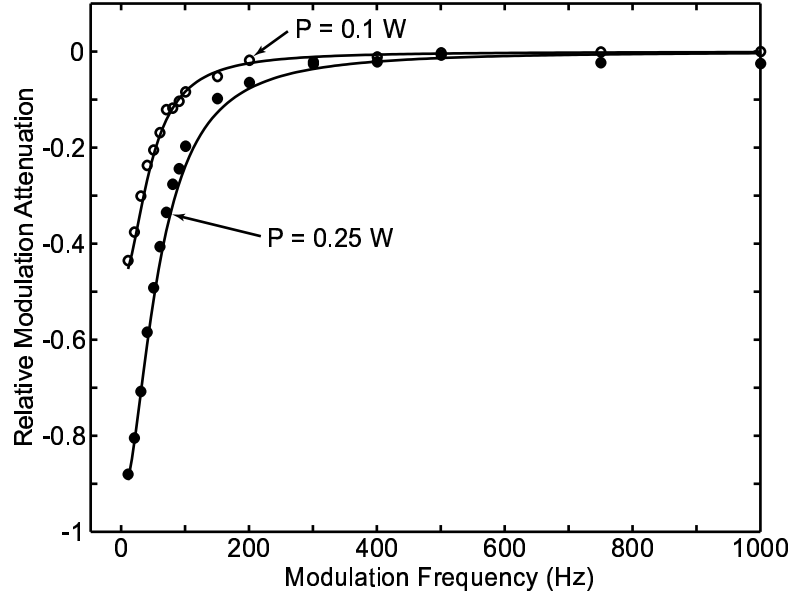
Figure 3.2: The relative modulation attenuation $A(\delta)$ with respect to the pump as a function of modulation frequency for input pump powers of 0.1 and 0.25 W. The solid lines represent the theoretical model of Eq. (2.20).

In Fig. 3.2, I show the measured relative modulation attenuation and compare it

with the numerical solution of Eq. (2.20). In the limit in which the pump field becomes

very weak, the spectral hole has a width of $1/(T_1 2\pi)$ or about 35.8 Hz (HWHM). As

the input power is increased, the hole experiences power broadening. This result is in

good agreement with the characteristics of the spectral hole that Hillman *et al.* [85] found in a 1 cm ruby.
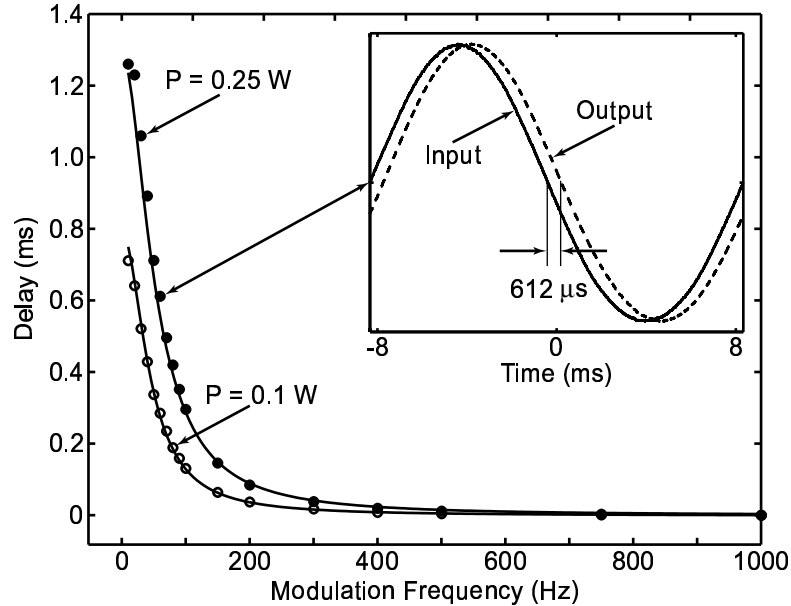
Figure 3.3: Observed time delay as a function of the modulation frequency for input pump powers of 0.1 and 0.25 W. The inset shows the normalized 60 Hz input (solid line) and output (dashed line) signal at 0.25 W. The 60 Hz signal was delayed 612 μs corresponding to an average group velocity of 118 m/s.

This spectral dip causes an amplitude modulated beam to experience a large group index. I show the delay experienced by the modulation in Fig. 3.3 for input pump powers of 0.1 and 0.25 W. I observed the largest delay, $1.26 \pm .01$ ms, with an input pump power of 0.25 W, which corresponds in Fig. 3.2 to the power where the spectral hole is deepest but still very narrow. The inferred group velocity at this power is 57.5 ± 0.5 m/s. Note that the group velocity can be controlled by changing the modulation frequency or the input intensity. I found the nature of the effect to be strongly intensity dependent in that by moving the ruby a small distance from

the focus I could greatly decrease the measured delay. As a check of my results, I found that the time delay would completely disappear if I moved the ruby far from the focus. Note that the modulation frequency with the largest fractional delay was $1/(\pi T_1) \sim 60$ Hz as we would expect. Also, the fractional delay at this frequency (3.7%) was comparable to what we would expect from Eq. (2.14).
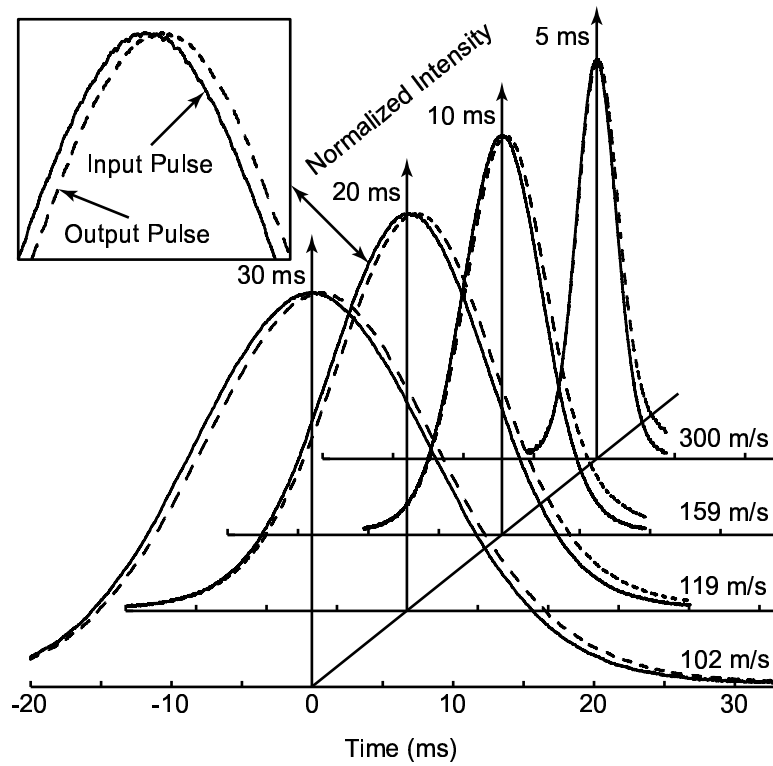
Figure 3.4: The normalized input and output intensities of a 5, 10, 20, and 30 ms pulse. The corresponding average group velocities of the pulses are 300, 159, 119, and 102 m/s. The inset shows a close-up of the 20 ms pulse.

Moreover, I have found that it was not necessary to apply separate pump and probe waves to the ruby crystal in order to observe slow light effects. A single intense pulse of light was able to provide the saturation required to modify the group index to provide slow light propagation. These relatively intense pulses can be thought

of as producing their own pump field and are thus self-delayed. I know of no other examples where a separate pump beam is not required for generating ultraslow light. For this experiment, I used the programmable pulse generator to produce gaussian pulses with a $1/e$ intensity full width of 1 to 30 ms with almost no background, and I observed how they were delayed in propagating through the ruby. I found that the longer pulses also had the longer delays with the center of mass of a 30 ms pulse delayed by 0.71 ms with little pulse distortion. I show this result and those for other pulse lengths in Fig. 3.4. While the theory developed in the last chapter, which assumed the presence of distinct CW pump and probe fields, does not model this pulsed experiment directly, that theory can be used to gain some intuition regarding the experiment. For instance, we would expect longer pulses, which contain lower frequency components, to experience longer delays. In addition, very short pulses with high frequency components would be expected to travel through the ruby with very little delay. As can be seen in Fig. 3.4, this insight is correct.

Chapter 4

Fast Light in Alexandrite

"... the light is short because of darkness." — Job 17:12

Whereas a spectral hole from coherent population oscillations in a homogenously broadened absorption line can cause slow light, an "anti-hole" should cause fast light. Such an anti-hole with a measured width of 612 Hz was observed by Malcuit *et al.* in alexandrite at 457 nm [91]. This "anti-hole" forms instead of a hole since alexandrite is inversely saturable from roughly 450-510 nm due to excited state absorption [92]. However an anti-hole is not the only feature that can be seen within that wavelength range. Alexandrite is formed by doping a $BeAl_2O_4$ crystal with Cr^{3+} ions, and these ions replace the Al^{3+} ions [93]. However, not all of the ion sites are identical. Namely, 78% of the sites occupied by the Cr^{3+} ions have mirror symmetry (C_s), and the rest have inversion symmetry (C_i) [94]. As a result, the ground-state absorption cross

sections σ_1, population relaxation times T_1, and the saturation intensities $I_s \equiv \frac{\hbar\omega}{\sigma_1 T_1}$ are different at each site (see Fig. 4.1). Ions at mirror sites have a relaxation time of 290 μs, and ions at inversion sites have a relaxation time of $\sim$50 ms [94]. The measurements suggest that the mirror-site ions have a large excited-state absorption cross section σ_2, whereas the inversion-site ions experience negligible excited-state absorption. I reached this conclusion because the width of the anti-hole (which is a consequence of excited-state absorption) is the inverse of 290 μs whereas the width of the spectral hole (which does not involve excited-state absorption) is approximately the inverse of 50 ms. The relative size of the hole or anti-hole depends on the absorp-
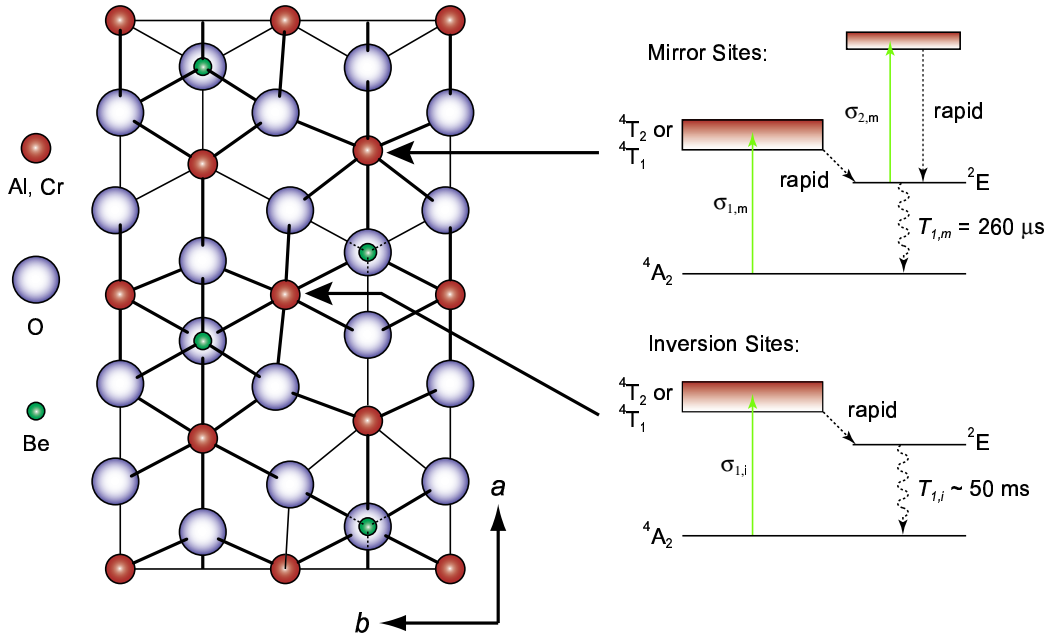
Figure 4.1: The crystal structure of alexandrite looking along the c axis, after Ref. [93]. The arrows indicate the locations of ion sites that have mirror or inversion symmetry. On the right are the corresponding energy-level diagrams for Cr^{3+} ions at the different sites. Mirror-site ions experience excited-state absorption and have a population relaxation time of 260 μs. Inversion-site ions have negligible excited-state absorption and a much longer population relaxation time ($\sim$50 ms).

tion cross sections for each site at a given wavelength.

The setup for this experiment was nearly identical to what is shown in Fig. 3.1. However this time I operated the argon-ion laser at either 457, 476, or 488 nm. Also, the beam was focused with a 20-cm-focal length lens and the alexandrite crystal was 4.0 cm long. The orientation of the crystal was such that the light was polarized parallel to the a axis. The transmitted beam went through an interference filter to remove any signal caused by the fluorescence from electrons decaying from ^{2}E to the ground state and then fell onto a detector. The detected signal was stored along with that of the reference beam on a digital oscilloscope, and the resulting traces were compared on a computer to calculate the relative delay and amplitude of the two signals.

To model our results, I considered the influence of ions at both the inversion sites and the mirror sites. In addition, the absorption cross sections should be different at different wavelengths. For a given wavelength and a given ion site, we can refer to Eqs. (2.9) to find the refractive index and probe beam absorption as functions of the probe beam detuning δ,

$$n(\delta) \; = \; 1 + \frac{\alpha_0 c}{2\omega_1} \frac{I_0}{1 + I_0} \left[\frac{\delta T_1}{(T_1 \delta)^2 + (1 + I_0)^2} \right],$$
$$\alpha(\delta) \; = \; \frac{\alpha_0}{1 + I_0} \left[1 - \frac{I_0 (1 + I_0)}{(T_1 \delta)^2 + (1 + I_0)^2} \right],$$

Since the mirror-site ions experience excited-state absorption, I can replace the un-

saturated absorption coefficient α_0 for these sites with $N(\sigma_1 - \sigma_2)$, where N is the ion density. Also, I assume that the inversion-site ions experience negligible excited-state absorption and have a different saturation intensity than mirror-site ions. Now I can modify Eqs. (2.9) by including a term from both the mirror sites and the inversion sites to get

$$
\begin{aligned}
n(\delta) &= 1 + \frac{Nc}{2\omega_1} \left\{ \rho_m(\sigma_{1,m} - \sigma_{2,m}) \frac{I_{0,m}}{1 + I_{0,m}} \left[\frac{T_{1,m}\delta}{(T_{1,m}\delta)^2 + (1 + I_{0,m})^2} \right] \right. \\
&\quad \left. + \rho_i \sigma_{1,i} \frac{I_{0,i}}{1 + I_{0,i}} \left[\frac{T_{1,i}\delta}{(T_{1,i}\delta)^2 + (1 + I_{0,i})^2} \right] \right\},
\end{aligned}
\tag{4.2}
$$

$$
\begin{aligned}
\alpha(\delta) &= \frac{\rho_m N(\sigma_{1,m} - \sigma_{2,m})}{1 + I_{0,m}} \left[1 - \frac{I_{0,m}(1 + I_{0,m})}{(T_{1,m}\delta)^2 + (1 + I_{0,m})^2} \right] + N\rho_m \sigma_{2,m} \\
&\quad + \frac{\rho_i N \sigma_{1,i}}{1 + I_{0,i}} \left[1 - \frac{I_{0,i}(1 + I_{0,i})}{(T_{1,i}\delta)^2 + (1 + I_{0,i})^2} \right],
\end{aligned}
\tag{4.3}
$$

where the subscripts m or i indicate the parameter is for the mirror or inversion sites and ρ is the percentage of ions at a given site. As I did for ruby, I calculated numerically the intensity throughout the crystal and used these equations to find the expected delay and attenuation of the modulated signal. I found the best fit for the data using the parameters $N = 9 \times 10^{19}$ cm^{-3}, $T_{1,m} = 280$ μs, and $T_{1,i} = 19$ ms. The discrepancy between $T_{1,i}$ in our model and in the literature (19 ms compared with 50 ms) may possibly be explained by the temperature dependence of T_1 in alexandrite [94]. The rest of these parameters are within the range of accepted values [92, 94]. I

give the absorption cross sections that I used for each wavelength below. This work

has been published in Science [95].

Figure 4.2: The (a) relative modulation attenuation and (b) delay found in a 4-cm alexandrite crystal at a wavelength of 457 nm with a pump power of 320 mW. The observed negative time delay corresponds to superluminal propagation. The solid lines indicate the results of the theoretical model.

We independently measured the probe absorption and modulation delay as func-

tions of frequency, and then display both of them to demonstrate the self-consistency

of the experimental data. These results are summarized in Figs. 4.2 through 4.4. In

Fig. 4.2, I show the relative modulation attenuation (as defined in Chap. 2) and the

modulation delay for a pump power of 320 mW at a wavelength of 457 nm. This is the original wavelength used by Malcuit *et al.* [91]. At this wavelength, the absorption is almost completely dominated by the mirror sites. As a result, the modulation attenuation that I saw is comparable to what was observed by Malcuit *et al.* However, there is possibly some small influence of the inversion sites observable primarily in the negative delay almost going to zero. In the modelling of these results, I used the values $\sigma_{1,i} = 0.1 \times 10^{-20}$ cm^2, $\sigma_{1,m} = 2.8 \times 10^{-20}$ cm^2, and $\sigma_{2,m} = 4.9 \times 10^{-20}$ cm^2. We noted that the beam transmission at this wavelength was small ($< 0.1\%$) which motivated us to look at the other laser lines of the argon-ion laser.

In Fig. 4.3, I again show the relative modulation attenuation and the accompanying delay, only this time at 476 nm and at two different pump power levels. At this wavelength, the inversion sites play a much larger role, and their influence is observable both in the small narrow dip in the relative modulation attenuation and in the corresponding positive delay at low modulation frequencies. This effect is in good agreement with the work of Schepler [96] who found that the inversion site contribution to the fluorescence intensity becomes significant from about 470-520 nm. I observed an advancement of the waveform as large as 50 μs which corresponds to a group velocity of -800 m/s and a group index of -3.75×10^5. The measured transmission was about 3.5%. In the modelling of these results, I used the values $\sigma_{1,i} = 0.35 \times 10^{-20}$ cm^2, $\sigma_{1,m} = 0.9 \times 10^{-20}$ cm^2, and $\sigma_{2,m} = 4.05 \times 10^{-20}$ cm^2. Using these numbers I found reasonably good agreement with the experimental data.
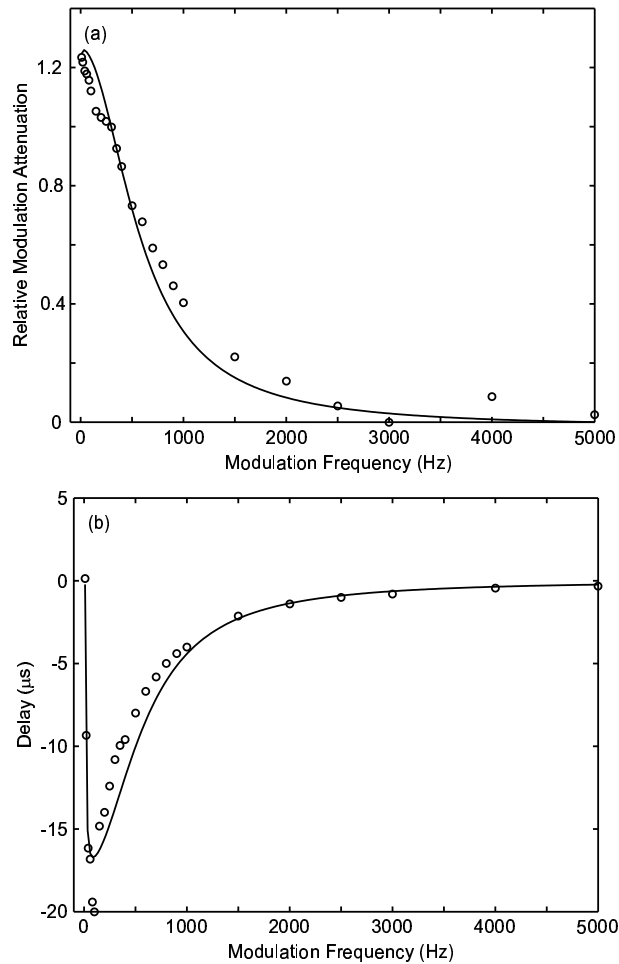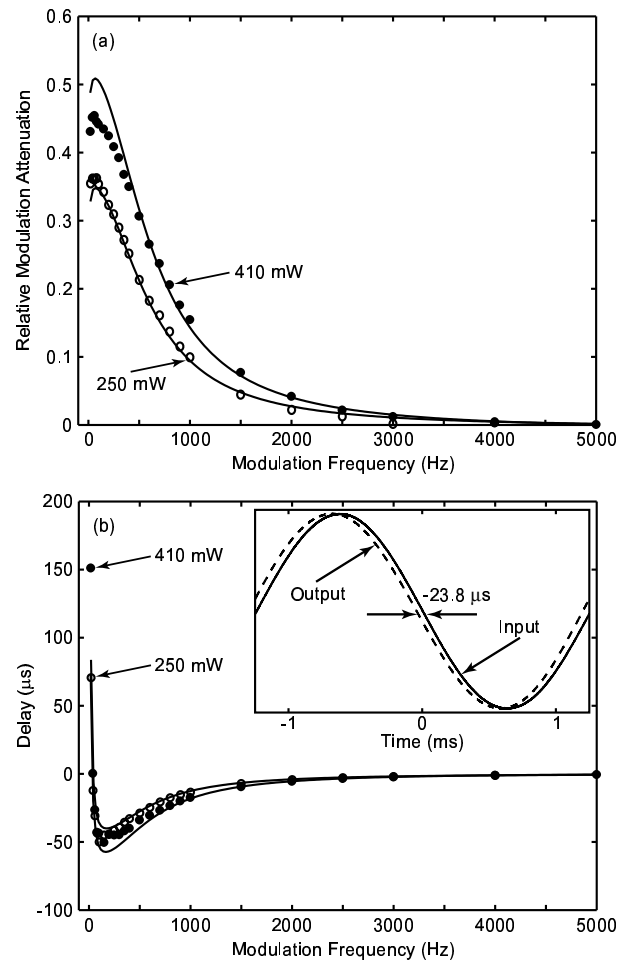
Figure 4.3: The (a) relative modulation attenuation and (b) delay found in a 4-cm alexandrite crystal at a wavelength of 476 nm with a pump power of 250 and 410 mW. The solid line indicates the results of the theoretical model. The inset in (b) shows the normalized output signal at 800 Hz leading the input signal by 23.8 μs.

Finally, in Fig. 4.4 I show the same data at a wavelength of 488 nm. At this wavelength the effect of the inversion sites dominate, and produce a very narrow dip in the absorption at low frequencies. The peak in the delay shown in Fig. 4.4 corresponds to an average group velocity of 148 m/s, but I also observed group velocities as low as 91 m/s with a higher pump power (950 mW). The transmission at this wavelength
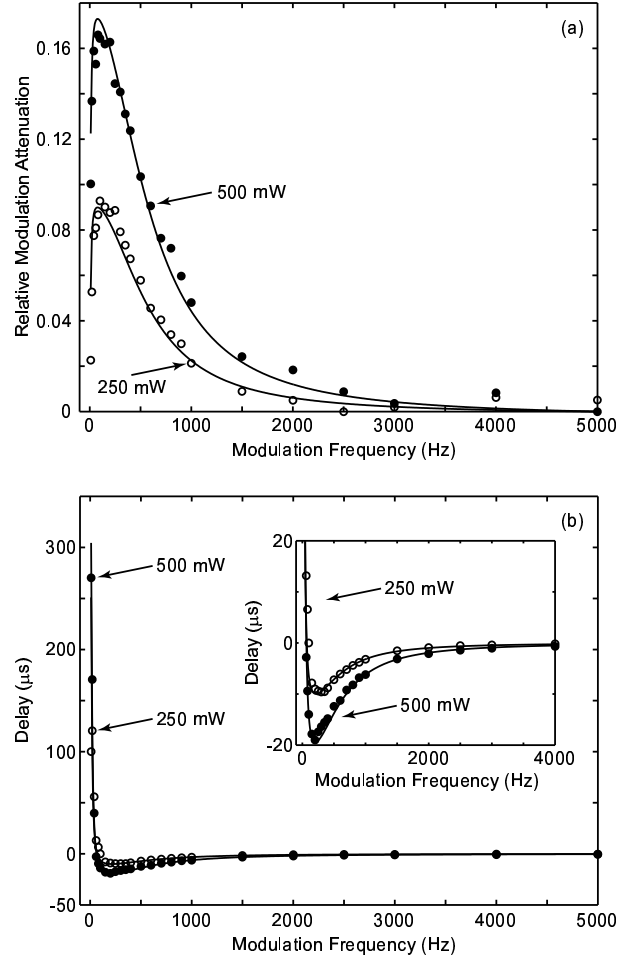
Figure 4.4: The (a) relative modulation attenuation and (b) delay found in a 4-cm alexandrite crystal at a wavelength of 488 nm with a pump power of 250 and 500 mW. The solid line indicates the results of the theoretical model. Note that ultra-slow propagation occurs for low modulation frequencies (< 60 Hz), and that superluminal propagation occurs at higher frequencies. The inset in (b) is a close-up of the same data.

was more than 10%. As can be seen from the insert in Fig. 4.4(b), we have excellent agreement with our numerical model at this wavelength using the parameters $\sigma_{1,i} = 0.4 \times 10^{-20}$ cm^2, $\sigma_{1,m} = 0.9 \times 10^{-20}$ cm^2, and $\sigma_{2,m} = 3.5 \times 10^{-20}$ cm^2.

These experiments show that it is possible to advance an amplitude modulated signal. I found that is was also possible to advance a pulse. To do this, I adjusted

the electro-optic modulator to produce a pulse on the CW beam. The average power was 330 mW and the pulse had a peak that was 16% of the background power. The laser was tuned to the 476 nm line because the largest advancement was observed at that wavelength. I found that the center-of-mass of a 1 ms pulse could be advanced as much as 43 μs with very little distortion (see Fig. 4.5).
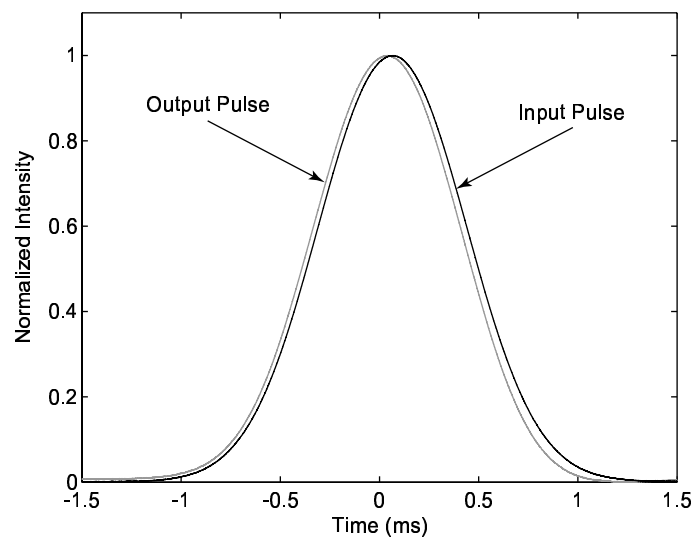
Figure 4.5: The input (solid) and output (dashed) signal for a 1 ms pulse at 476 nm. The output is advanced by 43 μs.

In conclusion, we have demonstrated that either ultra-slow or superluminal light propagation can be achieved in the same solid-state material by changing the excitation wavelength. This phenomenon occurs as a result of coherent population oscillations between the ground and excited states in an alexandrite crystal. We find that we have to take account of the different absorption characteristics of Cr^{3+} ions in mirror or inversion sites to interpret our results.

Chapter 5

Information Velocity in Ruby and Alexandrite

"We wait for light, but behold obscurity." — *Isaiah 59:9*

Because of their simplicity, the systems discussed in the previous chapters are ideal for studying the information velocity in a material with a large positive or negative group velocity. While a liability from an applications standpoint, the narrow linewidths found in these systems allow us to use ruby and alexandrite as a test-bed to study pulse propagation in detail.

Before any discussion of information velocity can begin, a working definition of information velocity must be established. It is helpful to first define an information arrival time. In this work, I define the information arrival time as the earliest possible

time one can observe a "change" in the electromagnetic field that propagates through a system. This change in the electromagnetic field must correspond to a clear physical change in the atoms generating the field (e.g. turning on the laser). Therefore, if L is the distance between where the physical change takes place and the detector, the information velocity is L divided by the information arrival time. This definition of information velocity is equivalent to the speed of nonanalytic points as proposed by Chiao and Steinberg [35]. Obviously, this definition is also the one that Sommerfeld had in mind when he made the statement I quoted in Chap. 1.

In the next sections, I study how the width of the incident pulse influences the shape of the transmitted pulse for alexandrite and ruby. We find that as we decrease the pulse width, higher-order dispersion becomes significant as the bandwidth of the pulse becomes comparable to the spectral width of the interaction region of the material. These higher-order effects cause pulse distortion. When the pulse bandwidth becomes much larger than the spectral width of the interaction region, the pulse velocity becomes luminal (equal to c/n where n is the background refractive index of the sapphire or chrysoberyl crystal) and the distortion disappears. In addition, I study the propagation of nonanalytic pulses and show that the velocity of a discontinuity is luminal. From these results I conclude that the information velocity is equal to c/n in both systems.

I should mention that in this chapter that the distinction between a velocity c and a velocity c/n is not important because the change in the group index due to the

chromium ions can be as much as six orders of magnitude larger than the background index. Also, since my input signals are relatively slow, I cannot resolve the difference in arrival time between c and c/n. Finally, these results are general enough that they should be scalable. If I could produce (and detect) signals that were fast enough to be comparable to the response time of the (undoped) crystals, I should see similar results.

5.1 Impulse Response Function

In this section, I develop a model of pulse propagation for these systems. While it is possible to fully solve the density matrix equations in ruby and alexandrite [97], and thereby find how a pulse shape is changed in the interaction, there is a simpler way. As noted by Macke and Ségard [98], it is possible to model a fast (or slow) light system with an impulse response function. They found that this model is particularly useful for the case of multiple resonances, but we can modify their model to fit our system. In the notation of Macke and Ségard we can write the electric field $\mathcal{E}(z,t)$ as

$$\mathcal{E}(z,t) = \Re \left[E(z,t) e^{i\omega_0 t} \right], \tag{5.1}$$

where $E(z,t)$ is the complex pulse envelope and ω_0 is the mean pulse frequency. The transmitted pulse envelope after travelling a distance Δz through a material is related

to the initial pulse shape through an impulse response function $h(t)$ as

$$E(z + \Delta z, t) = h(t) \otimes E(z, t), \tag{5.2}$$

where '$\otimes$' indicates a convolution operation. Correspondingly, we can relate the initial
and final pulse spectra with a transfer function $H(\Omega)$ so that

$$
\begin{aligned}
\widehat{E}(z + \Delta z, \Omega) &= H(\Omega)\widehat{E}(z, \Omega) \\
&= e^{\Gamma(\Omega)}\widehat{E}(z, \Omega) \\
&= e^{F(\Omega)}e^{i\varphi(\Omega)}\widehat{E}(z, \Omega), \tag{5.3}
\end{aligned}
$$

where $\Gamma(\Omega)$ is the complex gain factor, $F(\Omega)$ is the real amplitude absorption factor,
and $\varphi(\Omega)$ is the complex phase. The pulse envelope spectrum $\widehat{E}(z, \Omega)$ is the Fourier
transform of the pulse envelope, and likewise, the transfer function $H(\Omega)$ is the Fourier
transform of the impulse response function. As an example, we consider a material
with a single resonance. If we assume that ω_0 is equal to the resonance frequency,
the complex gain factor becomes

$$\Gamma(\Omega) = -\frac{\alpha \Delta z / 2}{1 + i\Omega/\gamma}, \tag{5.4}$$

where α is the intensity absorption coefficient and γ is the relaxation rate.

The system we want to model is only slightly more complicated. We do not

have a single resonance line, but the spectral hole (or anti-hole) caused by coherent

population oscillations is Lorentzian. As a result, the functional form is the same.

Using Eq. (2.9a), we can see that the complex gain factor is

$$\Gamma(\Omega, I_0) = \frac{\alpha_0 \Delta z}{2(1 + I_0)} \left[1 - \frac{I_0}{(1 + I_0) + iT_1\Omega} \right], \tag{5.5}$$

where, as before, α_0 is the unsaturated intensity absorption coefficient, I_0 is the

normalized pump intensity, and T_1 is the population relaxation time. Note that,

unlike the case with a resonance line [Eq. (5.4)], the complex gain factor depends on

pump intensity. As a result, the modified pulse shape must be calculated step-wise

throughout the length of the material. From Eq. (5.5), we see that the complex phase

is

$$\varphi(\Omega, I_0) = \frac{\alpha_0 \Delta z}{2} \frac{I_0}{1 + I_0} \frac{T_1\Omega}{(1 + I_0)^2 + (T_1\Omega)^2}. \tag{5.6}$$

From this we can find that the refractive index that a pulse will see over a distance

Δz is

$$\Delta n(\Omega) = \frac{\alpha_0 c}{\omega_0 \Delta z} \int_0^{\Delta z} \frac{I_0}{1 + I_0} \frac{T_1\Omega}{(1 + I_0)^2 + (T_1\Omega)^2} dz. \tag{5.7}$$

Likewise, the amplitude absorption factor is

$$F(\Omega, I_0) = \frac{\alpha_0 \Delta z}{2} \left[\frac{1}{(1 + I_0)} - \frac{I_0}{(1 + I_0)^2 + (T_1\Omega)^2} \right]. \tag{5.8}$$

Correspondingly, we can express the intensity attenuation seen by the pulse (neglect-

ing background absorption) as

$$A_{\text{pulse}}(\Omega) = -\alpha_0 \int_0^{\Delta z} \frac{I_0}{(1 + I_0)^2 + (T_1\Omega)^2} dz. \tag{5.9}$$

It can be shown that this expression is equivalent to the relative modulation attenu-

ation (as defined in Chap. 2).

5.2   Pulse Distortion

For a pulse with a bandwidth much smaller than the region of large dispersion, the

output pulse envelope will have the form

$$E'(z + \Delta z, t) = E(z, t - \theta), \tag{5.10}$$

where θ is the delay of the pulse travelling through the material and $E'(z, t)$ is the

output field envelope that has been normalized to ignore background absorption. The

value for θ can be defined as the delay of the center-of-mass of the envelope of the

output pulse [98], but due to the nature of the distortion found in my experiments, I

found it most useful to set the value of θ equal to the delay of the peak of the pulse.

If the bandwidth of the pulse starts to become significant relative to the range of

large dispersion, we should expect that the pulse will become distorted. The degree

of pulse distortion can be characterized in a slightly modified form of Eq. (22) in

Ref. [98] as

$$D = \left(\frac{\int_{-\infty}^{+\infty} ||E'(z + \Delta z, t)|^2 - |E(z, t - \theta)|^2| dt}{\int_{-\infty}^{+\infty} |E(z, t)|^2 dt} \right)^{\frac{1}{2}}. \tag{5.11}$$

Note that D is equal to zero when the pulse is undistorted. This equation, when applied to our results, produces an offset from zero due to noise. Nevertheless, I found that Eq. (5.11) is a useful characterization of the pulse distortion for both pulse delays or advances (i.e. θ either positive or negative).

5.3 Information Velocity in a Fast Light Material

I first conducted an experiment with gaussian pulses in alexandrite to investigate
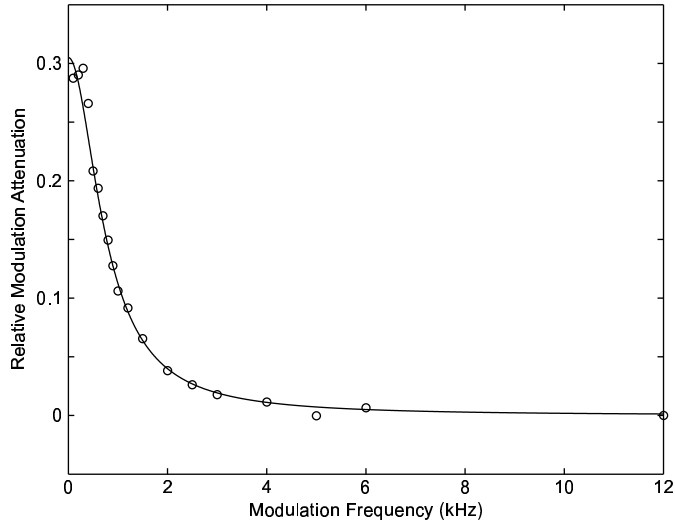
Figure 5.1: The relative modulation attenuation under the conditions used to study pulse propagation in alexandrite. The solid line is the solution to Eq. (5.9).

the information velocity in a material with a superluminal group velocity. In this experiment, the pulses are on a large background (580 mW) which acts as the pump,

and the wavelength of the light was 476 nm because that was the wavelength I had found to have the largest fractional advancement [95]. The background acts as a pump with the superimposed pulse acting as a probe. Also, the polarization of the light was rotated so that the influence of inversion sites (i.e. slow light) was small. This can be seen in Fig. 5.1 where I again measured the relative modulation attenuation under this configuration.

I then measured the peak advancement and calculated the distortion [Eq. 5.11] for a range of different pulse lengths. These results are shown in Fig. 5.2. The fractional

Figure 5.2: (a) The fractional advancement of the peak of a gaussian pulse as a function of pulse width (FWHM) in alexandrite. (b) The distortion [as defined in Eq. (5.11)] experienced by the pulse in transmission through the alexandrite as a function of pulse width.

advancement is defined as the ratio of pulse advancement to pulse width (FWHM).

In Fig. 5.3, the figures in the left column show a representative sample of input and output intensities of gaussian pulses with several different pulse widths. The plots in the right column are the numerical results of the impulse response model with the same parameters as the experiment. As can be seen, the agreement is very
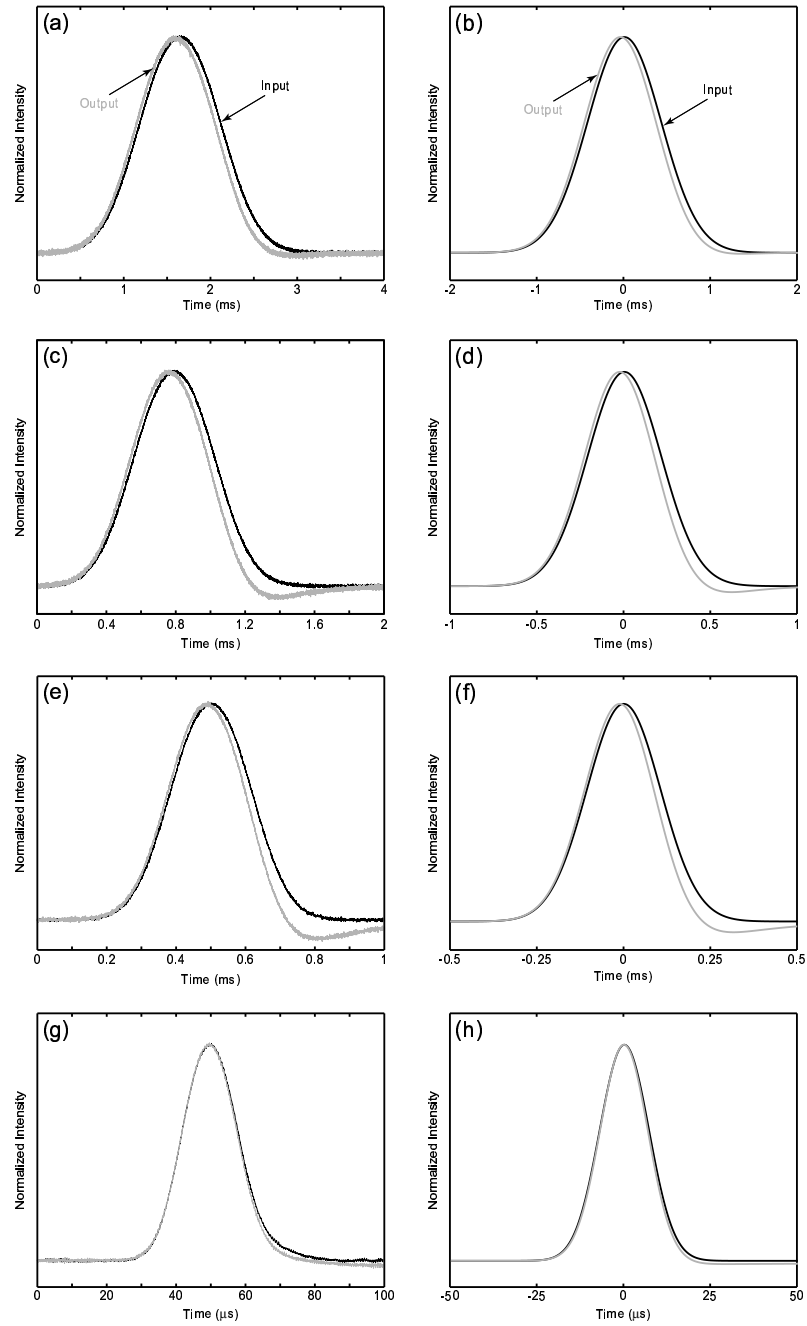
Figure 5.3: The input (black) and output (gray) intensity for gaussian pulses with different pulse widths. The left column shows the experiment and the right column shows the impulse response model. The pulse widths are 1 ms [(a) and (b)], 0.5 ms [(c) and (d)], 0.25 ms [(e) and (f)], and 16.7 μs [(g) and (h)].

good. In addition, Fig. 5.3 illustrates the initial increase and then decrease in pulse

distortion as the pulse width is decreased as seen in Fig. 5.2(b).
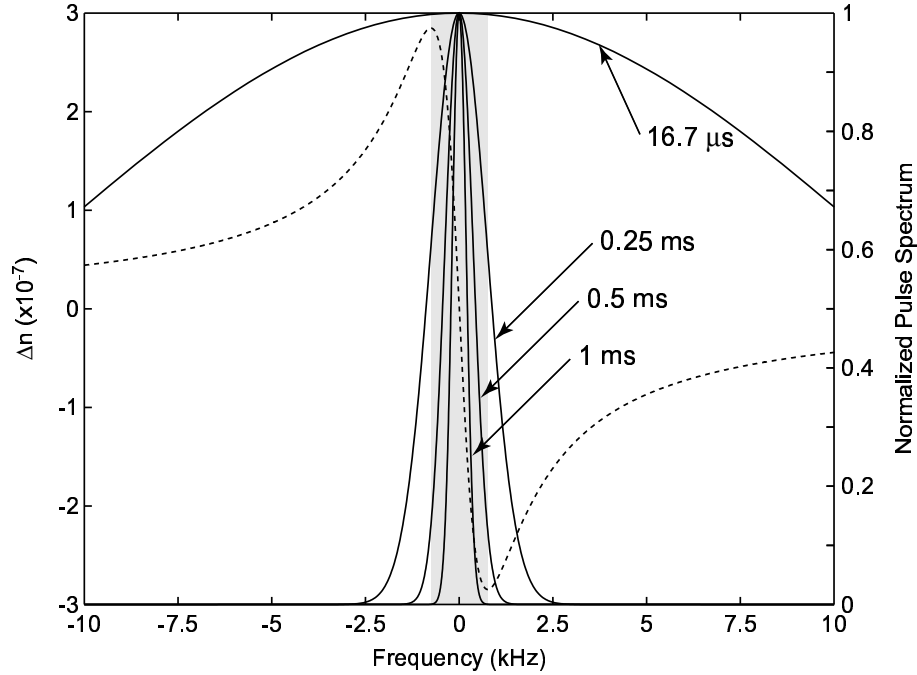
Figure 5.4: The spectra (solid lines) and the change in refractive index (Δn) induced by the strong pump beam (dashed line) for the different pulse widths shown in Fig. 5.3. The dashed line is the solution to Eq. (5.7). The gray region shows the range of large anomalous dispersion.

In Fig. 5.4, we compare the initial pulse spectrum with the region of large anomalous dispersion. The change in the refractive index induced by the strong pump beam [calculated from Eq. (5.7)] is shown as the dashed line. We can see that when the pulse width is large, most of the spectrum is within the region of large anomalous dispersion (gray shaded region). Comparing this with Fig. 5.2, we see that this is also when the fractional advancement is large and the pulse distortion is small. However, when the pulse width becomes too narrow, the pulse bandwidth becomes too large

to interact with the spectral feature. As a result, this entire narrow pulse can be thought of as a 'front' which travels at c/n through the alexandrite.

To further study the propagation of fronts, I experimentally investigated the propagation of different pulse shapes in alexandrite. Specifically, I considered two types of nonanalytic pulses. I chose to look at nonanalytic pulses since Chiao and Steinberg [35] have shown that points that are nonanalytic travel exactly at c in any material. As a result, they equate this velocity with the group velocity.

The intensity profile of the first nonanalytic pulse was

$$I(t) = I_{\text{peak}} \left\{ 1 - \exp\left[-\ln\left(\frac{2}{2 - \sqrt{2}} \right) \frac{(\tau_p/2)^2}{t^2} \right] \right\}^2, \tag{5.12}$$

where τ_p is the pulse width (FWHM), and I_{peak} is the peak intensity. Note that although this function is nonanalytic at its peak ($t = 0$), the intensity is continuous and smooth at that point. As a result, unlike the work of Stenner *et al.* [12], it is not possible to trace the point that is nonanalytic since it is only undefined in a purely mathematical sense. Eq. (5.12) is an example of a function that has points that are nonanalytic which do not correspond to infinite frequency components in the Fourier domain.

The same basic pattern that was seen in Fig. 5.3 is visible in these pulses. Again we see that the long pulses are significantly advanced, and that short pulses have very little advancement [Fig. 5.5(a)]. Also, we see in Fig. 5.5(b) that the distortion is largest at pulses at intermediate widths. We note that the maximum observed
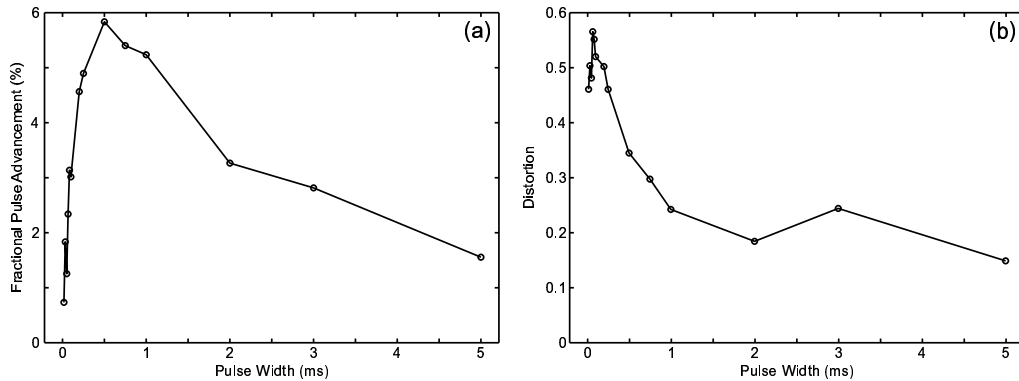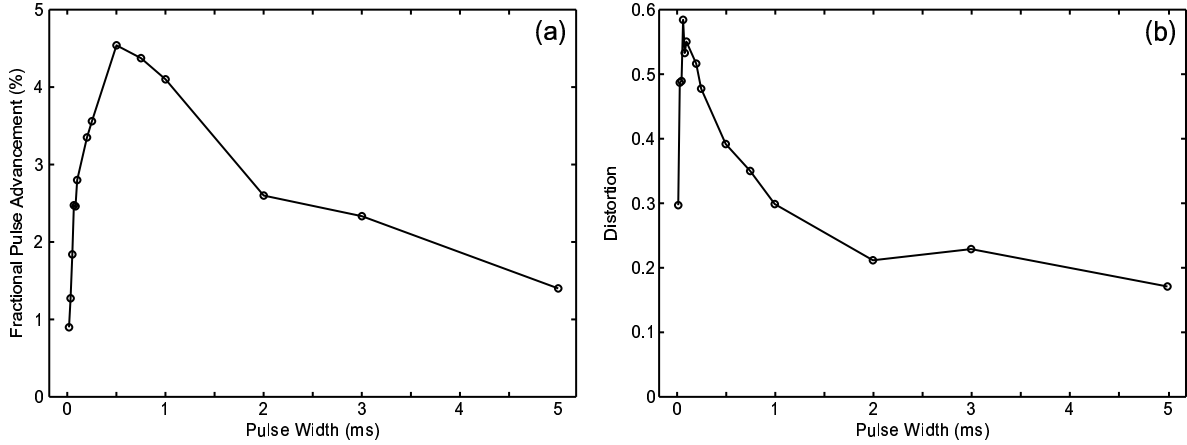
Figure 5.5: (a) The fractional advancement of a nonanalytic pulse as a function of pulse width in alexandrite. (b) The distortion [as defined in Eq. (5.11)] experienced by the pulse in transmission through the alexandrite as a function of pulse width.

distortion for these pulses is slightly larger than what was observed for gaussian pulses.

I show in Fig. 5.6 what these pulses look like before and after they travel through alexandrite. They resemble super-gaussian pulses, and because of their associated higher frequency components, they are more heavily distorted than gaussian pulses with the same widths.

The second nonanalytic pulse shape that I sent through the alexandrite resembled the '0'-pulse that Stenner *et al.* [12] used in their experiments. The first half of the input pulse is gaussian, but at the peak, the intensity rapidly drops to zero. As can be seen in Fig. 5.7, the leading edge and peak of the pulse is advanced, but the 'front' is not. We then conclude that the information velocity in alexandrite is equal to c/n.
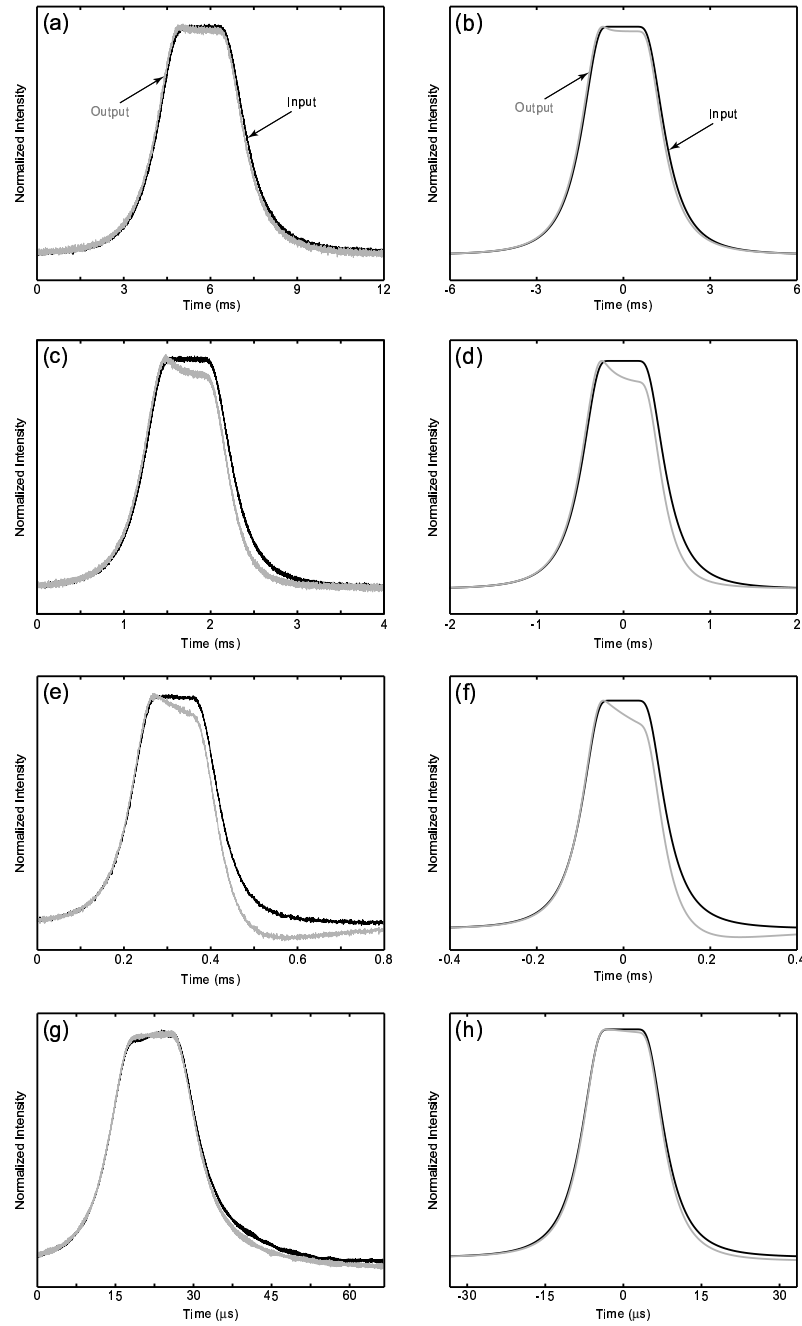
Figure 5.6: The input (black) and output (gray) intensity for nonanalytic pulses with different pulse widths. The left column shows the experiment and the right column shows the results of the impulse response model. The pulse widths are 3 ms [(a) and (b)], 1 ms [(c) and (d)], 0.2 ms [(e) and (f)], and 16.7 μs [(g) and (h)].
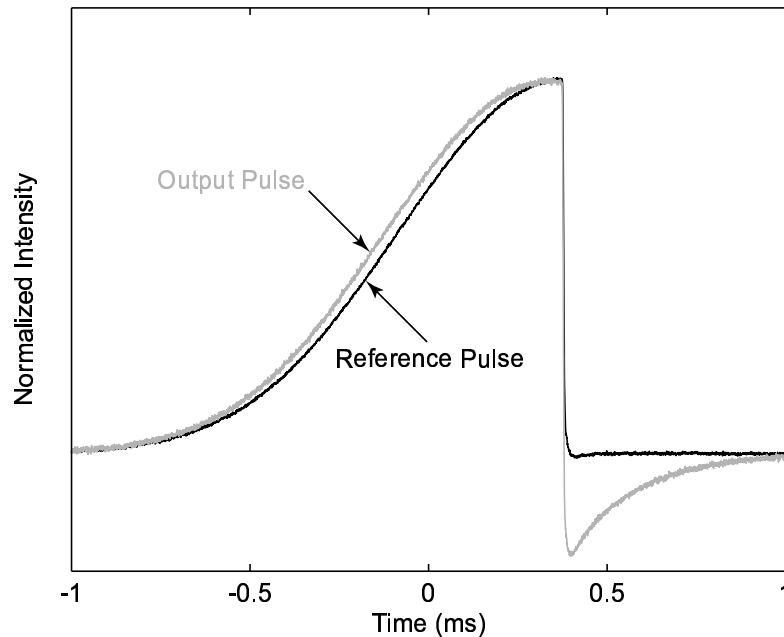
Figure 5.7: The input and normalized output intensity of a '0'-pulse in alexandrite. Without the sharp cutoff, the pulse would have had a width (FWHM) of 1 ms. Note that while the slowly varying leading edge of the pulse experiences a measurable pulse advancement, the abrupt trailing edge does not. Thus, although the group velocity is negative, the information velocity is seen to be c/n.

5.4 Information Velocity in a Slow Light Material

I continued the study of information velocity by investigating the analogous effects in ruby. We shall see that when it comes to information velocity, fast and slow light are completely equivalent. As with alexandrite, let us first consider the propagation of gaussian pulses through ruby. The difference between these pulses and the pulses shown in Fig. 3.4 is that I have modified the experimental set-up so that the pulses have a large background (230 mW). Also, since we had cut the original ruby into three pieces, I used a shorter lens (25 cm) to focus into the largest remaining piece (4.25 cm). Other than that, the setup is the same as shown in Fig. 3.1.
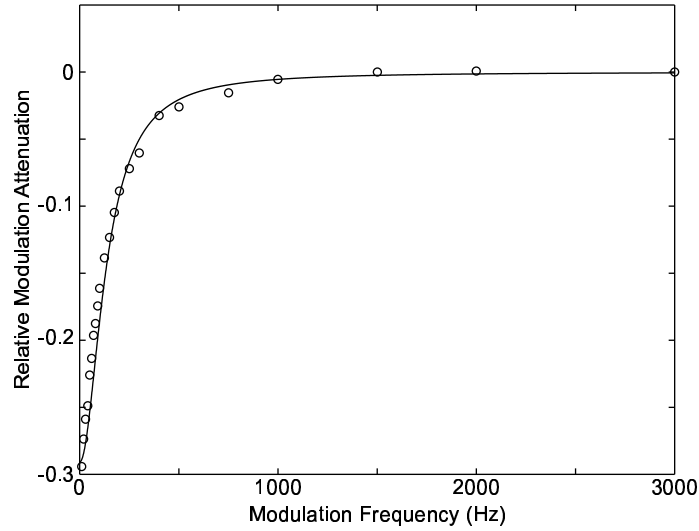
Figure 5.8: The relative modulation attenuation under the conditions used to study pulse propagation in ruby. The solid line is the solution to Eq. (5.9).

As before, I remeasured the spectral hole in ruby with this new configuration (Fig. 5.8). The solid line in Fig. 5.8 is the solution to Eq. (5.9). Note that the width of the spectral hole is noticeably wider ($\sim$135 Hz HWHM) than seen in Fig. 3.2. Because we focused the beam with a smaller lens, we attribute this increase in width to power broadening.

I show the delay in the peak of the gaussian pulse for different pulse lengths in Fig. 5.9(a). Just as we saw in alexandrite, we note that the fractional delay is greatly reduced at small pulse widths. In Fig. 5.9(b), we show the pulse distortion (D) experienced by the pulse when it is transmitted through the ruby. Again we can see that long pulses experience little distortion, and that once the pulse width becomes very narrow, the pulse is again able to travel through the ruby undistorted.

In Fig. 5.10, I show the reference and transmitted pulse intensities to illustrate
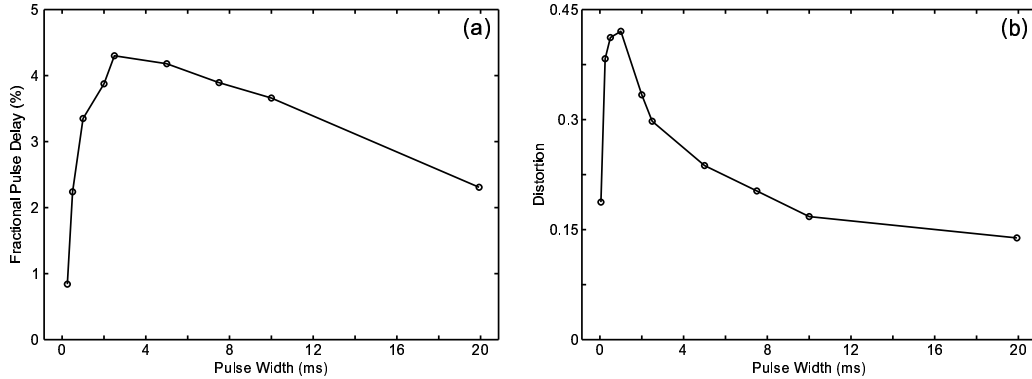
Figure 5.9: (a) The fractional delay of the peak of a gaussian pulse as a function of pulse width in ruby. (b) The distortion [as defined in Eq. (5.11)] experienced by the pulse in transmission through the ruby as a function of pulse width.

the onset of pulses distortion (particularly the tail of the pulse) as the pulse width is decreased. The plots on the left in Fig. 5.10 are from the experiment, and the ones on the right are the results of our impulse response model. As indicated in Fig. 5.9, we can see in Fig. 5.10(g) that once we reduce the pulse width to 50 μs pulse, both the pulse distortion and discernable delay disappears. When the width is too narrow, the pulse bandwidth becomes too large to interact with the spectral feature (see Fig. 5.11). Just as in the case of alexandrite, this entire narrow pulse can be thought of as a 'front' which travels at c/n through the ruby.

I also investigated the propagation of nonanalytic pulse shapes in ruby. Fig. 5.12 shows the fractional delay and distortion for pulses with an intensity profile described by Eq. (5.12). The same pattern that we have seen before emerges here again. The fractional delay disappears when the pulse becomes too narrow, and the distortion is slightly larger than it was for gaussian pulses with comparable pulse widths.
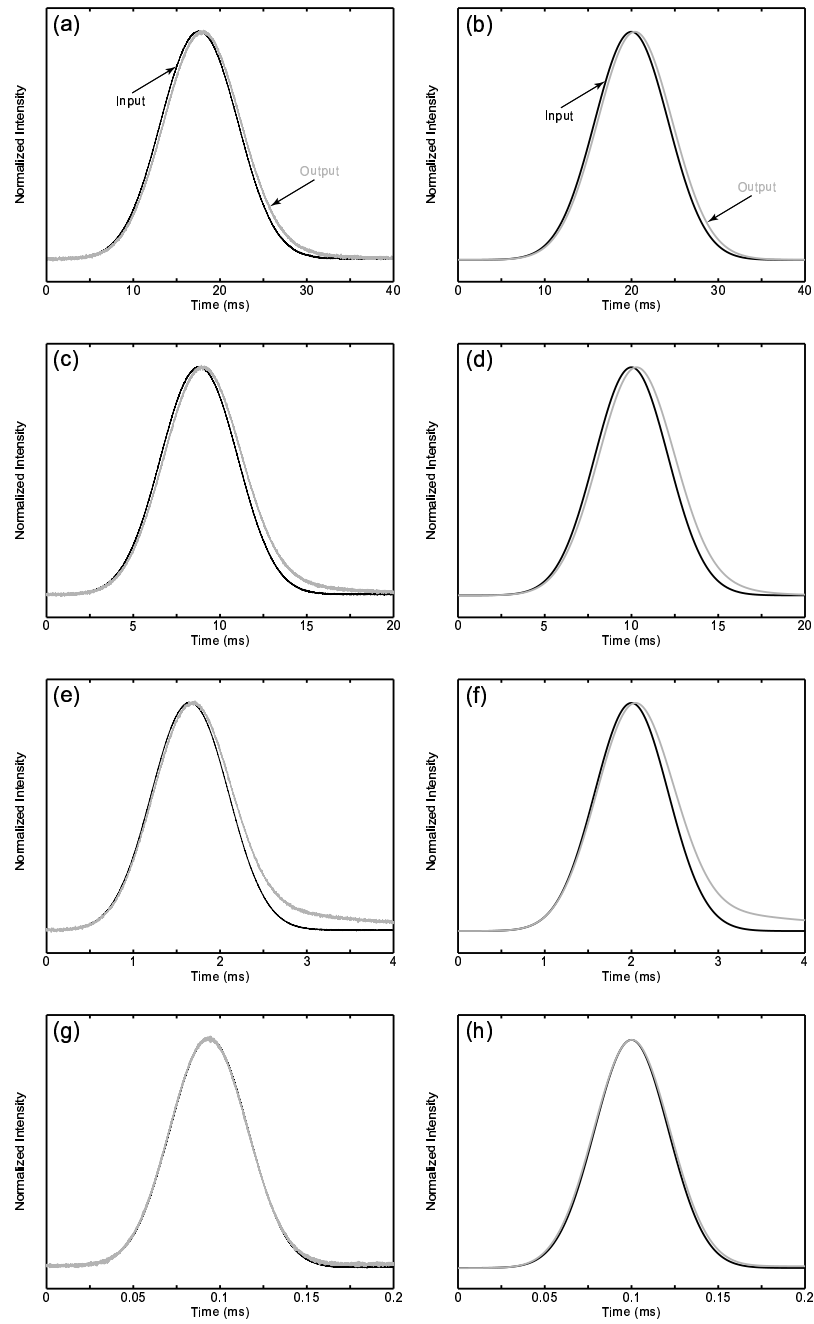
Figure 5.10: The input (black) and output (gray) intensity for gaussian pulses with different pulse widths in ruby. The left column shows the experiment and the right column shows the impulse response model. The pulse widths (FWHM) are 10 ms [(a) and (b)], 5 ms [(c) and (d)], 1 ms [(e) and (f)], and 50 μs [(g) and (h)].
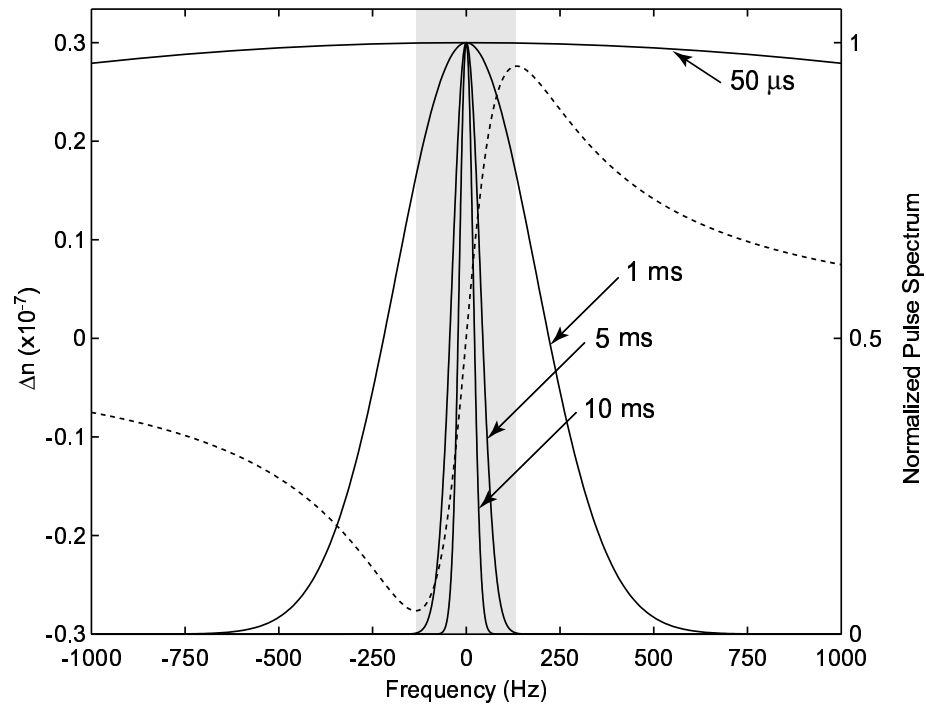
Figure 5.11: The spectra (solid lines) and the change in refractive index (Δn) induced by the strong pump beam (dashed line) for the different pulse widths shown in Fig. 5.10. The dashed line is the solution to Eq. (5.7). The gray region shows the region of large normal dispersion.
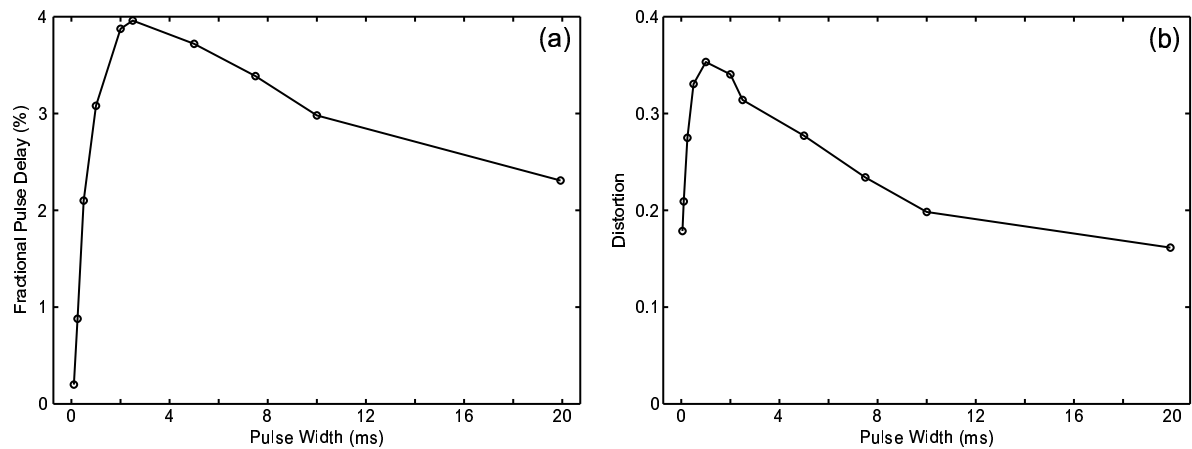
Figure 5.12: (a) The fractional delay of a nonanalytic pulse as a function of pulse width in ruby. (b) The distortion [as defined in Eq. (5.11)] experienced by the pulse in transmission through the ruby as a function of pulse width.
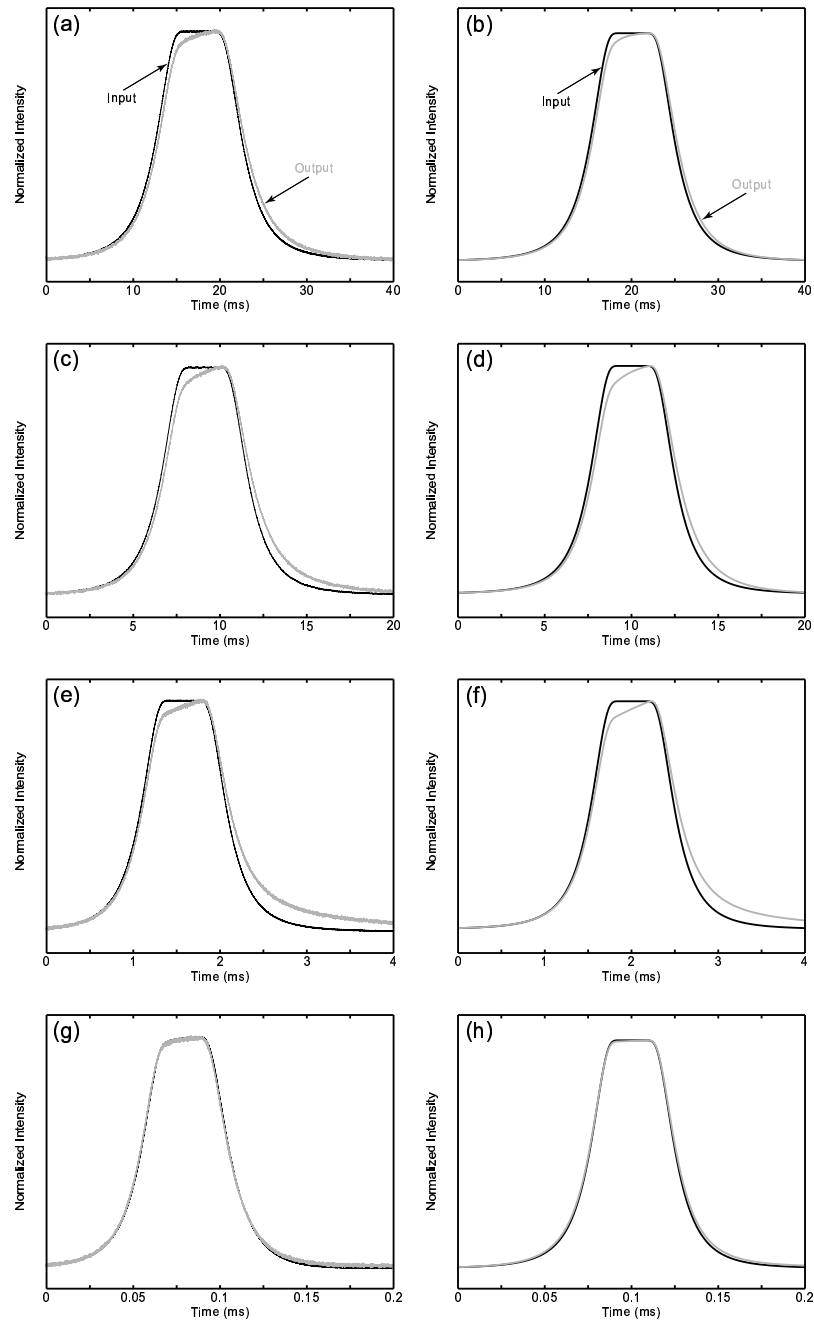
Figure 5.13: The input (black) and output (gray) intensity for nonanalytic pulses different pulse widths in ruby. The left column shows the experiment and the right column shows the results of the impulse response model. The pulse widths (FWHM) are 10 ms [(a) and (b)], 5 ms [(c) and (d)], 1 ms [(e) and (f)], and 50 μs [(g) and (h)].

We again illustrate this pattern in Fig. 5.13 where we compare our experimental results with the numerical results of our impulse response model. Note that the types of distortions that these pulses experience in ruby are quite different than the ones they experience in alexandrite. However, both regain their shape when the pulse is narrow enough.
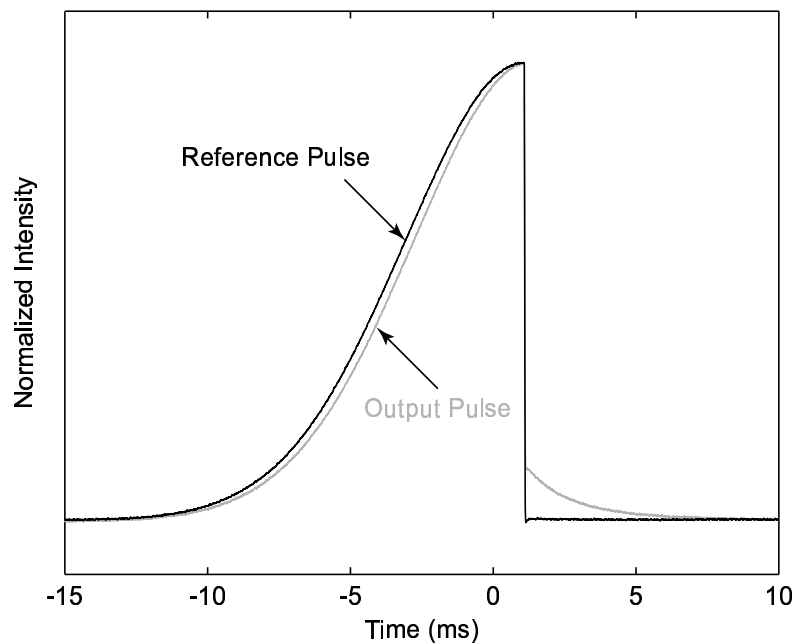
Figure 5.14: The input and normalized output intensity of a '0'-pulse in ruby. Without the sharp cutoff, the pulse would have had a width (FWHM) of 10 ms. Note that like alexandrite, the slowly varying leading edge of the pulse experiences a measurable pulse delay, but the abrupt trailing edge does not.

Finally, as with alexandrite, we sent a gaussian pulse into ruby that drops to zero at the peak. As can be seen in Fig. 5.14, we find that 'fronts' travel at luminal speeds in ruby as well. Therefore, we conclude that the information velocity in a ultra-slow light medium is also equal to c/n.

5.5   Analysis and Conclusions

We have analyzed pulse propagation in materials with both large normal and anomalous dispersion. In our first set of experiments, we investigated the evolution of gaussian pulses in alexandrite and ruby. We found that in both systems, longer pulses are substantially advanced or delayed, but that the temporal offset disappears for short pulses. Also, by sending a pulse with a clear discontinuity through both systems, we have additional evidence that information velocity is always equal to c/n. In both cases, the sharp edge travelled at luminal speeds even if the rest of the pulse was delayed or advanced.

What does this tell us about the information velocity? In Chap. 1, I quoted Brillouin who defined a signal as "... a short isolated succession of wavelets, with the system at rest before the signal arrived and also after it has passed." Such a definition would require a signal to have infinite frequency components, and leads to the prediction of the Brillouin and Sommerfeld forerunners or precursors. Brillouin assumed that it was not possible to detect precursors. As a result, he predicted that the information velocity is equal to the group velocity in a material with normal dispersion and less than c in a material with anomalous dispersion. Alternatively, if you can detect the precursor, the information velocity must be equal to c in all cases. However, a Brillouin precursor is simply a part of the signal that is too fast for the system to have time to respond. As we increased the bandwidth of our gaussian pulses, we would observe pulse distortion. We can interpret this distortion as the

interference of the precursors with the main signal. Once we further increase the pulse bandwidth, the main signal itself is too fast for the system to respond, and the entire pulse effectively becomes a precursor. Thus the information velocity is equal to c in both systems.

Also, we note that for a pulse centered on the spectral feature (which is automatically the case for these experiments), the pulse dispersion is normal for ruby and anomalous for alexandrite *regardless* of the bandwidth of the pulse. In the case of alexandrite, this is because even though an individual frequency component of the pulse may be in a region of normal dispersion, there is always a corresponding frequency component on the other side of the spectral feature which will beat with the first component. These two corresponding frequency components must be considered together, and combined, they *always* experience anomalous dispersion. The same argument can be also applied to ruby. Therefore, we can argue that the information velocity in these systems is luminal even when the pulse only sees normal or anomalous dispersion.

Finally, in this study, I have not considered the influence of noise (which must be present in any real system) on the information arrival time. What this work shows is that the information velocity is limited by c independent of the noise in the system. Once noise is taken fully into account, the information velocity becomes strictly less than c in all systems [99].

Chapter 6

Slow and Fast Light in

Erbium-Doped Fiber Amplifiers

"The light of the eyes rejoiceth the heart ..." — Proverbs 15:30

In this chapter, we extend the study of coherent population oscillations to single-mode erbium-doped silica fiber. This is a significant extension because erbium-doped fiber amplifiers (EDFAs) are a well-developed technology and the 1550 nm wavelength is prevalent in telecommunications. In addition, compared to other solid-state media, doped fibers allow for long interaction lengths, which can be desirable in producing a strong effect. Finally, since the medium acts as an absorber or an amplifier depending on the strength of the pump field, we gained the ability to tune the pulse delay continuously from positive to negative by using a separate pump laser. This work

was inspired by the work of Jarabo *et al.* [100, 101].

The energy-level structure for erbium in silica fiber at room temperature bears a strong resemblance to ruby (see Fig. 6.1). It is effectively a three-level system with a strong absorption band where population rapidly decays to a metastable level [102]. The lifetime of the metastable level is about 10 ms. However, the laser scheme that
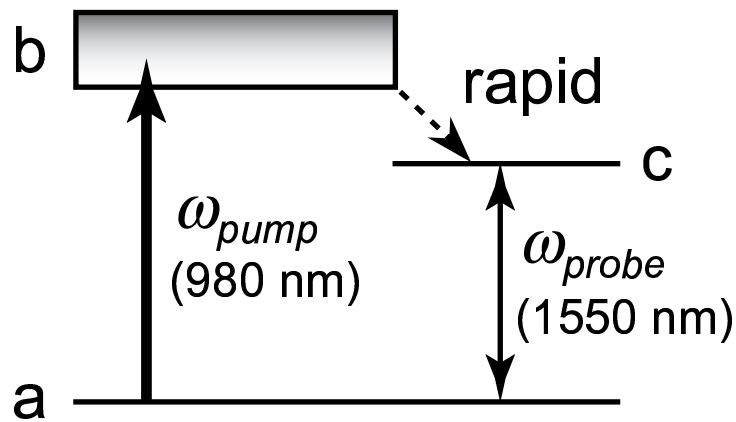
Figure 6.1: The energy levels and pumping scheme we employed to observe slow and fast light in erbium fiber.

we employed differs significantly from that of the ruby and alexandrite experiments. For those experiments, the modulated field is tuned between the ground state and the broad absorption band (levels *a* and *b*). Whereas for the experiments with erbium-doped fiber, the modulated field is tuned between the metastable level and the ground state (*a* and *c*). This arrangement allows us to add a separate pump beam (unmodulated) tuned between the ground state and the broad absorption band (*a* and *b*) that we could use to control the static population in the metastable level.

A schematic of the experimental layout is shown in Fig. 6.2. We used a counter-
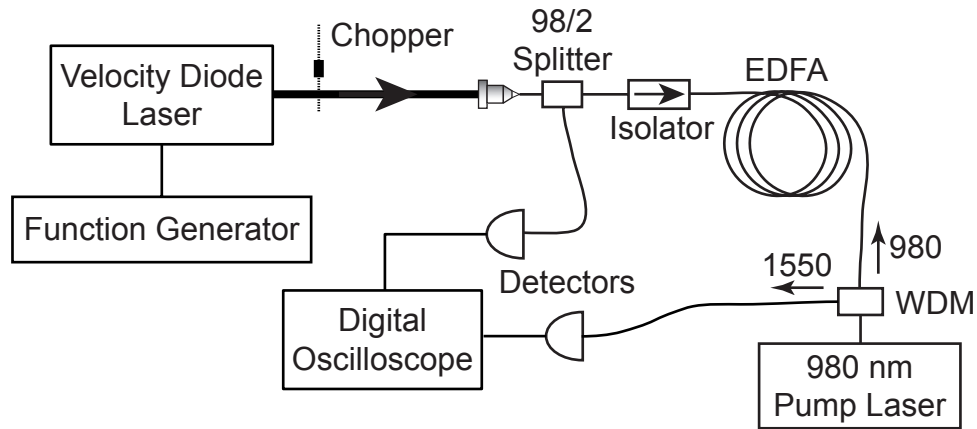
Figure 6.2: The experimental setup used to observe slow and fast light in erbium fiber.

propagating 980 nm diode laser to pump the amplifier. The modulated field, which directly drives population oscillations, comes from a second diode laser at 1550 nm. The modulations could be directly imposed on the beam by driving the laser control box from a function generator. An alternate set-up, consisting of a chopper with a single narrow slit in the wheel, was used to produce effectively gaussian pulses that had no background. Part of the light was split off before the EDFA to be detected and recorded as a reference. The rest went through the 45-meter amplifier and the delay or advancement of the signal was recorded as a function of pump power or modulation frequency on a digital oscilloscope. The recorded waveforms could then be compared on a computer and a delay or advancement could be calculated. The two detectors were made as identical as possible to eliminate false time delays.

In Fig. 6.3, we show the advancement of a modulated signal at a pump power of 12.6 and 140 mW as a function of modulation frequency. We see that it is possible
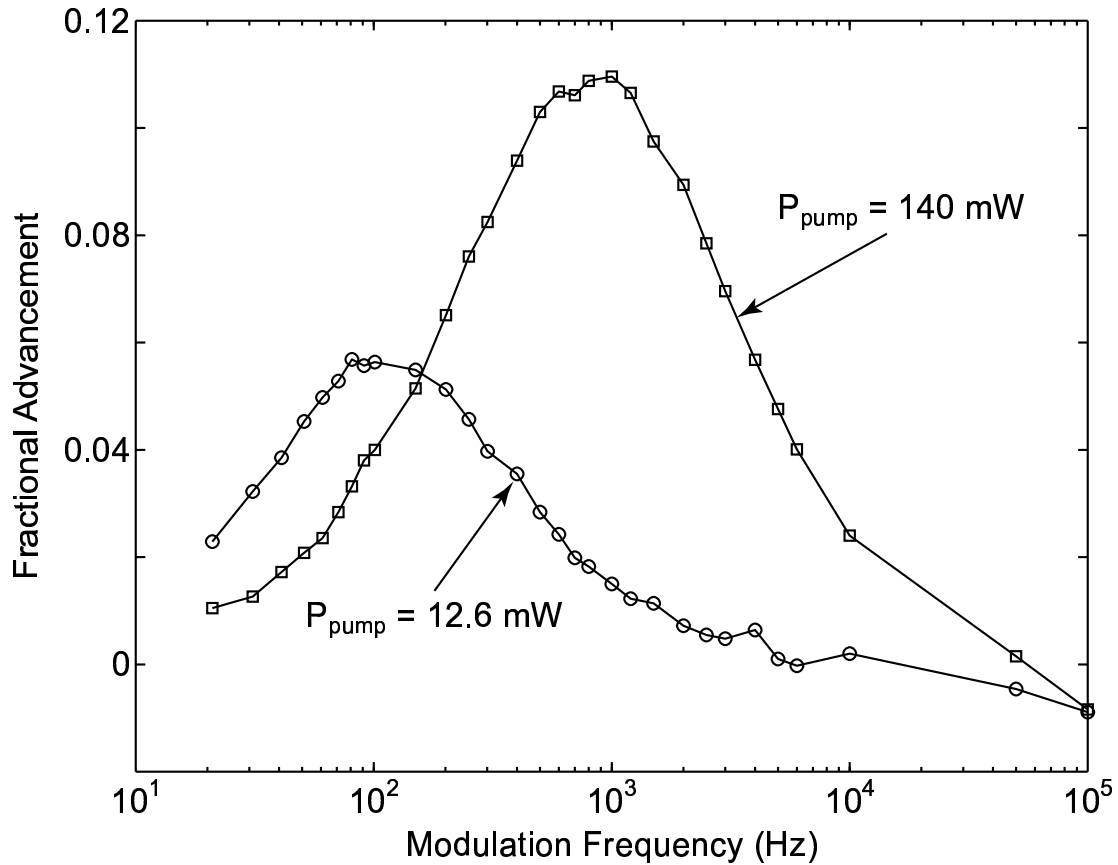
Figure 6.3: The fractional modulation advancement as function of modulation frequency for two different pump powers.

to at least double the fractional delay by increasing the pump power. In addition, we note that at higher power, the peak of the fractional delay is shifted to higher frequencies by nearly an order of magnitude. However, we found that these effects saturate so that the fractional advancement and the location of peak does not change significantly for pump powers greater than 140 mW. The delay in the modulation seen at very high frequencies originates from the time it takes for the light to pass through the amplifier (and connecting fiber) which starts to become significant with these fast signals. These results are in good qualitative agreement with the results

that other investigators have found [103, 104].

For the next set of experiments, we were able to demonstrate how pulses can transition from sub-luminal to super-luminal group velocities with increasing pump power. In Fig. 6.4, we show the delay of the peak of an 11.3 ms gaussian pulse as a function of pump power. We can see that the pulse delay becomes negative at
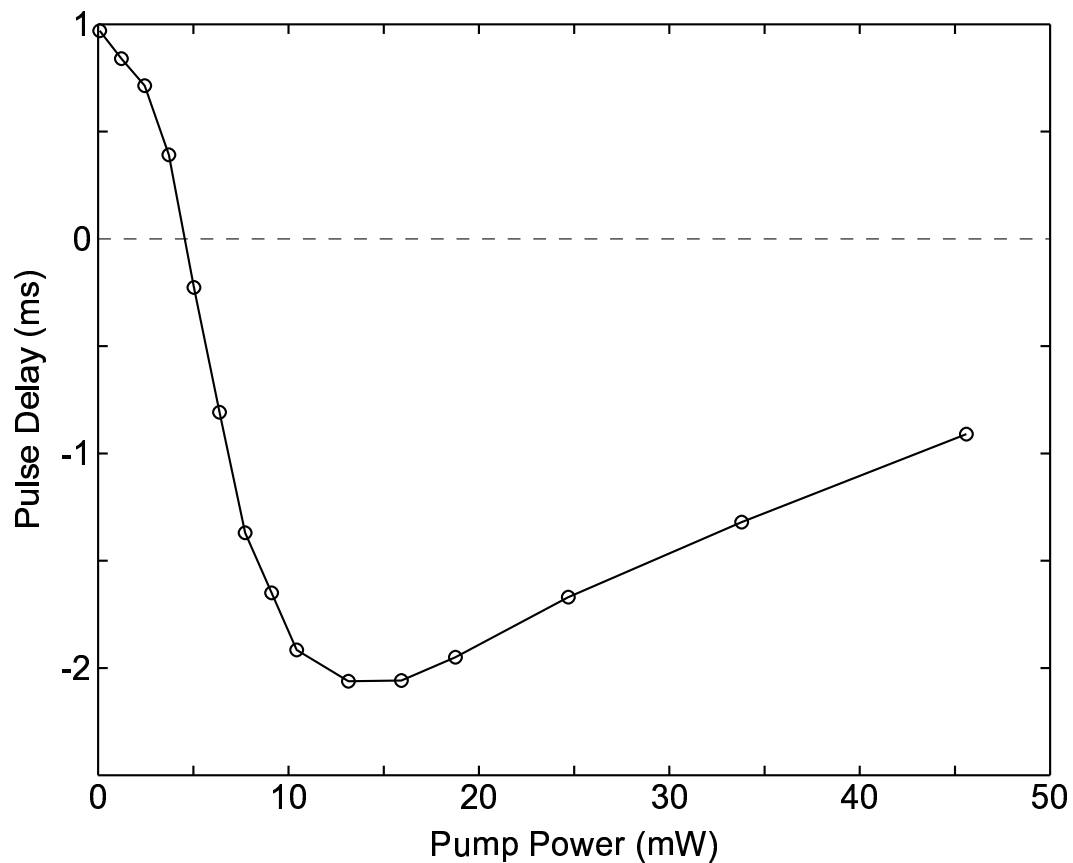
Figure 6.4: The delay of the peak of a gaussian pulse as a function of pump power. The input pulse had width (FWHM) of 11.3 ms.

pump power of about 4.5 mW, has a minimum at about 14 mW, and then increases back towards zero at higher power. This reduced effect is a result of pulse distortion (broadening) where the pulse broadens out to a width of ~18 ms.

In Fig. 6.5, we show the input and output intensity for two of the pulses from

Fig. 6.4. At a pump power of 2.45 mW [Fig. 6.5(a)], the pulse experiences a delay of

0.71 ms corresponding to a group velocity of $c/4{,}700$. By increasing the pump power to
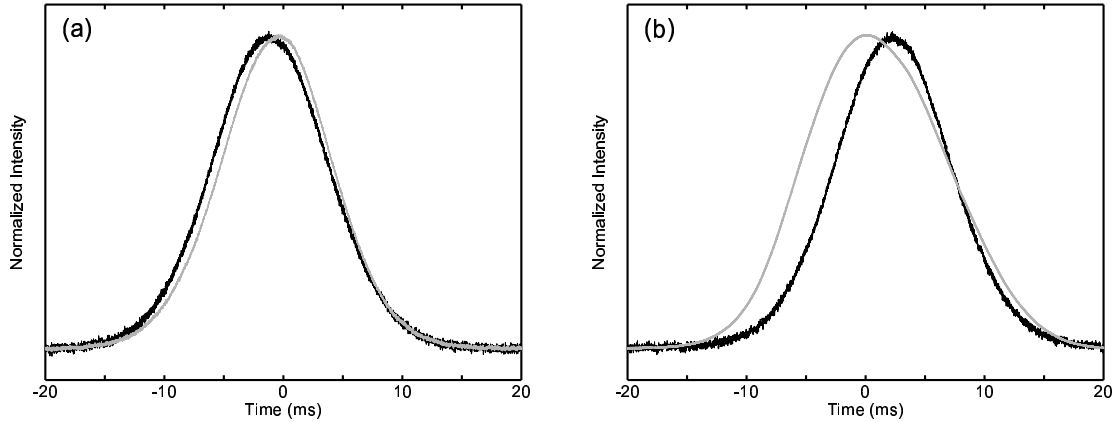
Figure 6.5:   The input and output pulse intensities for a gaussian pulse with a
pump power of (a) 2.45 mW and (b) 10.43 mW.

10.43 mW [Fig. 6.5(b)], the peak of the pulse is advanced 1.92 ms which corresponds to

a group velocity of $-c/12{,}800$. Note that this pulse has been considerably broadened.

In summary, we investigated coherent population oscillations in erbium-doped

fiber amplifiers. Although the absolute value of the group velocity was smaller in

this system than it was for ruby or alexandrite, we had a much greater control of the

group velocity than we had in those other systems. In addition, we found that we can

produce a larger fractional effect in this system as compared with ruby or alexandrite,

and we could increase the fractional advancement (and modulation frequency where

the largest advancement would occur) by increasing the pump power. However, we

found that the advancement could not be increased without limit and would saturate.

We also found that pulse distortion limits pulse advancement. While the data that I have shown in this chapter was taken with a 45-meter erbium-doped fiber, we found comparable results with a 13-meter fiber. Therefore, we conclude that these results are an important step in the development of all-optical delay lines, but much work is still needed.

Chapter 7

Group Velocity Control in an SBS

Amplifier

"... the light shall not be clear, nor dark." — Zechariah 14:6

Now we analyze a completely new technique to control the group velocity in a material. As discussed in Chap. 2, the group velocity of a pulse can be changed in a material where there is a dip in the absorption at the pulse central frequency. This dip would be equivalent for a pulse to see (unsaturated) gain at its center frequency. What we investigate in this chapter is precise group velocity control in a stimulated Brillouin scattering (SBS) amplifier.

The SBS amplifier scheme has several major advantages that the methods presented in previous chapters lack. Like the erbium-doped fiber amplifier (EDFA)

technique, the SBS technique can be done in a fiber which allows for a long inter-action region, and it works at the telecommunications wavelength (1550 nm). Also, the amount of delay in the SBS amplifier can be precisely controlled with an external pump laser. However, the pulses that an SBS amplifier can delay are much shorter, ideally on the order of the phonon decay time (10's of nanoseconds). In addition, the fractional pulse delays can be much larger than any of the other systems mentioned. Although even under the best conditions the group velocity in a SBS amplifier is only decreased by less than a factor of three, the combination of large interaction lengths and short pulses makes the effect very significant.

To analyze this system, we start with the propagation equation for a wave in an SBS amplifier. The evolution of the Stokes field (A_2) is given by [86]

$$\frac{dA_2}{dz} = \frac{-i\omega q^2 \gamma_e^2}{8\pi n_0 c \rho_0} \frac{|A_1|^2 A_2}{\Omega_B^2 - \Omega^2 + i\Omega\Gamma_B}, \tag{7.1}$$

where ω is the optical frequency of the pump, q is the phonon wavenumber, γ_e is the electrostrictive constant, n_0 is the refractive (phase) index, ρ is the material density, A_1 is the pump field, Ω_B is the Brillouin frequency, Ω is the frequecy that the Stokes field is detuned from the pump, and $\tau_p = \Gamma_B^{-1}$ is the phonon lifetime. Since $q = 2k_1 = 2n_0\omega/c$, we can write Eq. (7.1) to as

$$\frac{dA_2}{dz} = \frac{-i\omega^3 \gamma_e^2}{c^4 \rho_0} \frac{\Omega_B^2 - \Omega^2 - i\Omega\Gamma_B}{\left(\Omega_B^2 - \Omega^2\right)^2 + \Omega^2 \Gamma_B^2} I_1 A_2, \tag{7.2}$$

where $I_1 = n_0 c/(2\pi)|A_1|^2$ is now the intensity of the pump beam. If we define $A_2 \equiv a_2 + ib_2$ where a_2 and b_2 are purely real, we can separate Eq. (7.2) into real and imaginary components. We make the approximation that $(\Omega_B + \Omega)^2 \simeq 4\Omega^2 \simeq 4\Omega_B^2$ and find

$$\frac{da_2}{dz} = -\frac{g_0}{2}\frac{(\Gamma_B/2)^2}{(\Omega_B - \Omega)^2 + (\Gamma_B/2)^2}I_1 a_2, \tag{7.3}$$

and

$$\frac{db_2}{dz} = -\frac{g_0\Gamma_B}{4}\frac{(\Omega_B - \Omega)}{(\Omega_B - \Omega)^2 + (\Gamma_B/2)^2}I_1 b_2, \tag{7.4}$$

where

$$g_0 = \frac{\gamma_e^2 \omega^2}{n_0 v c^3 \rho_0 \Gamma_B} \tag{7.5}$$

is the line-center gain factor and v is the velocity of sound in the material. We see that Eq. (7.3) describes the gain of the Stokes field and Eq. (7.4) describes the phase change (and correspondingly the refractive index) of the Stokes field. If we make the assumption that the pump beam is undepleted, we can solve Eq. (7.4) to find that the change in the refractive index seen be the Stokes field as a function of frequency is

$$\Delta n(\Omega) = -\frac{I_1 \Gamma_B g_0}{4k_0}\frac{(\Omega_B - \Omega)}{(\Omega_B - \Omega)^2 + (\Gamma_B/2)^2}, \tag{7.6}$$

where k_0 is the wavenumber of the pump beam. Using the known values [86, 102] of the line-center gain factor, the Brillouin frequency, and the linewidth at 1550 nm, I plot Eq. (7.6) for different pump powers. In Fig. 7.1, we can see that when a
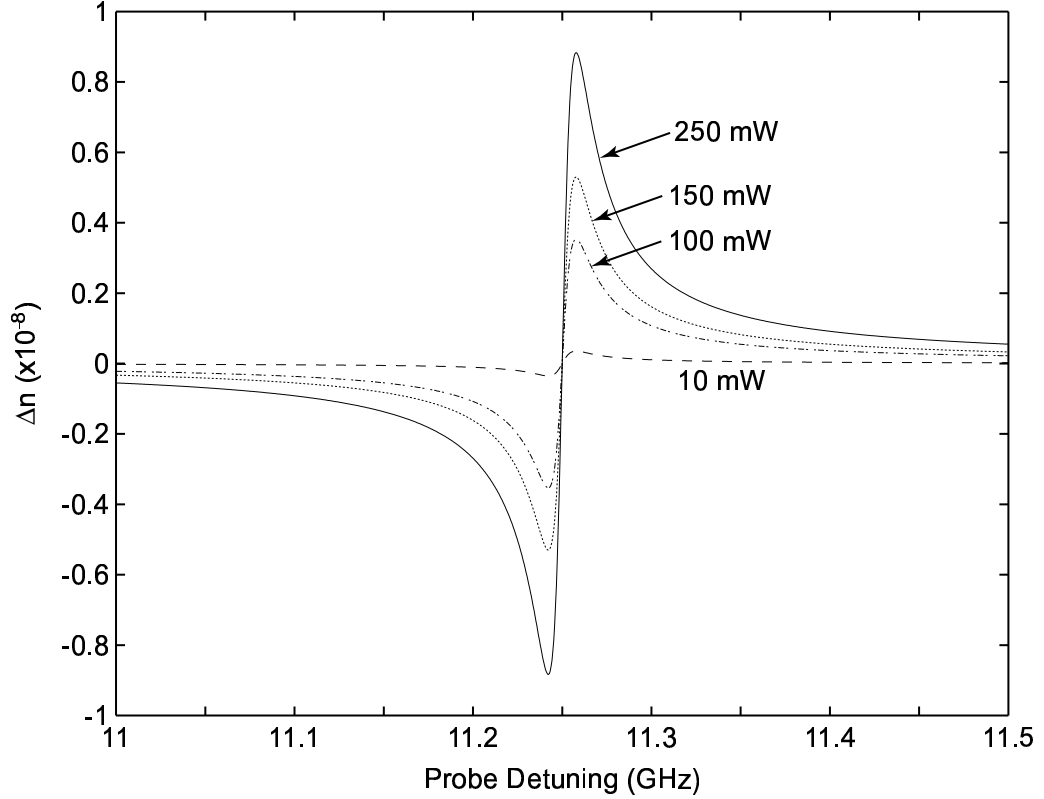
Figure 7.1: The change in the refractive index seen by the probe pulse as a function of frequency for different pump powers.

probe pulse is tuned to the peak of the SBS gain, it should experience strong (and controllable) normal dispersion.

From Eq. (7.6), we can also calculate the group index. We find that

$$
\begin{aligned}
n_g(\Omega) &= n_{g,0} + \omega \frac{dn}{d\Omega} \\
&= n_{g,0} + \frac{c I_1 \Gamma_B g_0}{4 n_0} \left\{ \frac{(\Gamma_B/2)^2 - (\Omega_B - \Omega)^2}{\left[(\Omega_B - \Omega)^2 + (\Gamma_B/2)^2 \right]^2} \right\},
\end{aligned}
\tag{7.7}
$$

where $n_{g,0}$ is the unaltered group index of the fiber at the probe wavelength. Since

the group index is maximum when $\Omega = \Omega_B$, we can find the simple expression

$$n_g^{max} = n_{g,0} + \frac{cg_0}{n_0\Gamma_B}I_1.\tag{7.8}$$

The net group delay is therefore

$$\Delta t_g^{max} = \frac{Lg_0}{n_0\Gamma_B}I_1,\tag{7.9}$$

where L is the length of the SBS amplifier. We see that as long as the pump remains undepleted, the effect is linear in pump power. In addition, the effect gets larger at longer wavelengths since Γ_B is inversely proportional to the square of the wavelength. Since we want this system to work at telecommunications wavelengths, a larger effect at longer wave lengths is advantageous. However, it does limit the bandwidth of our pulses to $\sim$16 MHz. Despite the simplicity of Eq. (7.9), we can not make the delay arbitrarily large by increasing the pump intensity. If the pump gets too large, SBS will occur within the amplifier and the pump will be depleted before it can amplify the pulse. In addition, the signal that is amplified will be very noisy. We also find, once we plug in real numbers, that $n_g^{max} \sim 3$. This may not seem like much, especially in light of the last couple of chapters where the group velocity was on the order of a million, but since the pulses are short and the interaction lengths are long, the fractional delay can be very large.

To get Eq. (7.9), I have made the assumption that the pump remains large com-

pared to the probe. Clearly if we amplify over long distances and/or the probe peak

power is relatively high, this assumption is no longer valid. To address this issue, I

numerically solved Eqs. (7.3) and (7.4), and I kept track of the energy flow out of

the pump beam into the probe pulse. The results of these calculations are shown

in Fig. 7.2. The *additional* pulse delay caused by the SBS dispersion was calculated
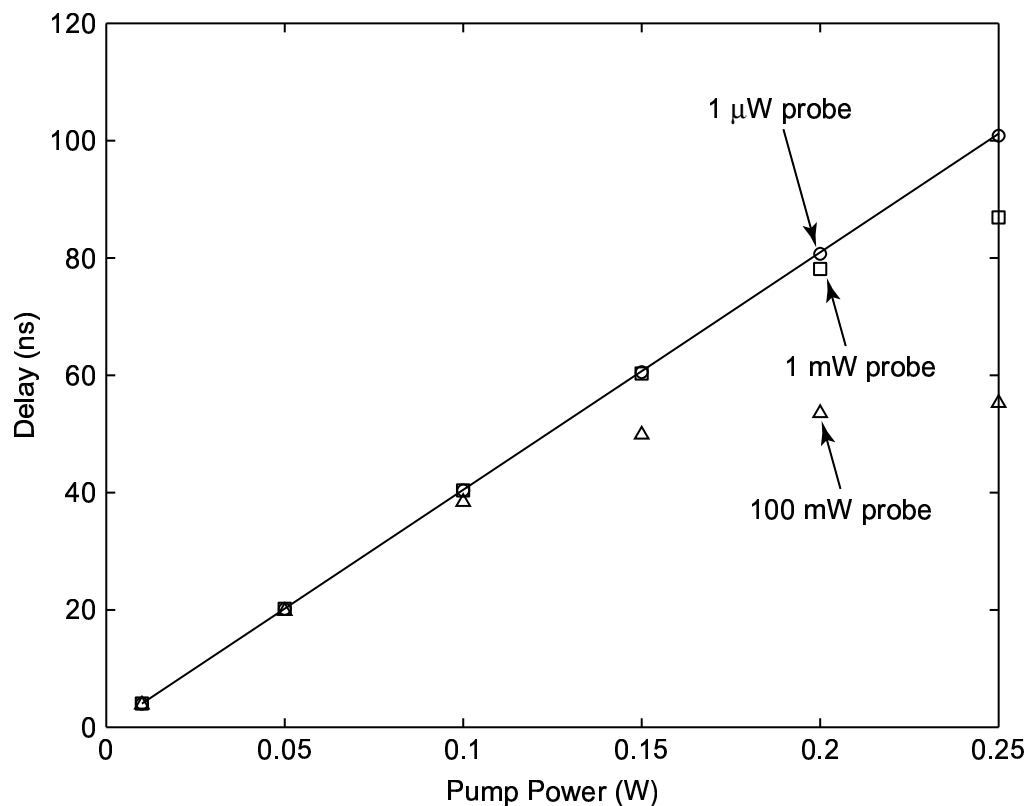
Figure 7.2: The calculated additional delay of probe pulse as a function of different pump powers over a 100 meter single-mode fiber. The solid line is the undepleted pump approximation found in Eq. (7.9). I calculate numerically the delay for a pulse with a peak power of 1 μW (circles), 1 mW (squares), and 100 mW (triangles).

over 100 meters of SMF-28 optical fiber. I found that as long as the peak power of

the optical pulse is less than 1 mW, Eq. (7.9) is a reasonably good approximation to

the group delay. Additionally, for a probe pulse width of ~50 ns, the delay can be up to two pulse widths.

Our experimental set-up is shown in Fig. 7.3. The output of a New Focus Velocity
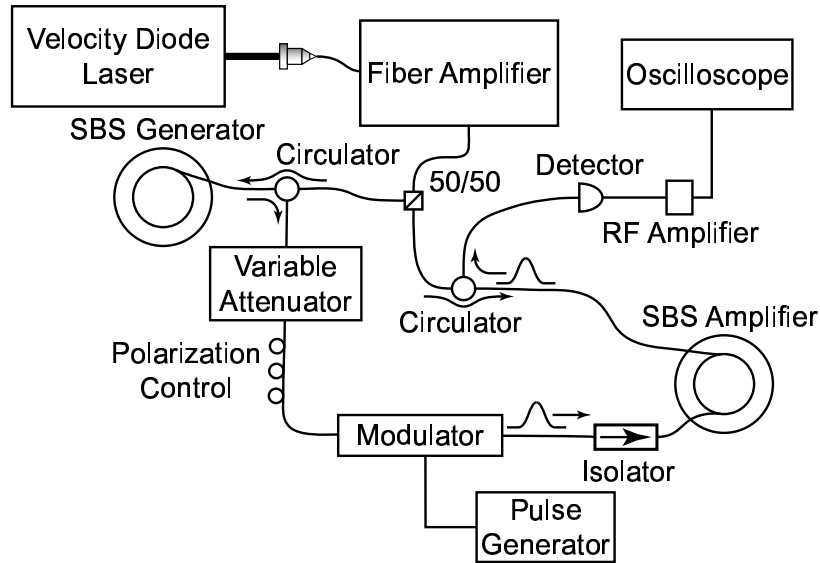
Figure 7.3: The experimental setup used to observe controllable slow light in an SBS amplifier.

diode laser tuned to 1550 nm was coupled into a fiber and sent to a erbium-doped fiber amplifier (EDFA). Although the EDFA was capable of producing over 1 Watt of optical power, we reduced the gain since we did not need that much power. To assure that the frequency of the probe pulses will be centered on the SBS gain peak, we sent part of the pump beam into a long fiber (1 km) to act as an SBS generator. The generated Stokes light was strongly attenuated in the variable attenuator (>20 dB) and then sent through an electro-optic modulator to produce nanosecond pulses. The modulator was sensitive to polarization so a fiber polarization controller was placed between the variable attenuator and the modulator. The input pulse shape was a

square, but the rise time was increased on the pulse generator to minimize ringing. We estimated the peak power of the input pulses to be less than 100 μW. These pulses travelled through a 300-meter SBS amplifier to a detector. The measured pump power before the amplifier was 120 mW. Since the pulses (even after the SBS amplifier) are weak, the output of the detector is sent through an RF amplifier before it is recorded on a digital oscilloscope. To observe a delay, the pulses were also recorded when the SBS amplifier pump wave was blocked.
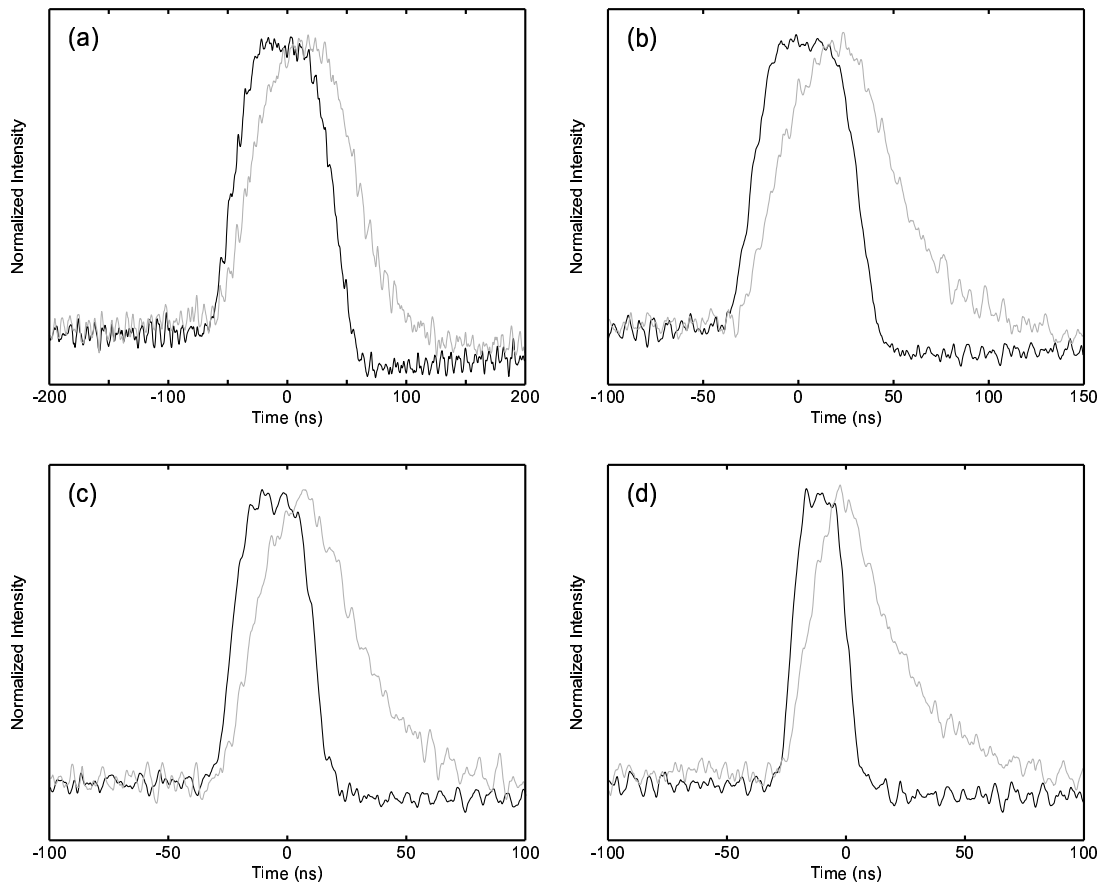
Figure 7.4: The normalized reference (black) and delayed (gray) pulse intensities for an (a) 80 ns, (b) 50 ns, (c) 30 ns, and (d) 20 ns input pulse.

In Fig. 7.4, I show the reference and delayed normalized pulse intensities for several different input pulse widths. We see that the observed delay for the 80 and 50 ns pulse (20 ns) is about a factor of six less than what we predicted from Eq. (7.9). We attribute the difference to pump depletion as a result of amplification of the input pulse background. Our modulator did not have a perfect extinction ratio, and so pump power was lost in amplifying the background. Additionally, as a result of the background depleting the pump, we found that higher pump powers would not increase the pulse delay. Nevertheless, we could still produce significantly larger fractional delays than we could in ruby, alexandrite, or erbium-doped fiber. We can also see that bandwidth of the input pulse influences the output pulse shape. Although the largest fractional delays ($\sim$50%) occur at a pulse length of 20 and 30 ns, the pulse is noticeably distorted since the pulse bandwidth is comparable to the SBS gain bandwidth.

In conclusion, we have done a proof-of-principle experiment demonstrating controllable slow light generation in an SBS amplifier. While the total delays are relatively small, the fractional delays can be very large. Similarly, the bandwidth of this system is substantially larger than any we have studied previously. In addition, the slow light medium—single-mode fused silica fiber—is even less exotic and expensive than ruby or alexandrite. Finally, we note that this method can be used to delay single photons. Therefore, we conclude that this technique could be very important in quantum communications and other optical storage applications.

Chapter 8

Spatial Vector Ring Solitons

"I form the light, and create darkness ..." — Isaiah 45:7

In this chapter, we consider a class of vector ring solitons that possess greatly improved stability. In contrast to a scalar ring soliton that carries a definite nonzero angular momentum, each component of a vector ring soliton can be made to possess equal and opposite angular momentum to produce a beam with no net angular momentum. We show that vector ring solitons that carry zero total angular momentum are more stable than scalar ring solitons by performing both analytical and numerical studies of these vector ring solitons. Using a simplified analysis, we show that zero-angular-momentum vector ring solitons are more resilient against the dominant, low-spatial frequency, azimuthal perturbations. In addition, we find that these beams possess an additional region of instability for a certain finite range of perturbation

frequencies. However, these instabilities can be suppressed by using beams that carry

high power. These analytic predictions are in good agreement with numerical results

that are also presented in this chapter.

We assume that the vector soliton is comprised of two components of the form

$E_1(r, \phi, z, t) = \psi_1(r, \phi, z)e^{i(kz-\omega t)}$+c.c. and $E_2(r, \phi, z, t) = \psi_2(r, \phi, z)e^{i(kz-\omega t)}$+c.c. We

take the equation that describes the propagation of this field as

$$-i\frac{\partial \psi_{1,2}}{\partial z} = \frac{1}{2k}\nabla_\perp^2 \psi_{1,2} + F(|\psi_1|^2 + |\psi_2|^2)\,\psi_{1,2} \tag{8.1}$$

where $\nabla_\perp^2$ is the transverse Laplacian, and $F(|\psi_1|^2 + |\psi_2|^2)$ is a function of the total

optical intensity.   For a Kerr nonlinearity, this equation reduces to the Manakov

equation by taking

$$F\left(|\psi_1|^2 + |\psi_2|^2\right) = \gamma\left(|\psi_1|^2 + |\psi_2|^2\right), \tag{8.2}$$

where the parameter γ is related to the third-order nonlinear susceptibility by $\gamma =$

$(6\pi\omega/n_0 c)\chi^{(3)}$.   For a saturable nonlinear optical medium, we model the nonlinear

response as

$$F\left(|\psi_1|^2 + |\psi_2|^2\right) = \frac{\gamma\left(|\psi_1|^2 + |\psi_2|^2\right)}{1 + \eta\left(|\psi_1|^2 + |\psi_2|^2\right)}, \tag{8.3}$$

where η is inversely proportional to the saturation intensity.

We consider a class of solutions to Eq. (8.1) having the form

$$\psi_1(r, \phi, z) \;=\; \frac{1}{\sqrt{2}} R\left(r\right) e^{i\kappa z} e^{im\phi}, \tag{8.4a}$$

$$\psi_2(r, \phi, z) \;=\; \frac{1}{\sqrt{2}} R\left(r\right) e^{i\kappa z} e^{\pm im\phi}. \tag{8.4b}$$

Here ψ_1 and ψ_2 represent the two components of the vector soliton, $R(r)$ represents their common radial dependence, κ is their common rate of nonlinear phase acquisition, and $\pm m$ two possible orbital angular momenta for the second component [105]. We will denote the cases of equal and opposite angular momenta by (m, m) and $(m, -m)$. Scalar solitons, for which (in our notation) either ψ_1 or ψ_2 vanishes, carry nonzero-angular momentum and are essentially equivalent to the (m, m) case after the symmetry rotation: $(\psi_1 + \psi_2)/\sqrt{2} \to \psi_1$, $(\psi_1 - \psi_2)/\sqrt{2} \to \psi_2$ under which Eq. (8.1) is invariant. In contrast, the total field carries zero angular momentum in the $(m, -m)$ case. By introducing the trial solution (8.4) into the wave equation [Eq. (8.1)], we find that Eq. (8.4) is in fact a solution only if the radial function $R(r)$ obeys the equation

$$R'' + \frac{1}{r}R' = \left(\frac{m^2}{r^2} + \beta^2\right) R - 2kF(R^2)R, \tag{8.5}$$

where $\beta = \sqrt{2k\kappa}$ and where R' and R'' are the first and second derivatives of R with respect to the radial coordinate r. When we apply the boundary condition for bright solitons that $R \to 0$ as $r \to \infty$, we find that, for each value of m, there is an infinite number of solutions $R(r)$. We label these solutions as $R_{nm}(r)$, where n represents

the number of radial nodes in the solution. In Fig. 8.1 we show a representation of the intensity and phase of these solutions for different values of the mode numbers n and m.
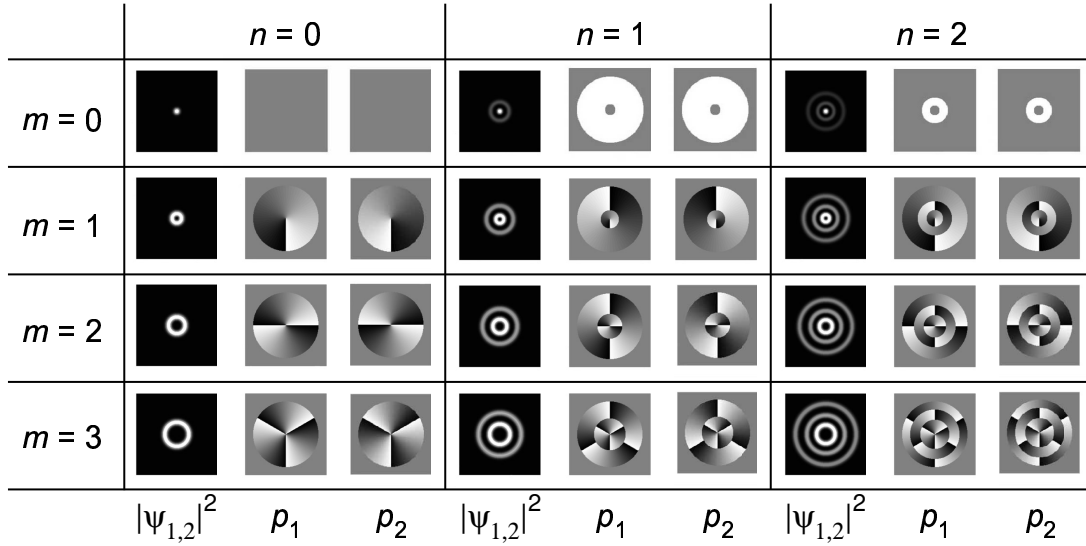
Figure 8.1: The transverse intensity $|\psi_{1,2}|^2$ and phase (p_1 and p_2) distributions for each component of the vector ring soliton, for various values of the mode numbers m and n. For the $(m, -m)$ case, the phase of $\psi_{1,2}$ is shown as $p_{1,2}$. For the (m, m) case, phase of both fields is given by p_1. The phase plots run from $-\pi$ (dark) to π (bright).

We next address the stability of these solutions and demonstrate their enhanced robustness in the $(m, -m)$ case. We consider explicitly the case $n = 0$, $m \geq 1$, although the method generalizes readily to higher-n solutions. This analysis is similar to one performed by Soto-Crespo et $al.$ and others [106]. To perform the stability

analysis, we consider perturbations of the form

$$\delta\psi_1 = \frac{1}{\sqrt{2}}a_1(r,\phi,z)R(r)e^{i\kappa z}e^{im\phi}, \tag{8.6a}$$

$$\delta\psi_2 = \frac{1}{\sqrt{2}}a_2(r,\phi,z)R(r)e^{i\kappa z}e^{\pm im\phi} \tag{8.6b}$$

We introduce this form into the linearization of Eq. (8.1) to obtain

$$-i\frac{\partial a_1}{\partial z} = \frac{1}{2k}\left(\frac{\partial^2 a_1}{\partial r^2} + \frac{1}{r}\frac{\partial a_1}{\partial r} + \frac{1}{r^2}\frac{\partial^2 a_1}{\partial \phi^2} + \frac{2R'}{R}\frac{\partial a_1}{\partial r} + \frac{2im}{r^2}\frac{\partial a_1}{\partial \phi}\right)$$
$$+\frac{1}{2}R^2 F'(R^2)(a_1 + a_1^* + a_2 + a_2^*), \tag{8.7a}$$

$$-i\frac{\partial a_2}{\partial z} = \frac{1}{2k}\left(\frac{\partial^2 a_2}{\partial r^2} + \frac{1}{r}\frac{\partial a_2}{\partial r} + \frac{1}{r^2}\frac{\partial^2 a_2}{\partial \phi^2} + \frac{2R'}{R}\frac{\partial a_2}{\partial r} \pm \frac{2im}{r^2}\frac{\partial a_2}{\partial \phi}\right)$$
$$+\frac{1}{2}R^2 F'(R^2)(a_1 + a_1^* + a_2 + a_2^*), \tag{8.7b}$$

where F' denotes the derivative of F with respect to its argument.

Now we make the change of variables $a_1 = \varepsilon_1 + i\Delta_1$ and $a_2 = \varepsilon_2 + i\Delta_2$, and introduce the definitions $\varepsilon_\pm = \varepsilon_1 \pm \varepsilon_2$, $\Delta_\pm = \Delta_1 \pm \Delta_2$ to obtain

$$-\frac{\partial \varepsilon_\pm}{\partial z} = \frac{1}{2k}\left(\frac{\partial^2 \Delta_\pm}{\partial r^2} + \frac{1}{r}\frac{\partial \Delta_\pm}{\partial r} + \frac{1}{r^2}\frac{\partial^2 \Delta_\pm}{\partial \phi^2} + \frac{2R'}{R}\frac{\partial \Delta_\pm}{\partial r} + \frac{2m}{r^2}\frac{\partial E_\pm}{\partial \phi}\right), \tag{8.8a}$$

$$\frac{\partial \Delta_\pm}{\partial z} = \frac{1}{2k}\left(\frac{\partial^2 \varepsilon_\pm}{\partial r^2} + \frac{1}{r}\frac{\partial \varepsilon_\pm}{\partial r} + \frac{1}{r^2}\frac{\partial^2 \varepsilon_\pm}{\partial \phi^2} + \frac{2R'}{R}\frac{\partial \varepsilon_\pm}{\partial r} - \frac{2m}{r^2}\frac{\partial D_\pm}{\partial \phi}\right)$$
$$+2R^2 F'(R^2)M_\pm, \tag{8.8b}$$

where $M_+ = \varepsilon_+$, $M_- = 0$. We have $E_\pm = \varepsilon_\pm$, $D_\pm = \Delta_\pm$ for the (m, m) case and $E_\pm = \varepsilon_\mp$, $D_\pm = \Delta_\mp$ for the $(m, -m)$ case. In order to check stability under

perturbations, we seek for a solution with definite angular dependence of the form,

$$\varepsilon_{\pm}(z, r, \phi) \quad = \quad \varepsilon^{\pm}(r)\cos\left(\Lambda z + \Omega\phi\right), \tag{8.9a}$$

$$\Delta_{\pm}(z, r, \phi) \quad = \quad \Delta^{\pm}(r)\sin\left(\Lambda z + \Omega\phi\right), \tag{8.9b}$$

so that the linearized equation reduces to the eigenvalue problem with eigenvalue Λ,

$$\Lambda\varepsilon^{\pm} \quad = \quad \frac{1}{2k}\left(\frac{d^2\Delta^{\pm}}{dr^2} + \frac{1}{r}\frac{d\Delta^{\pm}}{dr} - \frac{\Omega^2}{r^2}\Delta^{\pm} + \frac{2R^{'}}{R}\frac{d\Delta^{\pm}}{dr} - \frac{2m\Omega}{r^2}E^{\pm}\right), \tag{8.10a}$$

$$\Lambda\Delta^{\pm} \quad = \quad \frac{1}{2k}\left(\frac{d^2\varepsilon^{\pm}}{dr^2} + \frac{1}{r}\frac{d\varepsilon^{\pm}}{dr} - \frac{\Omega^2}{r^2}\varepsilon^{\pm} + \frac{2R^{'}}{R}\frac{d\varepsilon^{\pm}}{dr} - \frac{2m\Omega}{r^2}D^{\pm}\right)$$

$$+2R^2 F^{'}(R^2)M^{\pm}, \tag{8.10b}$$

where $E^{\pm}, D^{\pm}$, and $M^{\pm}$ are the same as before except that the cosine and the sine

factors are absent. In principle, this eigenvalue problem can be solved numerically

to determine eigenvalue Λ; if Λ possesses an imaginary part, the solution is unstable.

However, in order to develop an analytic understanding of the eigenvalue problem,

we make an approximation by assuming that stability is governed dominantly by field

fluctuations around the peak of the ring vector solitons, i.e., at $r = r_0$, $R^{'}(r_0) = 0$. We

construct Taylor expansions around $r = r_0$ for the quantities $\Delta^{\pm}(r) \simeq \Delta_0^{\pm}(r_0) + (r -$

$r_0)\Delta_1^{\pm}(r_0)$, $\epsilon^{\pm}(r) \simeq \epsilon_0^{\pm}(r_0) + (r - r_0)\epsilon_1^{\pm}(r_0)$, and $1/r \simeq 1/r_0 - (r - r_0)/r_0^2$ where $\epsilon_1^{\pm}(r_0) \equiv$

$d\epsilon^{\pm}(r)/dr|_{r_0}$ and $\Delta_1^{\pm}(r_0) \equiv d\Delta^{\pm}(r)/dr|_{r_0}$. With this expansion, we approximate the

eigenvalue equations (8.10) by keeping terms up to first order in $\delta r = r - r_0$. To begin

with, we will look at the zeroth-order part of our approximation. These assumptions are strictly valid for the case of a very thin ring, but even for a broad ring case they provide a good qualitative description of stability and agree quite well with numerical results we present later in this chapter. With these assumptions, the eigenvalue equation reduces to

$$\Lambda \varepsilon_0^\pm = -\frac{\Omega^2}{2kr_0^2}\Delta_0^\pm - \frac{m\Omega}{kr_0^2}E_0^\pm, \tag{8.11a}$$

$$\Lambda \Delta_0^\pm = -\frac{\Omega^2}{2kr_0^2}\varepsilon_0^\pm - \frac{m\Omega}{kr_0^2}D_0^\pm + 2R_0^2 F'(R_0^2)M_0^\pm, \tag{8.11b}$$

where the subscript '$_0$' signifies evaluation of quantities at $r = r_0$. Now we consider the (m,m) and the $(m,-m)$ cases separately. The eigenvalue equation for the (m,m) case can be compactly written in a matrix form

$$L\Psi = 0 \tag{8.12}$$

where the 4×4 matrix L and the vector Ψ is given by

$$\Psi^T = (\varepsilon_0^+, \Delta_0^+, \varepsilon_0^-, \Delta_0^-), \tag{8.13a}$$

$$L = \begin{pmatrix} \Lambda + 2\xi m\Omega & \xi\Omega^2 & 0 & 0 \\ -2R_0^2 F'(R_0^2) + \xi\Omega^2 & \Lambda + 2\xi m\Omega & 0 & 0 \\ 0 & 0 & \Lambda + 2\xi m\Omega & \xi\Omega^2 \\ 0 & 0 & \xi\Omega^2 & \Lambda + 2\xi m\Omega \end{pmatrix}, \tag{8.13b}$$

where $\xi = 1/2kr_0^2$. The characteristic equation,

$$\det L = \left\{ (\Lambda + 2\xi m\Omega)^2 - \xi\Omega^2 \left[\xi\Omega^2 - 2R_0^2 F'(R_0^2) \right] \right\} \left[(\Lambda + 2\xi m\Omega)^2 - (\xi\Omega^2)^2 \right] = 0,$$

(8.14)

immediately shows that complex Λ arises only if

$$\xi\Omega^2 < 2R_0^2 F'(R_0^2).$$

(8.15)

Thus, the (m, m)-ring vector soliton becomes unstable when the angular frequency of azimuthal perturbation is below the critical value $\Omega < \Omega_c = 2r_0 R_0 \sqrt{kF'(R_0^2)}$.

In the $(m, -m)$ case, the matrix L becomes

$$L = \begin{pmatrix} \Lambda & \xi\Omega^2 & 2\xi m\Omega & 0 \\ -2R_0^2 F'(R_0^2) + \xi\Omega^2 & \Lambda & 0 & 2\xi m\Omega \\ 2\xi m\Omega & 0 & \Lambda & \xi\Omega^2 \\ 0 & 2\xi m\Omega & \xi\Omega^2 & \Lambda \end{pmatrix}.$$

(8.16)

The characteristic equation now has the form

$$\det L = -\Lambda^4 + A\Lambda^2 - B = 0,$$

(8.17)

where

$$A = 8m^2\Omega^2\xi^2 + 2\Omega^4\xi^2 - 2R_0^2F'(R_0^2)\Omega^2\xi, \qquad (8.18a)$$

$$B = \xi^3\Omega^4(\Omega^2 - 4m^2)(\Omega^2\xi - 4\xi m^2 - 2R_0^2F'(R_0^2)). \qquad (8.18b)$$

In order for Λ to be real, Λ^2 has to be non-negative real. This condition can be met when A, B and the discriminant $A^2 - 4B$ are all nonnegative. Thus, the $(m, -m)$-ring vector soliton becomes stable when the frequency Ω lies in the domain satisfying the following three restrictions:

$$(i) \quad \Omega^2 \geq 2kr_0^2R_0^2F'(R_0^2) - 4m^2, \qquad (8.19a)$$

$$(ii) \quad \Omega^2 \leq 4m^2 \text{ or } \Omega^2 \geq 4m^2 + 4kr_0^2R_0^2F'(R_0^2), \qquad (8.19b)$$

$$(iii) \quad \Omega^2 \geq 2kr_0^2R_0^2F'(R_0^2) - \frac{(kr_0^2R_0^2F'(R_0^2))^2}{4m^2}. \qquad (8.19c)$$

In Fig. 8.2 we summarize the expressions from Eqs. (8.15) and (8.19) and show the regions of stability and instability for different azimuthal frequencies as a function of κ (dashed line). For the sake of argument, we have assumed the material to be a saturable nonlinear medium, but analogous diagrams can be drawn for a Kerr nonlinearity. To improve the approximations made earlier, we repeated the above analysis including terms up to first order in the Taylor expansion. When we do this L becomes a 8×8 matrix, and the corresponding regions of stability are slightly modified (solid line in Fig. 8.2).
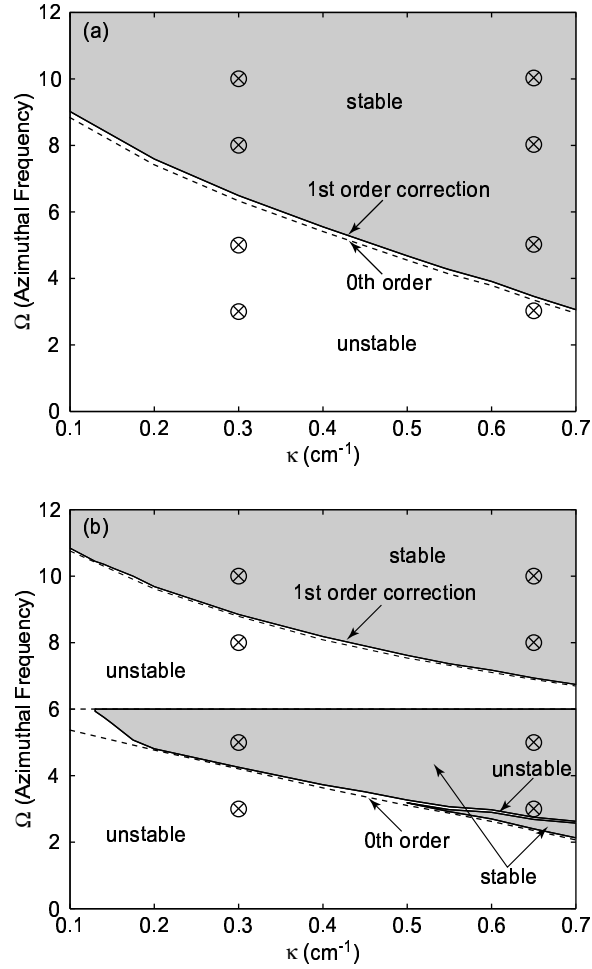
Figure 8.2: The regions of stability and instability of azimuthal perturbations to exponential growth for the R_{03} mode. The dashed line corresponds to the zeroth-order terms in the Taylor expansion and the solid line is the first-order correction. (a) The regions of stability for the (m, m) case. (b) The regions of stability for the $(m, -m)$ case. Beams with azimuthal perturbation frequencies indicated by points the graphs are shown before and after propagating through a saturable nonlinear medium in Figs. 8.3 and 8.4.

We can make several observations about Fig. 8.2. First, we note that the thin ring approximation breaks down when κ is small in the (m,-m) case. This is not surprising since the ring broadens out considerably at these lower values. Also, the large regions where the beams are nearly stable for large values of kappa are comparable to the

results of Mihalache *et al.* who report similar behavior [69, 70]. However, they only considered spinning solitons or the (m, m) case in our notation. Finally, the most significant result between the (m, m) case and the $(m, -m)$ case is that the $(m, -m)$ beam has a smaller region of instability at lower frequencies. By creating a beam that has a zero net angular momentum, we can suppress the growth of lower angular frequency perturbations that tend to dominate.

In addition, we observe that perturbations in both the lower and middle instability regions do not grow as fast in the $(m, -m)$ case as they do in the lower region of the (m, m) case. To show this, we performed numerical integrations of Eq. (8.1) using the split-step method [102] to explore the stability of the vector ring solitons in the different regions. We show in Figs. 8.3 and 8.4 the output of a vector soliton beam with small (less than 10% amplitude) complex azimuthal perturbations propagating in a saturable nonlinear medium for two different values of κ. In performing these calculations we assume the parameters $z = 50$ cm, $\gamma = 1.95 \times 10^{-6}$ cm^2/erg, $\eta = 2.49 \times 10^{-6}$ cm^3/erg, and $k = 1.28 \times 10^5$ cm^{-1}.

For the (m, m) case (Fig. 8.3) we can clearly see the beam breaking up and the individual filaments diverging from one another when the perturbation spacial frequency is $\Omega = 3$ and 5 for $\kappa = 0.3$ cm^{-1}. Beam rotation as a result of a net angular momentum can also be seen. For $\kappa = 0.65$ cm^{-1}, the beam has improved stability at these frequencies as both Fig. 8.2(a) and Ref. [69] suggests. In contrast, for the value of $\kappa = 0.3$ cm^{-1}, Fig. 8.4 shows that the perturbations to the $(m, -m)$ beam grow
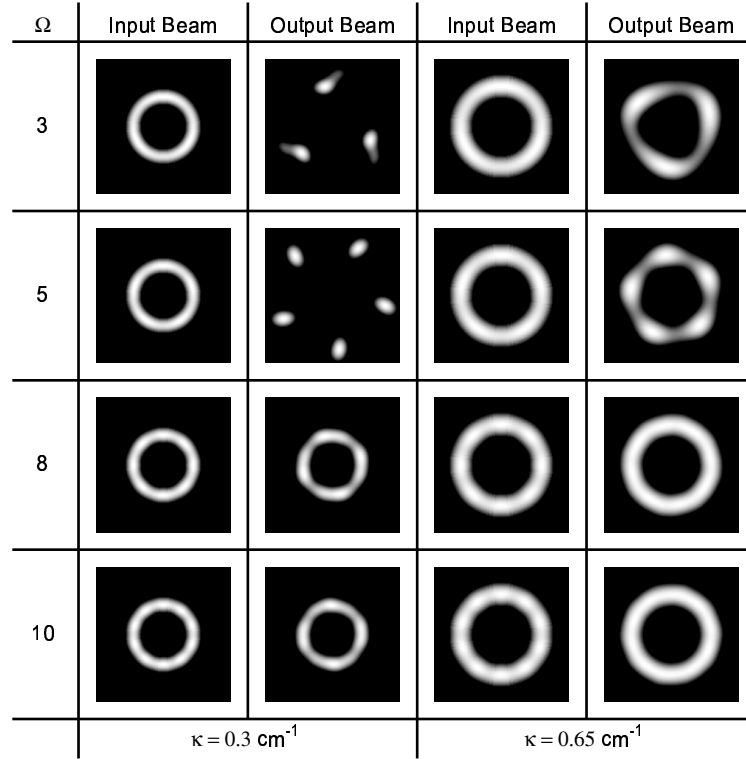
Figure 8.3: The input and output beams with four different azimuthal frequency perturbations for the (m, m) case vector soliton ($m = 3$).

at frequencies $\Omega = 3$ and $\Omega = 8$ on either side of a region of stability at $\Omega = 5$. This region of stability is predicted by our analytical theory shown in Fig. 8.2(b). When we increase the value of κ to 0.65 cm^{-1}, we see that the beam becomes essentially stable over all of these frequencies.

In conclusion, we have analyzed a class of vector ring solitons that possesses enhanced stability characteristics. These solitons have zero net angular momentum, and consequently they possess a greater degree of stability than do standard ring solitons. To show this we have conducted a simple analytical analysis of the system's eigenvalues to find the frequency regions where the rings are unstable, and have shown
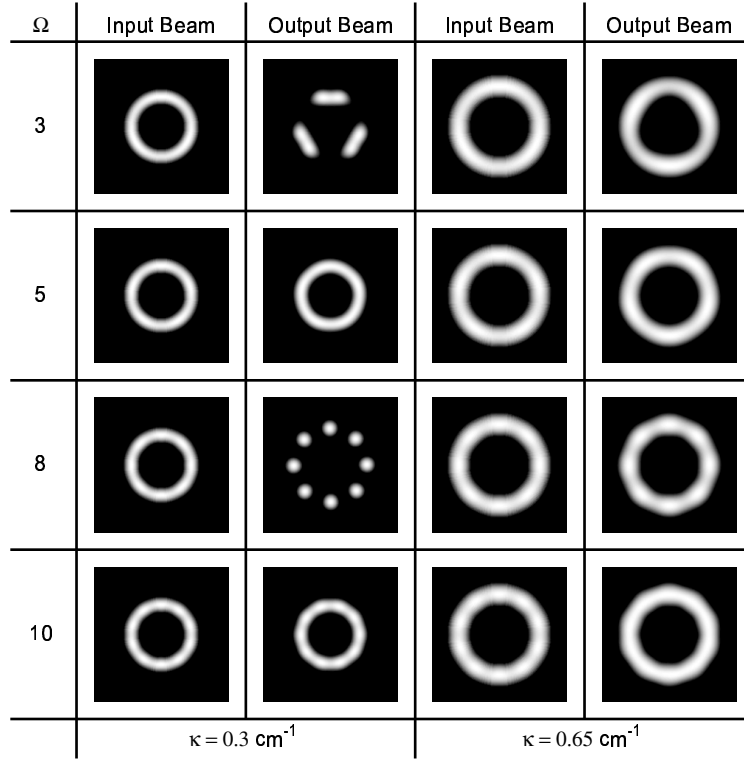
Figure 8.4: The input and output beams with the same azimuthal frequency perturbations for the $(m, -m)$ case vector soliton $(m = 3)$.

through numerical simulations that these regions exist. Therefore, the simplifying assumption that the rings are thin which we made while performing the analytical analysis is a good way to predict qualitatively the regions of stability for vector ring solitons. In particular, we have found that low frequency azimuthal perturbations of the soliton amplitude are suppressed. These results suggest that vector ring solitons with zero net angular momentum may have important applications in high-power laser systems. We also believe these vector solitons can be experimentally observed in a variety of material systems.

Chapter 9

Breakup of Ring Beams in Sodium

Vapor

"Thou hast prepared the light ..." — Psalm 74:16

In this next set of experiments, we experimentally investigate the stability of beams with orbital angular momentum in a material with a saturable nonlinearity. In contrast to the last chapter, we only consider single component beams rather than vector solitons. Specifically, we used a pulsed dye laser and observed the filamentation of solitons with orbital angular momentum values $m = 1$, 2, and 3 in a hot, dense sodium vapor. As predicted by Firth and Skryabin [51], we observed that these beams would break up into two, four, and six filaments, respectively. We compare this result with numerical beam propagation simulations that include an accurate model of the

fully saturable nonlinearity in an inhomogeneous two-level system, and show that this model gives excellent agreement with our experimental results. We also observed that these beams show some improved stability at higher powers.
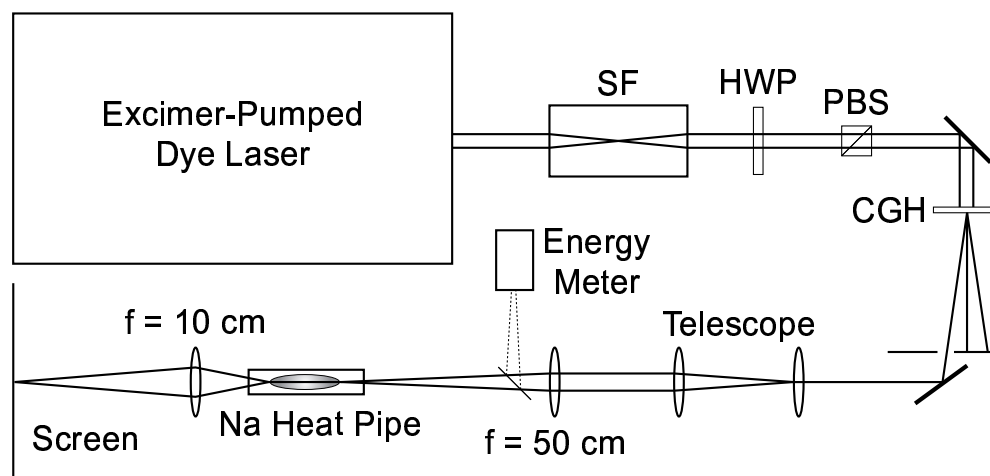
Figure 9.1: The experimental setup used to observe filamentation of ring solitons in sodium vapor.

Our experimental setup is shown in Fig. 9.1. The output of an excimer-pumped dye laser was sent through a spatial filter (SF) to produce a circular TM_{00} beam and was throttled with a half-wave plate (HWP) and polarizing beam-splitter (PBS). The pulses had a temporal width (FWHM) of about 15 ns, and were tuned from 40.6 to 46.7 GHz to the blue side of the D_2 resonance line of sodium. We sent the beam through a bleached computer-generated hologram (CGH) that would produce diffraction orders that are Laguerre-Gauss modes [107–109]. Since the input beam was circular, the generated modes are also circular. The general expression for the

field distribution for these modes at the beam waist is given by

$$
A_{m,p}(r, \phi) = A_0 \sqrt{\frac{2p!}{\pi w_0^2 (p + |m|)!}} \left(\frac{\sqrt{2}r}{w_0} \right)^{|m|}
$$
$$
\times L_p^m \left(\frac{2r^2}{w_0^2} \right) e^{-r^2/w_0^2} e^{-im\phi}, \tag{9.1}
$$

where w_0 is the characteristic beam width, and $L_p^m(x)$ is the generalized Laguerre

polynomial. The parameters p and m are the radial mode index and the topological

charge, respectively. In general, a beam in a given diffraction order would contain

a superposition of several radial modes. However, for our holograms, modes with a

radial mode index $p > 0$ were observed to be weak and assumed insignificant to beam

propagation dynamics. The conversion efficiency into the first diffraction order was

about 5%. One of the diffracted beams was enlarged in a telescope and focused to a

50 μm beam diameter inside the sodium cloud within a heat pipe. A typical value for

the number density of the sodium was 8×10^{14} cm^{-3} (depending on cell temperature),

and the region of this density was 5 cm long. We added 13 mbar of helium to the heat

pipe to act as a buffer gas. Before entering the cell, part of the beam was reflected

off a glass slide to monitor the pulse energy. The beam exiting the vapor was imaged

onto a screen several meters away where it could be photographed.

Despite the large number of earlier numerical studies of the stability of ring soli-

tons, none of these studies is directly comparable to our system because our input

beams are circular Laguerre-Gauss beams (not exact solutions) and our medium is

fully saturable (not cubic-quintic). Therefore, we model the behavior of the atomic vapor in the following manner. Since we were tuned relatively far from resonance ($\Delta > 40$ GHz), we can ignore the hyperfine energy levels and model the sodium vapor as a two-level atom. The density matrix equations of motion for a two-level atom are [86]

$$\dot{\rho}_{ba} = -\left(i\omega_{ba} + \frac{1}{T_2}\right)\rho_{ba} + \frac{i}{\hbar}V_{ba}W, \qquad (9.2a)$$

$$\dot{W} = -\frac{W - W^{(eq)}}{T_1} - \frac{2i}{\hbar}\left(V_{ba}\rho_{ab} - V_{ab}\rho_{ba}\right), \qquad (9.2b)$$

where W is the population inversion, $\hbar\omega_{ba}$ is the energy separation between level a (ground) and b (excited), T_1 is the ground state recovery time, T_2 is the dipole moment dephasing time, and $W^{(eq)}$ is the population inversion of the material in thermal equilibrium. The interaction Hamiltonian in the rotating-wave approximation is given by $V_{ba} = -\mu_{ba}E(t)e^{-i\omega t}$. To calculate the susceptibility from these equations, it is appropriate to make a steady state approximation [86, 110]. With this assumption, we can find an expression for the susceptibility

$$\chi = -\frac{\alpha_0(0)c}{4\pi\omega_{ba}}\frac{\Delta T_2 - i}{1 + \Delta^2 T_2^2 + |E|^2/|E_s^0|^2}, \qquad (9.3)$$

where N is the number density, $\alpha_0(0)$ is the unsaturated resonant absorption coefficient, $\Delta/2\pi$ is the frequency detuning, and E_s^0 is the resonant saturation field strength related to the saturation intensity as $I_s = c/(2\pi)|E_s^0|^2 = N\hbar\omega_{ba}/(2\alpha_0(0)T_1)$.

The unsaturated absorption coefficient is $\alpha_0(0) = 4\pi\omega_{ba}N|\mu_{ba}|^2 T_2/(\hbar c)$, and the susceptibility is related to the refractive index as $n = \sqrt{1 + 4\pi\chi} \simeq 1 + 2\pi\chi$. The phase index ($n_0$) and the absorption ($\alpha$) can be found by taking the real and imaginary components of the refractive index given as

$$n_0 = 1 - \frac{\alpha_0(0)c}{2\omega_{ba}}\frac{\Delta T_2}{1 + \Delta^2 T_2^2 + |E|^2/|E_s^0|^2}, \tag{9.4a}$$

$$\alpha = \alpha_0(0)\frac{1}{1 + \Delta^2 T_2^2 + |E|^2/|E_s^0|^2}. \tag{9.4b}$$

The expressions for the phase index and absorption for a homogeneously broadened two-level atom given in Eqs. (9.4) can be extended to an inhomogeneously (Doppler) broadened two-level system [111]. In such a system, the refractive index as a function of laser wavelength (λ) and intensity (I) is given by [112]

$$n_0(\lambda, I) = 1 - \frac{\sqrt{\ln 2}\lambda^3 N}{16\pi^{5/2}T_1\Delta\nu_D}\mathrm{Im}[w(\xi + i\eta)], \tag{9.5}$$

where N is the number density, $\Delta\nu_D$ is the Doppler linewidth, $\xi = 2\sqrt{\ln 2}(\nu - \nu_{ba})/\Delta\nu_D$ is the normalized detuning frequency, $\eta = \sqrt{\ln 2}/(\pi T_1\Delta\nu_D)\sqrt{1 + I/I_s}$ is power broadened hole size, and $w(z)$ is the complex error function. The absorption can also be found as

$$\alpha(\lambda, I) = -\frac{\eta\lambda^2 N}{8\sqrt{\pi}\,(1 + I/I_s)}\mathrm{Re}\,[w(\xi + i\eta)]. \tag{9.6}$$

It can be shown that by taking the asymptotic form for large z of the complex error function $w(z) \approx i/\sqrt{\pi}z$, Eqs. (9.5) and (9.6) reduce to Eqs. (9.4) [111].

To model our experimental results, we use the propagation equation

$$
\begin{aligned}
\frac{\partial A(x,y,z)}{\partial z} &= \frac{i}{2k}\nabla_\perp^2 A(x,y,z) \\
&+ (-\alpha + ik\Delta n)A(x,y,z),
\end{aligned}
\tag{9.7}
$$

where k is the wavenumber, Δn is the change in refractive index defined as $\Delta n = n_0(\lambda, I) - n_0(\lambda, 0)$, and $A(x,y,z)$ is the complex amplitude of the electric field. We solved Eq. (9.7) using a standard split-step fast Fourier transform (FFT) routine with the input beam profile described in Eq. (9.1). The parameters for $\alpha(x,y)$ and $n(x,y)$ were found at each step from the measured values from the experiment using Eqs. (9.5) and (9.6). In addition, a small amount of random amplitude noise was added to the input beam [113].

Our results for an $A_{1,0}$ beam are shown in Fig. 9.2. The laser was tuned 40.6 GHz to the blue side of resonance. Because the nonlinearity is large, even at a relatively low input energy (76 nJ), we see that the beam broke up into two filaments [Fig. 9.2(a)]. For all our results, we found that the patterns generated are quite repeatable provided that the beam quality is good. As mentioned above, we put no intentional perturbation on the beam, and made it as circular as possible. The patterns did not appear to be affected by the orientation of the hologram. Since they did not change from shot to shot, we conclude that the patterns were seeded

Figure 9.2: The experimental output (a) for an $m = 1$ beam with a pulse energy of 76 nJ breaking into two filaments at a wavelength of 588.950 nm, and (b) tuned far from resonance. In (c) and (d) we show the equivalent results from our computer simulations with parameters corresponding to our experiment and a random 1.5% amplitude noise added to the input beam.

by imperfections in our system (e.g. dust on lenses and mirrors). We observed these beams breaking up into two spots over a range of pulse energies from 65 to 710 nJ. We show in Fig. 9.2(b) the same beam tuned far from resonance (nonlinearity off). Fig. 9.2(c) and 9.2(d) show the output beam from our numerical simulations with and without the nonlinearity ($\Delta n = 0$). A random 1.5% amplitude noise has been added to the input beam in these numerical simulations.

As expected, the $m = 2$ beam was found to break up into four spots as shown in Fig. 9.3(a). For this experiment, the laser was tuned 46.7 GHz to the blue side of the D_2 resonance line, and the pulse energy was 234 nJ. The $m = 2$ beam was seen to break into four spots over a pulse energy range of 200 nJ to 1.3 μJ. We also
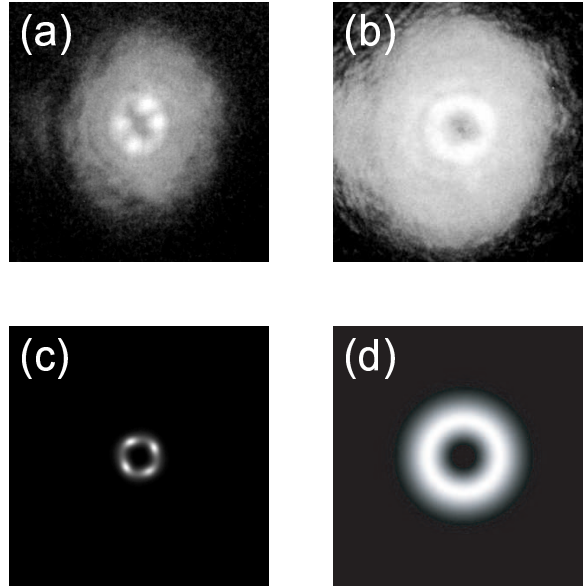
Figure 9.3: The experimental output (a) for an $m = 2$ beam with a pulse energy of 234 nJ breaking into four filaments at a wavelength of 588.943 nm, and (b) tuned far from resonance. In (c) and (d) we show the equivalent results from our computer simulations.

observed that at higher power, the $m = 2$ beam could break up into five or more spots. It can be seen in Fig. 9.3(b) that the input beam created by the computer-generated hologram was not a perfect $A_{2,0}$ beam. It had several extra rings around it indicating that it contained higher radial modes. These higher modes do not appear to be stable and appear as noise around the center $A_{2,0}$ beam in Fig. 9.3(a). Again we see in Fig. 9.3(c) and 9.3(d) that the numerical simulations are in excellent agreement with the experiment. As we did in modelling the $m = 1$ case, we added 1.5% random amplitude noise at each point on the input beam to cause the beam to break up.

In Fig. 9.4, we show the $m = 3$ beam breaking up into six spots. The observed range of six spot filamentation was 350 nJ to 2.5 μJ. The input pulse energy in
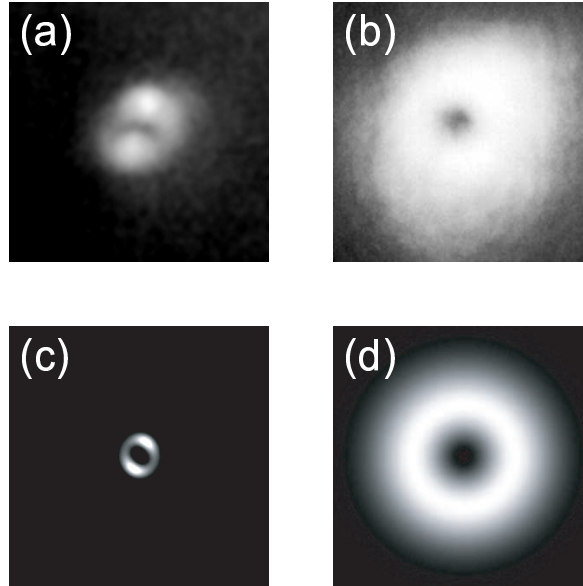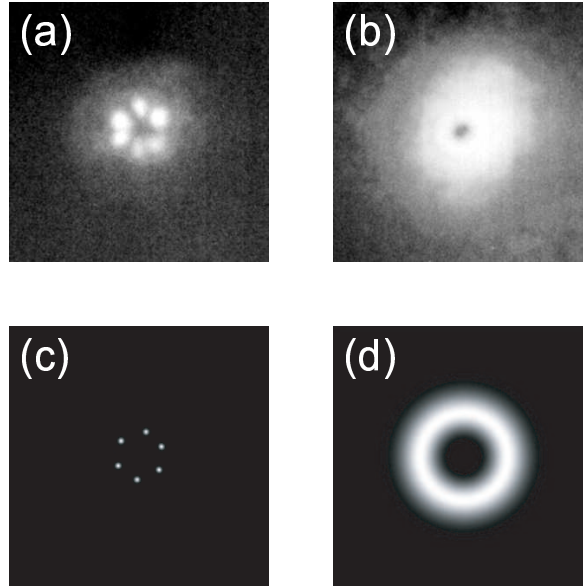
Figure 9.4: The experimental output (a) for an $m = 3$ beam with a pulse energy of 359 nJ breaking into six filaments at a wavelength of 588.943 nm, and (b) tuned far from resonance. In (c) and (d) we show the equivalent results from our simulations.

Fig. 9.4(a) was 359 nJ, and the laser detuning was again 46.7 GHz. As before, we did not add any intentional perturbation to the beam. While aligning the system, we occasionally saw the beam break up into five or seven spots caused by the seeding of these azimuthal frequencies due to poor beam quality. Poor beam quality can be caused by either misalignment of optics or light scattering off dust on optical surfaces. As we saw in the $m = 2$ beam, the $A_{3,0}$ beam from the computer-generated hologram was not perfect and had some higher-order radial modes. For the numerical simulations in Fig. 9.4(c) and (d), we added 1.0% random amplitude noise at each point.

We also experimentally observed the propagation of these beams at higher power.
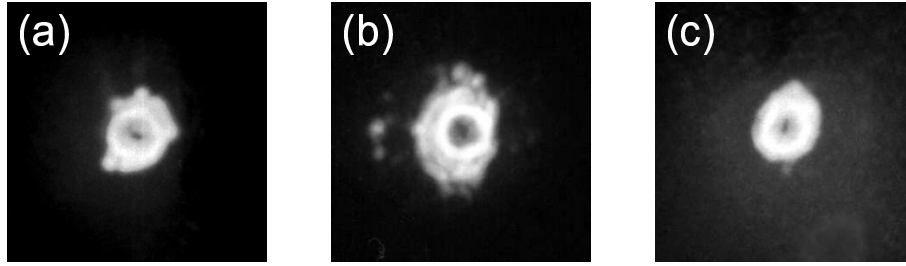
Figure 9.5: The beam profile at the output of the sodium cell at higher powers than those used in Figs. 9.2-9.4. The tendency of the beam to break into filaments is largely suppressed. (a) $m = 1$ at 9.1 μJ, (b) $m = 2$ at 24.1 μJ, (c) $m = 3$ at 6.63 μJ.

We found that when we increased the power of the beams that they would no longer break up (Fig. 9.5). The noise seen around the beams in Fig. 9.5 are the filamentation of the higher-order radial modes. We believe that the observed stability of the $A_{m,0}$ beams is caused by the beam almost completely saturating the nonlinearity, and thereby suppressing the filamentation.

While we made every effort to have perfectly circular input beams, we found that even a small amount of beam ellipticity caused the beam to break into two filaments. Tikhonenko *et al.* [79] previously observed that an elliptical $m = 2$ beam will break into two spots. However, as expected theoretically [51], we found that an $m = 3$ beam is less susceptible than an $m = 2$ beam to this type of instability.

In conclusion, we have experimentally observed that ring beams in a fully saturable nonlinear material that have orbital angular momentum m tend to break up into $2m$ nonrotating spots. Our observation of rings occasionally breaking up into something besides $2m$ beams is consistent with the predictions of Firth and Skryabin [51] since they show that perturbations with the different azimuthal frequencies will grow if

seeded, but just not as fast. We compare our experimental results with the propagation of randomly perturbed Laguerre-Gauss beams propagating in a two-level inhomogeneously broadened system, and show that it has excellent agreement with our observations. We have also observed that the beams become considerably more stable at high laser powers, which could prove important for various applications.

Chapter 10

Summary and Conclusions

"Then I saw that wisdom excelleth folly, as far as light excelleth darkness." — Ecclesiastes 2:13

In this thesis, we first described the concept of coherent population oscillations—the primary physical mechanism we used to generate large dispersion. We show that when the beat frequency between the pump and probe beams is slow enough, it will cause the population in a two-level atom to oscillate. This time-varying population will cause energy to be scattered out of the pump beam and into the probe. As a result, the probe will see less absorption over a narrow frequency range. Correspondingly, the group velocity for the probe can be very large within the same frequency range. From our investigations, it is clear that coherent population oscillations are possible in a wide variety of systems.

We described our experimental demonstration of ultra-slow light propagation in

ruby using coherent population oscillations. We observed a group velocity as low as 58 m/s which is a comparable group velocity to what is observed using much more difficult EIT techniques. Our results included the observation of a delay of both amplitude modulations and pulses. Therefore, our method is validated as an important new way to generate ultra-slow group velocities.

We further extended the investigation of coherent population oscillations to a different material. In alexandrite, we show how it is possible to observe both ultra-slow and superluminal group velocities. Since alexandrite in an inverse saturable absorber at certain wavelengths, the sign of the group velocity is changed. In addition, alexandrite has a slightly more complicated structure than ruby in that the chromium ions can occupy two different types of lattice sites within the crystal. These two types of sites are known as mirror sites (having mirror symmetry) and inversion sites (having inversion symmetry). Due to the energy level structure at each site, ions at mirror sites experience inverse-saturable absorption (fast light), whereas ions at inversion sites experience saturable absorption (slow light). The competing effects from ions at either site can be easily distinguished because they have markedly different population relaxation times.

I made a detailed investigation of the information velocity in ruby and alexandrite. I concluded that the information velocity is always equal to c even if the group velocity is ultra-slow or superluminal. I come to this conclusion by showing that it is possible to easily observe what are effectively Brillouin precursors in these type of systems. In

addition, we show that points that are non-analytic (corresponding to high-frequency components) travel at c/n regardless if group velocity in the material is ultra-slow or superluminal. These results are analogous to the resolution of apparent superluminal barrier tunnelling found by Winful [38, 39].

We considered a third material, erbium-doped optical fiber, where coherent populations oscillation can be important. We were able to observe both slow and fast light in an EDFA. This material has three distinct advantages over ruby or alexandrite. First, the entire system can be fiber-based. In addition, the wavelength where the delay or advancement occurs is at 1550 nm or the standard wavelength for telecommunications. Finally, the system can be modified to include a separate pump laser that allows us to tune the delay from slow (low pump power) to fast (high pump power).

While the group velocities that we observed in ruby, alexandrite, and erbium-doped fiber using coherent population oscillations are very impressive, the bandwidth of those systems is very limited. As a result, we were motivated to investigate a totally new way of controlling the group velocity. This new method uses the narrow gain in an SBS amplifier to modify the group index. With this technique, we found that we can produce long fractional pulse delays in an undoped single-mode fiber. This method has the advantage of producing delays at 1550 nm, and the pulses can much shorter (nanosecond) than the pulses we delayed in an EDFA. As a result, this new technique could be very useful in producing all-optical delay lines and buffers.

Finally, we investigated the stability of ring spatial solitons that carry orbital angular momentum. By analytical and numerical studies, we found that vector-ring solitons that carry no net orbital angular momentum are more resistant to azimuthal modulation instabilities than comparable beams that do carry orbital angular momentum. In addition, we found experimentally that beams (non-vector) with orbital momentum number m will break up into $2m$ spots as predicted by Firth and Skryabin [51]. More importantly, we found that these ring beams will not break up at very high power.

In conclusion, the primary goal of this work was to develop and explore new methods to create and control large group velocities. The major advantage of these techniques is that they can be implemented in room-temperature solids. As a result, these techniques offer the possibility of applications in photonics such as fully integrated, controllable optical delay lines. In addition, we investigated another important development in optical communications—ring spatial solitons. These beams are important because of their potentially improved stability, their greater power carrying abilities, and their increased information content.

Bibliography

[1] Lord Rayleigh, Proc. London Math. Society **IX**, 21 (1877).

[2] L. Brillouin, *Wave propagation and group velocity*, (Academic Press, New York, 1960).

[3] R. W. Boyd and D. J. Gauthier, *Progress in Optics* XLIII, E. Wolf, Ed. (Elsevier, Amsterdam, 2002), pp. 497-530.

[4] R. L. Smith, Am. J. Phys. **38**, 978 (1970).

[5] S. C. Bloch, Am. J. Phys. **45**, 538 (1977).

[6] R. Loudon, J. Phys. A **3**, 233 (1970).

[7] K. E. Oughstun and G. C. Sherman, *Electromagnetic Pulse Propagation in Causal Dielectrics*, (Springer-Verlag, Berlin, 1994).

[8] J. Peatross, S. A. Glasgow, and M. Ware, Phys. Rev. Lett. **84**, 2370 (2000).

[9] P. Plesko and I. Palécz, Phys. Rev. Lett. **22**, 1201 (1967).

[10] J. Aaviksoo, J. Kuhl, and K. Ploog, Phys. Rev. A **44**, R5353 (1991).

[11] G. Nimtz and A. Haibel, Ann. Phys. **11**, 163 (2002).

[12] M. D. Stenner, D. J. Gauthier, and M. A. Neifeld, Nature **425**, 695 (2003).

[13] C. G. B. Garrett and D. E. McCumber, Phys. Rev. A **1**, 305 (1970).

[14] S. Chu and S. Wong, Phys. Rev. Lett. **48**, 738 (1982).

[15] S. P. Tewari and G. S. Agarwal, Phys. Rev. Lett. **56**, 1811 (1986).

[16] S. E. Harris, J. E. Field, and A. Imamoglu, Phys. Rev. Lett. **64**, 1107 (1990); and S. E. Harris, J. E. Field, and A. Kasapi, Phys. Rev. A **46**, R29 (1992).

[17] R. S. Bennink *et al.*, Phys. Rev. A **63**, 033804 (2001).

[18] A. Kasapi *et al.*, Phys. Rev. Lett. **74**, 2447 (1995).

[19] L. V. Hau *et al.*, Nature **397**, 594 (1999).

[20] M. M. Kash *et al.*, Phys. Rev. Lett. **82**, 5229 (1999).

[21] D. Budker *et al.*, Phys. Rev. Lett. **83**, 1767 (1999).

[22] A. V. Turukhin *et al.*, Phys. Rev. Lett. **88**, 023602 (2002).

[23] C. Liu, Z. Dutton, C. H. Behroozi, and L. V. Hau, Nature **409**, 490 (2001).

[24] D. F. Phillips *et al.*, Phys. Rev. Lett. **86**, 783 (2001).

[25] M. Bajcsy, A. S. Zibrov, and M. D. Lukin, Nature **426**, 638 (2003).

[26] B. Ségard and B. Macke, Phys. Lett. A **109**, 213 (1985).

[27] M. A. I. Talukder, Y. Amagishi, and M. Tomita, Phys. Rev. Lett. **86**, 3546 (2001).

[28] A. M. Akulshin, S. Barreiro, and A. Lezema, Phys. Rev. Lett. **83**, 4277 (1999).

[29] K. Kim *et al.*, Phys. Rev. A **68**, 013810 (2003).

[30] A. M. Steinberg and R. Y. Chiao, Phys. Rev. A **49**, 2071 (1994).

[31] L. J. Wang, A. Kuzmich, and A. Dogariu, Nature **406**, 277 (2000).

[32] L. A. MacColl, Phys. Rev. **40**, 621 (1932).

[33] E. P. Wigner, Phys. Rev. **98**, 145 (1955).

[34] T. E. Hartman, J. Appl. Phys. **33**, 3427 (1962).

[35] R. Y. Chiao and A. M. Steinberg, *Progress in Optics* XXXVII, E. Wolf, Ed. (Elsevier Science, Amsterdam, 1997), pp. 345-405.

[36] A. M. Steinberg, P. G. Kwiat, and R. Y. Chiao, Phys. Rev. Lett. **71**, 708 (1993).

[37] Ch. Spielmann, R. Szipöcs, A. Stingl, and F. Krausz, Phys. Rev. Lett. **73**, 2308 (1994).

[38] H. G. Winful, Phys. Rev. Lett. **90**, 023901 (2003).

[39] H. G. Winful, Nature **424**, 638 (2003).

[40] R. Y. Chiao, E. Garmire, and C. H. Townes, Phys. Rev. Lett. **13**, 479 (1964).

[41] G. I. Stegeman and M. Segev, Science, **286**, 1518 1999.

[42] R. McLeod, K. Wagner, and S. Blair, Phys. Rev. A **52**, 3254 (1995).

[43] H. A. Haus, Appl. Phys. Lett. **8**, 128 (1966).

[44] V. I. Kruglov, Yu. A. Logvin, and V. M. Volkov, J. Mod. Opt., **39**, 2277 (1992).

[45] G. A. Swartzlander, Jr., and C. T. Law, Phys. Rev. Lett. **69**, 2503 (1992).

[46] L. Allen, M. W. Beijersbergen, R. J. C. Spreeuw, and J. P. Woerdman, Phys. Rev. A, **45**, 8185 (1992).

[47] A. Mair *et al.*, Nature **412**, 313 (2001).

[48] A. Vaziri, G. Weihs, and A. Zeilinger, J. Opt. B: Quantum Semiclass. Opt. **4**, S47 (2002).

[49] J. Leach *et al.*, Phys. Rev. Lett. **88**, 257901 (2002).

[50] See, e.g., L. Bergé, Phys. Rep. **303**, 259 (1998).

[51] W. J. Firth and D. V. Skryabin, Phys. Rev. Lett. **79**, 2450 (1997).

[52] D. V. Skryabin and W. J. Firth, Phys. Rev. E, **58**, 3916 (1998).

[53] Y. Chen, Opt. Lett. **16**, 4 (1991); M. Karlsson, Phys. Rev. A **46**, 2726 (1992); D. N. Christodoulides, T. H. Coskun, and R. I. Joseph, Opt. Lett. **22**, 1080 (1997).

[54] A. Barthelemy, S. Maneuf, and C. Froehly, Opt. Commun. **201**, 55 (1985); J. S. Aitchison *et al.*, J. Opt. Soc. Am. B **8**, 1290 (1991).

[55] N. N. Rozanov, N. V. Vysotina, and A. G. Vladimirov, JETP **91**, 1130 (2000).

[56] Z. H. Musslimani, M. Segev, D. N. Christodoulides, and M. Soljacic, Phys. Rev. Lett **84**, 1164 (2000).

[57] J. J. García-Ripoll, V. M. Pérez-García, E. A. Ostrovskaya, and Y. S. Kivshar, Phys. Rev. Lett. **85**, 82 (2000).

[58] Z. H. Musslimani *et al.*, Phys. Rev. E **63**, 066608 (2001).

[59] D. Mihalache *et al.*, J. Opt. A: Pure Appl. Opt. **4**, 615 (2002).

[60] M. S. Bigelow, Q-Han Park, and R. W. Boyd, Phys. Rev. E **66**, 046631 (2002).

[61] S. V. Manakov, Sov. Phys. JETP **38**, 248 (1974).

[62] J. U. Kang, G. I. Stegeman, J. S. Aitchison, and N. Akhmediev, Phys. Rev. Lett. **76**, 3699 (1996).

[63] X. Liu, L. J. Qian, and F. W. Wise, Phys. Rev. Lett., **82**, 4631 (1999).

[64] M. Mitchell, Z. Chen, M.-F. Shih, and M. Segev, Phys. Rev. Lett. **77**, 490 (1996).

[65] D. E. Pelinovsky and Y. S. Kivshar, Phys. Rev. E **62**, 8668 (2000).

[66] E. A. Ostrovskaya, Y. S. Kivshar, D. V. Skryabin, and W. J. Firth, Phys. Rev. Lett. **83**, 296 (1999).

[67] M. Quiroga-Teixeiro and H. Michinel, J. Opt. Soc. Am. B **14**, 2004 (1997).

[68] I. Towers *et al.*, Phys. Lett. A **288**, 292 (2001).

[69] B. A. Malomed, L. C. Crasovan, and D. Mihalache, Physica D **161**, 187 (2002).

[70] D. Mihalache *et al.*, Phys. Rev. Lett. **88**, 073902 (2002).

[71] R. L. Pego and H. A. Warchall, J. Nonlinear Sci. **12**, 347 (2002).

[72] A. V. Buryak, Y. S. Kivshar, and S. Trillo, Opt. Lett. **20**, 1961 (1995).

[73] I. Towers, A. V. Buryak, R. A. Sammut, and B. A. Malomed, Phys. Rev. E **63**, 055601(R) (2001).

[74] D. Mihalache *et al.*, Phys. Rev. E **66**, 016613 (2002).

[75] D. Mihalache *et al.*, Phys. Rev. E **67**, 056608 (2003).

[76] W. Krolikowski *et al.*, Phys. Rev. Lett. **85**, 1424 (2000).

[77] D. V. Petrov *et al.*, Opt. Lett. **23**, 1444 (1998).

[78] V. Tikhonenko, J. Christou, and B. Luther-Davies, J. Opt. Soc. Am. B **12**, 2046 (1995).

[79] V. Tikhonenko, J. Christou, and B. Luther-Davies, Phys. Rev. Lett. **76**, 2698 (1996).

[80] S. Minardi *et al.*, Opt. Lett. **26**, 1004 (2001).

[81] S. E. Schwartz and T. Y. Tan, Appl. Phys. Lett. **10**, 4 (1967).

[82] M. Sargent III, Phys. Rep. **43**, 223 (1978).

[83] R. W. Boyd, M. G. Raymer, P. Narum, and D. J. Harter, Phys. Rev. A **24**, 411 (1981).

[84] A. D. Wilson-Gordon, Phys. Rev. A **48**, 4639 (1993).

[85] L. W. Hillman, R. W. Boyd, J. Krasinski, and C. R. Stroud, Jr., Opt. Comm. **45**, 416 (1983).

[86] R. W. Boyd *Nonlinear Optics*, (Academic Press, San Diego, 1992).

[87] N. G. Basov *et al.*, Sov. Phys. JETP **23**, 16 (1966).

[88] M. S. Bigelow, N. N. Lepeshkin, and R. W. Boyd, Phys. Rev. Lett. **90** 113903 (2003).

[89] P. F. Liao and D. M. Bloom, Opt. Lett. **3**, 4 (1978).

[90] D. C. Cronemeyer, JOSA **56**, 1703 (1966).

[91] M. S. Malcuit, R. W. Boyd, L. W. Hillman, J. Kasinski, and C. R. Stroud Jr., JOSA B **1**, 73 (1984).

[92] M. L. Shand, J. C. Walling, and R. C. Morris, J. Appl. Phys. **52**, 953 (1981).

[93] E. F. Farrell, J. H. Fang, and R. E. Newnham, Am. Mineral. **48**, 804 (1963).

[94] R. C. Powell, L. Xi, X. Gang, G. J. Quarles, and J. C. Walling Phys. Rev. B **32**, 2788 (1985).

[95] M. S. Bigelow, N. N. Lepeshkin, and R. W. Boyd, Science **301**, 200 (2003).

[96] K. L. Schepler, J. Appl. Phys., **56**, 1314 (1984).

[97] G. S. Agarwal and T. N. Dey, Phys. Rev. Lett. **92**, 203901 (2004).

[98] B. Macke and B. Ségard, Eur. Phys. J. D **23**, 125 (2003).

[99] A. Kuzmich *et al.*, Phys. Rev. Lett. **86**, 3925 (2001).

[100] S. Jarabo, Appl. Opt. **35**, 4759 (1996).

[101] S. Jarabo, J. Opt. Soc. Am. B **14**, 1846 (1997).

[102] G. P. Agrawal, *Nonlinear Fiber Optics*, Second Edition, (Academic Press, San Diego, 1995).

[103] S. Novak and A. Moesle, J. Lightwave Technol. **20**, 975 (2002).

[104] J. Freeman and J. Conradi, IEEE Phot. Tech. Lett., **5**, 224 (1993).

[105] In general, angular momenta for two components can be any two integers m_1, m_2. This requires distinct propagation constants κ_1, κ_2 and radial functions $R_1(r), R_2(r)$. The simple case of common radial function $R_1(r) = R_2(r)$ is possible only when $m_1 = m$ and $m_2 = \pm m$.

[106] J. M. Soto-Crespo, D. R. Heatley, E. M. Wright, and N. N. Akhmediev, Phys. Rev. A, **44**, 636 (1991).

[107] N. R. Heckenberg *et al.*, Opt. Quant. Electron. **24**, S951 (1992).

[108] H. He, N. R. Heckenberg, and H. Rubinsztein-Dunlop, J. Mod. Optics **42**, 217 (1995).

[109] N. Kim, Opt. Commun. **105**, 1 (1994).

[110] M. L. Dowell *et al.*, Phys. Rev. A **52**, 3244 (1995).

[111] D. H. Close, Phys. Rev. **153**, 360 (1967).

[112] G. A. Swartzlander, Jr., H. Yin, and A. E. Kaplan, J. Opt. Soc. Am. B **6**, 1317 (1989).

[113] We added $\sim 1\%$ random amplitude noise to the input beam in our simulations to match the apparent noise visible in our experimental input beams. We did not consider quantum fluctuations to be significant in our experiments.

[114] T. Brabec and F. Krausz, Phys. Rev. Lett. **78**, 3282 (1997).

Appendix A

Kramers-Kronig Relations

Hilbert transforms relate the real and imaginary components of the transfer function of a causal system. The Kramers-Kronig relations are a specific type of Hilbert transform that relate the real and imaginary parts of the linear susceptibility.

A general transfer function $H(\omega)$ is the Fourier transform of the impulse response function $h(t)$ defined as

$$H(\omega) = \frac{1}{2\pi} \int_{-\infty}^{\infty} h(t) e^{i\omega t} dt. \tag{A.1}$$

For a system to be causal, the impulse response function $h(t)$ must be equal to zero for all times $t < 0$. We can then break $h(t)$ into even and odd functions so that

$$h(t) = h_{\mathrm{e}}(t) + h_{\mathrm{o}}(t), \tag{A.2}$$

where $h_e(t)$ and $h_o(t)$ are related by

$$h_e(t) = \text{sgn(t)}h_o(t), \tag{A.3a}$$

$$h_o(t) = \text{sgn(t)}h_e(t). \tag{A.3b}$$

The Signum function is defined as

$$\text{sgn(t)} = \begin{cases} -1, & t < 0 \\ 1, & t > 0. \end{cases} \tag{A.4}$$

Since the Fourier transform of an even function is purely real and the Fourier transform of an odd function is purely imaginary, we can relate

$$\mathcal{F}\{h_e(t)\} = H_r(\omega), \tag{A.5a}$$

$$\mathcal{F}\{h_o(t)\} = iH_i(\omega), \tag{A.5b}$$

where $H(\omega) = H_r(\omega) + iH_i(\omega)$. Taking the Fourier transform of Eqs. (A.3), we find that

$$H_r(\omega) = -\frac{1}{\pi\omega} \otimes H_i(\omega) = -\frac{1}{\pi}P\int_{-\infty}^{\infty} \frac{H_i(s)}{\omega - s}ds, \tag{A.6a}$$

$$H_i(\omega) = \frac{1}{\pi\omega} \otimes H_r(\omega) = \frac{1}{\pi}P\int_{-\infty}^{\infty} \frac{H_r(s)}{\omega - s}ds, \tag{A.6b}$$

where the P in front of the integral means to take the Cauchy principal value. If we

assume that $h(t)$ is real, we find that $H(-\omega) = H^*(\omega)$. Correspondingly, $H_{\mathrm{r}}(\omega)$ and

$H_{\mathrm{i}}(\omega)$ must be even and odd functions, respectively. So from Eq. (A.6a) we can write

$$
\begin{aligned}
H_{\mathrm{r}}(\omega) &= -\frac{1}{\pi}\left[P\int_{-\infty}^{0}\frac{H_{\mathrm{i}}(p)}{\omega - p}dp + P\int_{0}^{\infty}\frac{H_{\mathrm{i}}(s)}{\omega - s}ds \right] \\
&= -\frac{1}{\pi}P\int_{0}^{\infty}H_{\mathrm{i}}(s)\left[\frac{-1}{\omega + s} + \frac{1}{\omega - s}\right]ds \\
&= -\frac{2}{\pi}P\int_{0}^{\infty}\frac{sH_{\mathrm{i}}(s)}{\omega^2 - s^2}ds.
\end{aligned} \tag{A.7}
$$

Likewise, we can express the imaginary part of the transfer function only in terms of

positive frequencies as

$$
H_{\mathrm{i}}(\omega) = \frac{2\omega}{\pi}P\int_{0}^{\infty}\frac{H_{\mathrm{r}}(s)}{\omega^2 - s^2}ds. \tag{A.8}
$$

The susceptibility $\chi(\omega)$ is a transfer function that relates the polarization to the

electric field as

$$
P(\omega) = \chi(\omega)E(\omega). \tag{A.9}
$$

In addition, it is linear and causal so it satisfies the other assumptions we made about

the more general transfer function. As a result, we can use Eqs. (A.7) and (A.8) to

relate the real and imaginary components of the susceptibility as

$$
\begin{aligned}
\chi_{\mathrm{r}}(\omega) &= -\frac{2}{\pi}P\int_{0}^{\infty}\frac{s\chi_{\mathrm{i}}(s)}{\omega^2 - s^2}ds, \tag{A.10a}\\
\chi_{\mathrm{i}}(\omega) &= \frac{2\omega}{\pi}P\int_{0}^{\infty}\frac{\chi_{\mathrm{r}}(s)}{\omega^2 - s^2}ds. \tag{A.10b}
\end{aligned}
$$

This is the most common expression for the Kramers-Kronig relations. These relations

can also be derived by using Cauchy's integral theorem [86].

It is useful to modify Eqs. (A.10) to relate the real part of the refractive index to the absorption. Since $n = \sqrt{1 + 4\pi\chi} \simeq 1 + 2\pi\chi$, we find that

$$n_{\mathrm{r}}(\omega) = 1 + 2\pi\chi_{\mathrm{r}}(\omega)$$

$$n_{\mathrm{i}}(\omega) = 2\pi\chi_{\mathrm{i}}(\omega).$$

Finally, we can relate the intensity absorption coefficient to the imaginary part of the refractive index as $\alpha(\omega) = 2\omega n_{\mathrm{i}}(\omega)/c$. This gives us the relations shown in Chap. 1

$$n_{\mathrm{r}}(\omega) = 1 + \frac{c}{\pi}P\int_0^\infty \frac{\alpha(s)}{s^2 - \omega^2}ds, \tag{A.11a}$$

$$\alpha(\omega) = -\frac{4\omega^2}{\pi c}P\int_0^\infty \frac{n_{\mathrm{r}}(s) - 1}{s^2 - \omega^2}ds. \tag{A.11b}$$

Appendix B

Energy-Transport Velocity

As stated in Chap. 1, the energy-transport velocity in an isotropic dielectric is equal to

$$v_e = \frac{c}{n_{\rm r} + 2\omega n_{\rm i}/\Gamma},$$

(B.1)

where Γ is the oscillator damping coefficient of a Lorentz material and $n_{\rm r}$ and $n_{\rm i}$ are the real and imaginary parts of the refractive index. Here we wish to verify that Eq. (B.1) is correct. This derivation follows that of Loudon [6].

The equation of motion for a simple harmonic oscillator with mass m and charge e under the influence of an electric field $\mathbf{E}$ is

$$m(\ddot{\mathbf{r}} + \Gamma\dot{\mathbf{r}} + \omega_0^2\mathbf{r}) = e\mathbf{E},$$

(B.2)

where Γ is the damping coefficient and ω_0 is the resonant frequency. We assume that

the electric field and the position vector point in the same direction so we can drop

the vector notation. Also, we assume that both E and r oscillate at $e^{-i\omega t}$. We can

now rewrite Eq. (B.2) as

$$r = \frac{eE}{m} \frac{1}{-\omega^2 - i\Gamma\omega + \omega_0^2},$$

(B.3)

or

$$|r|^2 = \frac{e^2}{m^2} \frac{1}{(\omega^2 + \omega_0^2)^2 + \omega^2\Gamma^2} |E|^2.$$

(B.4)

The polarization of the material can be written as

$$P = \frac{e}{V} r + \frac{\epsilon_\infty - 1}{4\pi} E,$$

(B.5)

where V is the volume of a single oscillator and ϵ_∞ is the background dielectric

constant caused by higher-frequency resonances. As a result, the dielectric constant

ϵ can be expressed as

$$\begin{aligned}
\epsilon &= 1 + 4\pi \frac{P}{E} \\
&= 1 + \frac{4\pi}{E} \left(\frac{e^2 E}{mV} \frac{1}{-\omega^2 - i\Gamma\omega + \omega_0^2} + \frac{\epsilon_\infty - 1}{4\pi} E \right) \\
&= \epsilon_\infty \left(1 + \frac{\Lambda^2}{-\omega^2 - i\Gamma\omega + \omega_0^2} \right),
\end{aligned}$$

(B.6)

where

$$\Lambda^2 = \frac{4\pi e^2}{mV\epsilon_\infty}$$

(B.7)

is the plasma frequency. The refractive index $n = n_{\rm r} + i n_{\rm i}$ is related to the dielectric

constant as $n = \sqrt{\epsilon}$, so from Eq. (B.6) we can write

$$n_{\rm r}^2 - n_{\rm i}^2 = \epsilon_\infty \left[1 + \frac{\Lambda^2 (\omega^2 + \omega_0^2)^2}{(\omega^2 + \omega_0^2)^2 + \omega^2 \Gamma^2} \right], \tag{B.8}$$

$$2 n_{\rm r} n_{\rm i} = \frac{\epsilon_\infty \Lambda^2 \omega \Gamma}{(\omega^2 + \omega_0^2)^2 + \omega^2 \Gamma^2}. \tag{B.9}$$

Now we can use these results to find the energy-transport velocity in a dielectric.

As mentioned in Chap. 1, the energy-transport velocity is defined as

$$v_e = \mathbf{S}/W, \tag{B.10}$$

where

$$\mathbf{S} = \frac{c}{4\pi} \mathbf{E} \times \mathbf{H} \tag{B.11}$$

is the Poynting vector and W is the energy density. The magnitude of the electric

field E is related to H as $E = nH$, so if we take the time average of Eq. (B.11) over

one cycle, we find that

$$\langle S \rangle = \frac{c}{8\pi} \mathrm{Re}(\mathrm{EH}^*)$$

$$= \frac{c n_{\rm r}}{8\pi} |E|^2. \tag{B.12}$$

The energy density W can be derived from Maxwell's equations [6] or we can write

it out from our knowledge of the system. We observe that

$$W = \frac{m}{2V}(\dot{r}^2 + \omega_0^2 r^2) + \frac{\epsilon_\infty E^2 + H^2}{8\pi}, \tag{B.13}$$

where the first term is the kinetic and potential energy densities of the oscillators, and the second term is the energy density of the fields. We take a time average of Eq. (B.13) to get

$$\langle W \rangle = (\omega^2 + \omega_0^2)|r|^2 + \frac{|E|^2}{16\pi}(\epsilon_\infty + n_r^2 + n_i^2). \tag{B.14}$$

If we apply Eqs. (B.4), (B.8) and (B.9) we find

$$
\begin{aligned}
\langle W \rangle &= \frac{e^2}{4Vm}\frac{(\omega^2 + \omega_0^2)}{(\omega^2 + \omega_0^2)^2 + \omega^2\Gamma^2}|E|^2 + \frac{|E|^2}{16\pi}(\epsilon_\infty + n_r^2 + n_i^2) \\
&= \frac{|E|^2}{16\pi}\left(\frac{\epsilon_\infty\Lambda^2(\omega^2 + \omega_0^2)}{(\omega^2 + \omega_0^2)^2 + \omega^2\Gamma^2} + \epsilon_\infty + n_r^2 + n_i^2\right) \\
&= \frac{|E|^2}{16\pi}\left(\frac{2n_r n_i}{\omega\Gamma}(\omega^2 + \omega_0^2) + \epsilon_\infty + n_r^2 + n_i^2\right) \\
&= \frac{|E|^2}{16\pi}\left(\frac{2\omega n_r n_i}{\Gamma} + \frac{2\omega_0^2 n_r n_i}{\omega\Gamma} + 2n_r^2 - \frac{\epsilon_\infty\Lambda^2(\omega_0^2 - \omega^2)}{(\omega^2 + \omega_0^2)^2 + \omega^2\Gamma^2}\right) \\
&= \frac{n_r}{8\pi}\left(\frac{2\omega n_i}{\Gamma} + n_r\right)|E|^2. \tag{B.15}
\end{aligned}
$$

Now we can combine Eqs. (B.12) and (B.15) to find a simple expression for the

energy-transport velocity

$$
\begin{aligned}
v_e &= \frac{\langle S \rangle}{\langle W \rangle} \\
&= \frac{c}{n_\mathrm{r} + 2\omega n_\mathrm{i}/\Gamma},
\end{aligned}
\tag{B.16}
$$

which the same as Eq. (B.1).

Appendix C

The Nonlinear Schödinger

Equation

The nonlinear Schödinger equation (NLSE) is the standard equation describing the evolution of the electric field inside a nonlinear material. Starting from the 3-D wave equation, I derive the NLSE keeping many of the higher-order terms. This derivation is based on Brabec and Krausz [114].

C.1   Single Field Equation

We start with the 3-D wave equation given by

$$(\partial_z^2 + \nabla_\perp^2)E(\mathbf{r},t) - \frac{1}{c^2}\partial_t^2 \int_{-\infty}^{t} dt'\varepsilon(t-t')E(\mathbf{r},t') = \frac{4\pi}{c^2}\partial_t^2 P_{nl}(\mathbf{r},t) \qquad \text{(C.1)}$$

where

$$\varepsilon(t) = \frac{1}{2\pi} \int_{-\infty}^{\infty} \varepsilon(\omega) e^{-i\omega t} d\omega, \tag{C.2}$$

and $n(\omega) = \sqrt{\varepsilon(\omega)}$. We define the following ansatz for the solution to this equation (assuming a linear polarization and lossless medium) $E(\mathbf{r}, t) = A(\mathbf{r}_\perp, z, t) e^{i(\beta_0 z - \omega_0 t)} +$ c.c. and $P_{nl}(\mathbf{r}, t) = B(\mathbf{r}_\perp, z, t) e^{i(\beta_0 z - \omega_0 t)} +$ c.c. Now we consider the second term of Eq. (C.1). If we take the Fourier transform of this term we get

$$\begin{aligned}
\frac{\omega^2}{c^2} \varepsilon(\omega) A(\mathbf{r}_\perp, z, \omega - \omega_0) &= \beta(\omega)^2 A \\
&= \left[\beta_0 + \sum_{m=1}^{\infty} \frac{\beta_m}{m!} (\omega - \omega_0)^m \right]^2 A \\
&= \left[\beta_0 + \beta_1 (\omega - \omega_0) + \sum_{m=2}^{\infty} \frac{\beta_m}{m!} (\omega - \omega_0)^m \right]^2 A.
\end{aligned}$$

Now taking the inverse Fourier transform of this expression we get

$$\left[\beta_0 + i\beta_1 \partial_t + \widehat{D} \right]^2 A(\mathbf{r}_\perp, z, t) e^{-i\omega_0 t}, \tag{C.3}$$

where

$$\widehat{D} = \sum_{m=2}^{\infty} \frac{\beta_m}{m!} (i\partial_t)^m.$$

We substitute (C.3) and our ansatz into Eq. (C.1) to get

$$
\left(-\beta_0^2 + 2i\beta_0\partial_z + \partial_z^2 + \nabla_\perp^2 \right) A \;\; + \;\; \left[\beta_0 + i\beta_1\partial_t + \widehat{D} \right]^2 A
$$

$$
= \;\; \frac{4\pi}{c^2} \left(-\omega_0^2 - 2i\omega_0\partial_t + \partial_t^2 \right) B
$$

$$
= \;\; -\frac{4\pi\omega_0^2}{c^2} \left(1 + \frac{i}{\omega_0}\partial_t \right)^2 B. \tag{C.4}
$$

By collecting some terms this becomes

$$
\left[2i\beta_0\partial_z + \partial_z^2 + \nabla_\perp^2 + 2i\beta_0\beta_1\partial_t + 2\beta_0\widehat{D} - (\beta_1\partial_t)^2 + 2i\beta_1\partial_t\widehat{D} + \widehat{D}^2 \right] A
$$

$$
+ \frac{4\pi\omega_0^2}{c^2} \left(1 + \frac{i}{\omega_0}\partial_t \right)^2 B = 0. \tag{C.5}
$$

If we divide by $2i\beta_0$ and move some terms around we get

$$
\left(\partial_z + \beta_1\partial_t - i\widehat{D} \right) A + \frac{1}{2i\beta_0}\nabla_\perp^2 A + \frac{2\pi\omega_0^2}{i\beta_0 c^2} \left(1 + \frac{i}{\omega_0}\partial_t \right)^2 B
$$

$$
= \frac{\beta_1\partial_t\widehat{D}}{\beta_0}A - \frac{1}{2i\beta_0} \left(\partial_z^2 - (\beta_1\partial_t)^2 + \widehat{D}^2 \right) A. \tag{C.6}
$$

Now we go to a moving reference frame $\tau = t - \beta_1 z$. So $\partial_z \rightarrow \partial_z - \beta_1 \partial_t$, $\partial_z^2 \rightarrow \partial_z^2 - 2\beta_1 \partial_t \partial_z + (\beta_1 \partial_t)^2$, and $\partial_t \rightarrow \partial_\tau$. As a result, Eq. (C.6) reduces to

$$
\begin{aligned}
\left(\partial_z - i\widehat{D}\right) A + \frac{1}{2i\beta_0}\nabla_\perp^2 A \;\; + \;\; & \frac{2\pi\omega_0^2}{i\beta_0 c^2}\left(1 + \frac{i}{\omega_0}\partial_\tau\right)^2 B \\
= \;\; & \frac{\beta_1 \partial_t \widehat{D}}{\beta_0}A - \frac{1}{2i\beta_0}\left(\partial_z^2 - 2\beta_1 \partial_t \partial_z + \widehat{D}^2\right) A \\
= \;\; & -\frac{i\beta_1 \partial_t}{\beta_0}\left(\partial_z - i\widehat{D}\right) A - \frac{1}{2i\beta_0}\left(\partial_z^2 + \widehat{D}^2\right) A. \quad \text{(C.7)}
\end{aligned}
$$

Now we add $\frac{i}{\omega_0}\partial_\tau\left(\partial_z - i\widehat{D}\right) A$ to both sides of the equation to get

$$
\begin{aligned}
\left(1 + \frac{i}{\omega_0}\partial_\tau\right)&\left[\left(\partial_z - i\widehat{D}\right) A - i\frac{2\pi\beta_0}{n_0^2}\left(1 + \frac{i}{\omega_0}\partial_\tau\right) B\right] - \frac{i}{2\beta_0}\nabla_\perp^2 A \\
= \;\; & \left(\frac{\beta_0 - \omega_0 \beta_1}{\beta_0}\right)\frac{i}{\omega_0}\partial_\tau\left(\partial_z - i\widehat{D}\right) A - \frac{1}{2i\beta_0}\left(\partial_z^2 + \widehat{D}^2\right) A \\
= \;\; & \left(1 - \frac{c/n_0}{v_g}\right)\frac{i}{\omega_0}\partial_\tau\left(\partial_z - i\widehat{D}\right) A - \frac{1}{2i\beta_0}\left(\partial_z^2 + \widehat{D}^2\right) A. \quad \text{(C.8)}
\end{aligned}
$$

We can see that if the group velocity is close to the phase velocity, we can safely neglect the first term on the right hand side of this equation. Also, since $\widehat{D}^2$ would not have anything less than fourth-order time derivatives, we can neglect this term. Finally, we make the assumption that $|\partial_z A| \ll \beta_0 |A|$ (SVEA) which allows us to neglect the second-order derivative in z. So Eq. (C.8) becomes

$$
\partial_z A = \frac{i}{2\beta_0}\left(1 + \frac{i}{\omega_0}\partial_\tau\right)^{-1}\nabla_\perp^2 A + i\widehat{D} + i\frac{2\pi\omega_0}{n_0 c}\left(1 + \frac{i}{\omega_0}\partial_\tau\right) B. \quad \text{(C.9)}
$$

If we keep up to third order derivatives in time and assume a Kerr nonlinearity $(B = n_2 n_0^2 c/4\pi^2 |A|^2 A)$, we get the more familiar expression

$$\boxed{\partial_z A = \frac{i}{2\beta_0}\left(1 + \frac{i}{\omega_0}\partial_\tau\right)^{-1}\nabla_\perp^2 A - i\frac{\beta_2}{2}\partial_\tau^2 A - i\frac{\beta_3}{6}\partial_\tau^3 A + i\frac{n_2 n_0 \omega_0}{2\pi}\left(1 + \frac{i}{\omega_0}\partial_\tau\right)|A|^2 A.}$$

$$(C.10)$$

C.2 Coupled Field Equations

Now we derive a coupled equation with two fields. Like we did for the single-field case, we again start with the 3-D wave equation given as

$$(\partial_z^2 + \nabla_\perp^2)E(\mathbf{r}, t) - \frac{1}{c^2}\partial_t^2\int_{-\infty}^{t} dt'\varepsilon(t - t')E(\mathbf{r}, t') = \frac{4\pi}{c^2}\partial_t^2 P_{nl}(\mathbf{r}, t)$$

where

$$\varepsilon(t) = \frac{1}{2\pi}\int_{-\infty}^{\infty}\varepsilon(\omega)e^{-i\omega t}d\omega,$$

and $n(\omega) = \sqrt{\varepsilon(\omega)}$. However, now there are two fields present with the form

$$
\begin{aligned}
E(\mathbf{r}, t) &= A_1(\mathbf{r}_\perp, z, t)e^{i(\beta_{01}z - \omega_{01}t)} + A_2(\mathbf{r}_\perp, z, t)e^{i(\beta_{02}z - \omega_{02}t)} + \text{c.c.}, \\
P_{nl}(\mathbf{r}, t) &= B_1(\mathbf{r}_\perp, z, t, A_1, A_2)e^{i(\beta_{01}z - \omega_{01}t)} + B_2(\mathbf{r}_\perp, z, t, A_1, A_2)e^{i(\beta_{02}z - \omega_{02}t)} + \text{c.c.}
\end{aligned}
$$

Again, we take the Fourier transform of the second term to get

$$\frac{\omega^2}{c^2}\varepsilon(\omega)\left(A_1(\mathbf{r}_\perp, z, \omega - \omega_{01}) + A_2(\mathbf{r}_\perp, z, \omega - \omega_{02})\right)$$

$$= \beta(\omega)^2 \left(A_1(\mathbf{r}_\perp, z, \omega - \omega_{01}) + A_2(\mathbf{r}_\perp, z, \omega - \omega_{02})\right).$$

Now we will expand $\beta(\omega)$ in a Taylor series about ω_{01} and ω_{02} for each of the two

terms to get

$$\Rightarrow \left[\beta_{01} + \beta_{11}(\omega - \omega_{01}) + \sum_{m=2}^{\infty} \frac{\beta_{m1}}{m!}(\omega - \omega_{01})^m\right]^2 A_1(\mathbf{r}_\perp, z, \omega - \omega_{01})$$

$$+ \left[\beta_{02} + \beta_{12}(\omega - \omega_{02}) + \sum_{m=2}^{\infty} \frac{\beta_{m2}}{m!}(\omega - \omega_{02})^m\right]^2 A_2(\mathbf{r}_\perp, z, \omega - \omega_{02}).$$

Taking the inverse Fourier transform of this expression yields

$$\left[\beta_{01} + i\beta_{11}\partial_t + \widehat{D}_1\right]^2 A_1(\mathbf{r}_\perp, z, t)e^{-i\omega_{01}t} + \left[\beta_{02} + i\beta_{12}\partial_t + \widehat{D}_2\right]^2 A_2(\mathbf{r}_\perp, z, t)e^{-i\omega_{02}t},$$

where

$$\widehat{D}_1 = \sum_{m=2}^{\infty} \frac{\beta_{m1}}{m!}(i\partial_t)^m, \quad \widehat{D}_2 = \sum_{m=2}^{\infty} \frac{\beta_{m2}}{m!}(i\partial_t)^m.$$

We assume each frequency component of the field satisfies Eq. (C.1), so we decompose the equation into

$$
\left(-\beta_{01}^2 + 2i\beta_{01}\partial_z + \partial_z^2 + \nabla_\perp^2\right) A_1 \; + \; \left[\beta_{01} + i\beta_{11}\partial_t + \widehat{D}_1\right]^2 A_1
$$
$$
= \; -\frac{4\pi\omega_{01}^2}{c^2}\left(1 + \frac{i}{\omega_{01}}\partial_t\right)^2 B_1, \qquad \text{(C.11)}
$$

and

$$
\left(-\beta_{02}^2 + 2i\beta_{02}\partial_z + \partial_z^2 + \nabla_\perp^2\right) A_2 \; + \; \left[\beta_{02} + i\beta_{12}\partial_t + \widehat{D}_2\right]^2 A_2
$$
$$
= \; -\frac{4\pi\omega_{02}^2}{c^2}\left(1 + \frac{i}{\omega_{02}}\partial_t\right)^2 B_2. \qquad \text{(C.12)}
$$

With some basic manipulation, Eq. (C.12) becomes

$$
\left(\partial_z + \beta_{12}\partial_t - i\widehat{D}\right) A_2 + \frac{1}{2i\beta_{02}}\nabla_\perp^2 A_2 + \frac{2\pi\omega_{02}^2}{i\beta_{02}c^2}\left(1 + \frac{i}{\omega_{02}}\partial_t\right)^2 B_2
$$
$$
= \frac{\beta_{12}\partial_t\widehat{D}_2}{\beta_{02}} A_2 - \frac{1}{2i\beta_{02}}\left(\partial_z^2 - (\beta_{12}\partial_t)^2 + \widehat{D}_2^2\right) A_2. \qquad \text{(C.13)}
$$

Following the same procedure as we did for the single-field case, we go to the moving

reference frame ($\tau = t - \beta_{11}z$) of A_1 to get

$$\left(\partial_z + (\beta_{12} - \beta_{11})\partial_\tau - i\widehat{D}\right)A_2 + \frac{1}{2i\beta_{02}}\nabla_\perp^2 A_2 + \frac{2\pi\omega_{02}^2}{i\beta_{02}c^2}\left(1 + \frac{i}{\omega_{02}}\partial_\tau\right)^2 B_2$$

$$= \frac{\beta_{12}\partial_\tau\widehat{D}_2}{\beta_{02}}A_2 - \frac{1}{2i\beta_{02}}\left(\partial_z^2 - (\beta_{12}\partial_\tau)^2 - 2\beta_{11}\partial_\tau\partial_z + (\beta_{11}\partial_\tau)^2 + \widehat{D}_2^2\right)A_2$$

$$= \frac{\partial_\tau}{\beta_{02}}\left(\beta_{12}\widehat{D}_2 - i\beta_{11}\partial_z\right)A_2 + \frac{i}{2\beta_{02}}\left(\beta_{11}^2 - \beta_{12}^2\right)\partial_\tau^2 A_2 + \frac{i}{2\beta_{02}}\left(\partial_z^2 + \widehat{D}_2^2\right)A_2$$

$$= \frac{-i\beta_{12}\partial_\tau}{\beta_{02}}\left(\frac{\beta_{11}}{\beta_{12}}\partial_z - i\widehat{D}_2\right)A_2 + \frac{i}{2\beta_{02}}\left(\beta_{11}^2 - \beta_{12}^2\right)\partial_\tau^2 A_2 + \frac{i}{2\beta_{02}}\left(\partial_z^2 + \widehat{D}_2^2\right)A_2.$$

We make the approximation $\beta_{12} \simeq \beta_{11}$ so that $(\beta_{11}^2 - \beta_{12}^2) = (\beta_{11} - \beta_{12})(\beta_{11} + \beta_{12})$

$\approx 2\beta_{12}(\beta_{11} - \beta_{12})$. Now we add $\frac{i}{\omega_{02}}\partial_\tau\left(\partial_z + (\beta_{12} - \beta_{11})\partial_\tau - i\widehat{D}_2\right)A_2$ to both sides

$$\left(1 + \frac{i}{\omega_{02}}\partial_\tau\right)\left[\left(\partial_z + (\beta_{12} - \beta_{11})\partial_\tau - i\widehat{D}_2\right)A_2 + \frac{2\pi\omega_{02}^2}{i\beta_{02}c^2}\left(1 + \frac{i}{\omega_{02}}\partial_\tau\right)B_2\right]$$

$$- \frac{i}{2\beta_{02}}\nabla_\perp^2 A_2$$

$$\simeq \left(\frac{\beta_{02} - \omega_{02}\beta_{12}}{\beta_{02}}\right)\frac{i}{\omega_{02}}\partial_\tau\left(\partial_z + (\beta_{12} - \beta_{11})\partial_\tau - i\widehat{D}_2\right)A_2 + \frac{i}{2\beta_{02}}\left(\partial_z^2 + \widehat{D}_2^2\right)A_2$$

$$= \left(1 - \frac{c/n_{02}}{v_{g,2}}\right)\frac{i}{\omega_{02}}\partial_\tau\left(\partial_z + (\beta_{12} - \beta_{11})\partial_\tau - i\widehat{D}_2\right)A_2 + \frac{i}{2\beta_{02}}\left(\partial_z^2 + \widehat{D}_2^2\right)A_2$$

Now we can make the same approximations (SVEA) that we made for the single-field

case which is equivalent to setting the entire right-hand side of this equation to zero

$$\boxed{\partial_z A_2 = \frac{i}{2\beta_{02}}\left(1 + \frac{i}{\omega_{02}}\partial_\tau\right)^{-1}\nabla_\perp^2 A_2 - (\beta_{12} - \beta_{11})\partial_\tau A_2 + i\widehat{D}_2 + i\frac{2\pi\omega_{02}}{n_{02}c}\left(1 + \frac{i}{\omega_{02}}\partial_\tau\right)B_2.}$$

$$(\text{C}.14)$$

Likewise, following an identical procedure as in the single-field case, Eq. (C.11) becomes

$$\partial_z A_1 = \frac{i}{2\beta_{01}} \left(1 + \frac{i}{\omega_{01}}\partial_\tau\right)^{-1} \nabla_\perp^2 A_1 + i\widehat{D}_1 + i\frac{2\pi\omega_{01}}{n_{01}c}\left(1 + \frac{i}{\omega_{01}}\partial_\tau\right) B_1. \qquad (C.15)$$

Now lets consider the special case of second harmonic generation in a Kerr medium. In this case $B_1 = 2\chi^{(2)} A_2 A_1^* e^{-i\Delta kz} + 3\chi^{(3)} |A_1|^2 A_1 + 6\chi^{(3)} |A_2|^2 A_1$, and $B_2 = \chi^{(2)} A_1^2 e^{i\Delta kz}$ $+3\chi^{(3)} |A_2|^2 A_2 + 6\chi^{(3)} |A_1|^2 A_2$. Putting these into Eqs. (C.14) and (C.15) and keeping up to third-order time derivatives, we get

$$\begin{aligned}
\partial_z A_1 &= \frac{i}{2\beta_{01}}\left(1 + \frac{i}{\omega_{01}}\partial_\tau\right)^{-1}\nabla_\perp^2 A_1 - i\frac{\beta_2}{2}\partial_\tau^2 A_1 - i\frac{\beta_3}{6}\partial_\tau^3 A_1 \\
&\quad + i\frac{8\pi\omega_{01}d}{n_{01}c}\left(1 + \frac{i}{\omega_{01}}\partial_\tau\right) A_2 A_1^* e^{-i\Delta kz} \\
&\quad + i\frac{n_2 n_{01}\omega_{01}}{2\pi}\left(1 + \frac{i}{\omega_{01}}\partial_\tau\right)\left(|A_1|^2 + 2|A_2|^2\right) A_1, \qquad (C.16)
\end{aligned}$$

and

$$\begin{aligned}
\partial_z A_2 &= \frac{i}{2\beta_{02}}\left(1 + \frac{i}{\omega_{02}}\partial_\tau\right)^{-1}\nabla_\perp^2 A_2 - (\beta_{12} - \beta_{11})\partial_\tau A_2 - i\frac{\beta_2}{2}\partial_\tau^2 A_1 - i\frac{\beta_3}{6}\partial_\tau^3 A_1 \\
&\quad + i\frac{4\pi\omega_{02}d}{n_{02}c}\left(1 + \frac{i}{\omega_{02}}\partial_\tau\right) A_1^2 e^{i\Delta kz} \\
&\quad + i\frac{n_2 n_{02}\omega_{02}}{2\pi}\left(1 + \frac{i}{\omega_{02}}\partial_\tau\right)\left(|A_2|^2 + 2|A_1|^2\right) A_2. \qquad (C.17)
\end{aligned}$$

The extra subscripts on β_2, β_3, and n_2 which indicate what frequency they should be evaluated at have been neglected to simplify the notation.